Electronic Thesis and Dissertation Repository

4-6-2021 11:00 AM

Formation of Supermassive Black Holes in the Early Universe

Arpan Das, *The University of Western Ontario*

Supervisor: Basu, Shantanu, *The University of Western Ontario*
Co-Supervisor: Buchel, Alex, *The University of Western Ontario*
A thesis submitted in partial fulfillment of the requirements for the Doctor of Philosophy degree in Astronomy
© Arpan Das 2021

Follow this and additional works at: https://ir.lib.uwo.ca/etd

Part of the Cosmology, Relativity, and Gravity Commons, External Galaxies Commons, and the Stars, Interstellar Medium and the Galaxy Commons

Abstract

The aim of the work presented in this thesis is to understand the formation and growth of the seeds of the supermassive black holes in early universe. Supermassive black holes (SMBH) with masses larger than $10^8 \, \mathrm{M_\odot}$ have been observed when the Universe was only 800 Myr old. The formation and accretion history of the seeds of these supermassive black holes are a matter of debate.

In the first part, considering the scenario of massive seed black hole formation which allows gas to directly collapse into a black hole (DCBH) of similar mass, we show that the mass function of SMBH can be described as a broken power-law with two characteristic features: (1) a power-law at intermediate masses whose index is the dimensionless ratio of the growth rate of the number of DCBH during their formation era, and the growth rate of DCBH masses by super-Eddington accretion during the DCBH growth era, (2) a break in the power law profile at high masses whose location is related to the duration of the period of DCBH growth.

In the second part, we explore another possible pathway for the formation of SMBH seeds via gas accretion and runaway stellar collisions in high-redshift, metal-poor nuclear star clusters. These SMSs are born with masses $10^3 - 10^5 \, \mathrm{M_\odot}$ which could grow into a few times $10^9 \, \mathrm{M_\odot}$ supermassive black holes observed at $z \sim 7$ via Eddington-accretion. We explore physically motivated accretion scenarios, e.g. Bondi–Hoyle–Lyttleton accretion and Eddington accretion, as well as simplified scenarios such as a constant accretion. While gas is present, the accretion timescale remains considerably shorter than the timescale for collisions with the most massive object. However, the timescale for collisions between any two stars in the cluster can become comparable or shorter than the accretion timescale, hence collisions still play a relevant role. In addition, initial collisions will speed up the accretion process particularly in the Eddington and Bondi scenario. We also show that additional factors e.g., the upper IMF cut-off, the compactness of the cluster and mass loss during the collision might affect the final off the SMSs born.

Finally, we study how the mass loss due to stellar will affect the formation of the SMSs in the NSCs, especially in high-metallicity environments using idealised N-body simulations. We adopt theoretical mass loss rates from the literature. Considering different accretion scenarios, we have studied the effect of the mass loss rates over a wide range of metallicities $Z_* = [.001 - 1] Z_\odot$ and Eddington factors $f_{\mathrm{Edd}} = L_*/L_{\mathrm{Edd}} = 0.5, 0.7, \& \, 0.9$.

Summary for lay audience

Cutting-edge observations of the universe in the past decades have revealed the existence of supermassive black holes of masses up to a few billion times the mass of the Sun within the first billion years after the birth of the universe a.k.a the Big Bang. How these massive objects formed and grew over such a short time still remains one of the biggest puzzles in the field of astronomy. In the past decades, many different theories have been proposed. In this thesis, we study the formation and growth of these massive objects via two different scenarios. The first one is known as the direct collapse black hole scenario where a black hole can be formed directly without forming a normal star. The second model is the formation of these black holes via collisions between stars and gas accretion in a dense nuclear star cluster. Our results suggest that both the channels we have studied are viable for the growth of these observed supermassive black holes.

Co-Authorship Statement

The three papers that constitute this Thesis were co-authored with various collaborators.

For the first paper in Chapter 1, I am the second author and Prof. Shantanu Basu is the first author. The idea and the model was proposed by Prof. Shantanu Basu. I applied the model to analyze the data. Both Shantanu Basu and I wrote the paper. I did approximately half of the work. This work was published in Astrophysical Journal Letters (url: https://iopscience.iop.org/article/10.3847/2041-8213/ab2646) on June 28th, 2019.

For the project in Chapter 2, I am the principal author. I wrote the paper with the input from my collaborators. The idea of the paper was proposed by Prof. Dominik Schleicher, who is a co-author. The numerical code I used to build the model and produce the results was based on the code by Tjarda Boekholt which was modified by me. Prof. Nathan Leigh, who is also a co-author, helped me to analyze the results. I did approximately three quarters of the work. The work was published in Monthly Notices of Royal Astronomical Society (url: https://academic.oup.com/mnras/advance-article-abstract/doi/10.1093/mnras/stab402/6133460) on Feb 11th, 2021.

For the project in Chapter 3, I am the principal author. This is an extension of the project in Chapter 2 and the idea was proposed by Prof. Dominik Schleicher, who is a co-author. Prof. Shantanu Basu, who is also a co-author of this paper, helped me to write the paper by giving valuable inputs. I did approximately three quarters of the work. The work is submitted to Monthly Notices of Royal Astronomical Society on Feb 3rd, 2021.

Dedicated to my father Pabitra Das and mother Nilima Das

"The cosmos is within us. We are made of star-stuff. We are a way for the universe to know itself.' - Carl Sagan

Contents

List of Figures

List of Tables

Chapter 1

Introduction

Over the last decade, astronomers have succeeded to understand much of the history of the Universe at unprecedented levels. Ground- and space-based observatories have done an incredible job to detect galaxies and quasars up to high redshifts ($z \sim 7$, where z stands for redshift) corresponding to times when the Universe was just 700 Myr old. At present, thousands of galaxies and quasars have been catalogued at redshift $z > 4$, and hundreds above $z > 6$, thanks to the remarkable achievements of the Sloan Digital Sky Survey (SDSS) and the Hubble Space Telescope (HST). Gamma-ray bursts have also been detected in recent years. Together, these observations have yielded important insights for understanding the evolution of the universe, including the star formation history, properties of the intergalactic medium (IGM), and galaxy formation.

At the same time, the measurements of the cosmic microwave background (CMB), by the Wilkinson Microwave Anisotropy Probe (WMAP) and Planck mission have provided the effective boundary conditions that govern the large-scale evolution of the Universe and ultimately the nature of the subsequent gravitational collapse of structures such as stars, galaxies, and quasars. Coupled with powerful cosmological probes at relatively low redshifts ($z < 1$), including statistical analysis of the distribution of galaxies, measurements of the acceleration history of the Universe using Type-Ia supernovae, and constraints on the abundance of dark matter from observations of galaxy clusters, cosmologists have built a self consistent model of the evolution of the universe.

Despite this amazing progress, a large gap remains in the history of the Universe for which there are currently no direct probes. This gap is also known as the cosmological "dark ages"(between 380,000 yr and 200 Myr after the Big Bang). Information from this period is not explicitly contained in the CMB because baryonic matter and radiation have already decoupled and CMB photons stream freely through the IGM. The upcoming telescopes are hoping to detect galaxies and quasars only from the end of the dark ages.

Probing this epoch has become one of the most important tasks in modern astrophysics and cosmology. It is extremely challenging to study the sources of the "first light". Theoretically, the first generation of stars could form as early as 100 to 200 Myr after the Big Bang. These stars are thought to be extremely massive, $\sim 100\,M_\odot$, and therefore very short-lived. In principle, their

deaths should produce a number of gamma-ray bursts that may eventually be detected. Massive galaxies and supermassive black holes may exist as well during early times. The upcoming James Webb Space Telescope (JWST) and next-generation 30 m ground based telescopes should be able to detect these objects out to very high redshifts ($z < 15$).
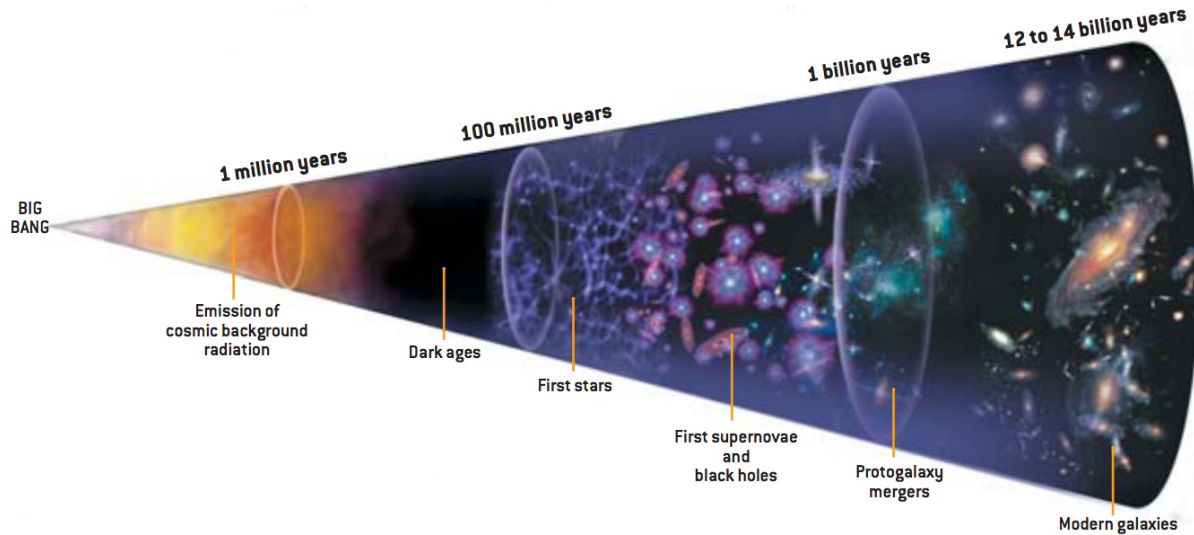
Figure 1.1: Cosmic timeline (Fig. courtesy: SCIENTIFIC AMERICAN, INC.)

In this Thesis, the new work developed that is related to the growth and formation history of the SMBHs is presented. The chapters of the Thesis are organized as follows:

Chapter 1 starts with an introduction to cosmic history and formation of large scale structures. Then a brief discussion about the black holes is presented, with emphasis on the problem of the formation of the first SMBHs. Different formation scenarios for the first black hole seeds are presented. Then two main formation scenarios which are relevant to this thesis are discussed: 1) the direct collapsed black hole (DCBH) scenario and 2) stellar collision and gas accretion in NSCs. After the introductory chapter, the original work developed during the Ph.D. is presented in the remaining three chapters.

Chapter 2 describes how the observed quasar luminosity function (QLF) can be fitted with a tapered power law whose parameters are determined by the formation and growth history of the DCBHs. The model's ability to describe the QLF with an inferred formation history that is aligned with some theoretical ideas of DCBH formation adds support to the DCBH formation scenario for SMBHs.

Chapter 3 describes the formation of massive black hole seeds via stellar collisions and gas accretion in NSCs. We find that this scenario for the formation of SMBHs also works in some limits.

Chapter 4 extends the model in Chapter 3 by adding mass loss due to stellar winds. We estimate its additional effect on the final mass of the black hole seeds created inside the NSCs

via stellar collisions and gas accretion.

1.0.1 Cosmic History

Before describing the physics of Black Holes, it is worthwhile to briefly review our current understanding of the universe in more detail, highlighting the poorly constrained parts that remain to be filled. Briefly we can divide the history of our universe into four epochs, each described below: the early universe, the "dark ages," the epoch of reionization (EoR), and the post-reionization or modern epoch.

The Early Universe

Although this epoch is the farthest from the current epoch, our knowledge of the early universe is fairly good. Measurements of the abundances of the elements produced during Big Bang nucleosynthesis and observations of the fluctuations in the CMB (380,000 yr after the Big Bang or redshift $z \sim 1100$) helped us to understand this epoch. In the standard model, these fluctuations are seeded by quantum fluctuations during a period of expansion known as "inflation". Measurements of the temperature and polarization angular power spectra of the CMB are extremely well described by such inflationary models. The Planck Mission (Planck Collaboration et al., 2016) has done an incredible job to constrain various parameters through the measurement of the CMB. However, at the largest scales Planck is cosmic variance limited i.e. there is a limiting precision with which anisotropies can determine the amplitude of primordial mass fluctuations. This is due to the fact that the surface of last scatter (SLS) probes only a finite two-dimensional slice of the Universe. Probing other SLSs observed from different locations in the Universe would reduce the cosmic variance. Observations of 21-cm emission[1] from the dark ages may be the most promising tool for measuring more modes of the primordial power spectrum and reducing the cosmic variance limit. However, it will be an extremely challenging job to do these measurements.

The Dark Ages

The so-called cosmic dark ages begin after the emission of CMB ($z \sim 1100$) and end with the formation of the first stars and galaxies ($z \sim 10-30$). Theoretically the physics of the dark ages is simple compared to the other three epochs. The seeds of the gravitational fluctuations planted by inflation continue to grow and accrete baryons freed at the last scattering. Eventually the structures go nonlinear, and collapse into objects such as stars and galaxies. These luminous structures start to emit light and the dark ages come to an end.

Although the dark ages are theoretically very well understood, they are observationally really poorly constrained due to the fact there are no luminous objects in this epoch. The upcoming James Webb Space Telescope (JWST) may be able to detect the first proto-galaxies from the end of the dark ages, but the bulk of this era may only be probed using highly redshifted 21-cm

---

[1]21-cm line is the electromagnetic radiation spectral line which comes from the transition between the two levels of the hydrogen 1s ground state. This electromagnetic radiation has the vacuum wavelength of 21-cm in free space.

observations. The dark ages are potentially rich with exotic physics, such as the signature of a decaying dark matter particles or deviations from the Gaussian perturbation spectrum predicted by inflation. The cosmological 21-cm signal will help us to understand these exotic physical phenomena.

1.0.2   Formation of first structures

The formation of the first large-scale structures in the Universe was associated with the collapse of dark matter halos starting from the primordial density fluctuations, left-overs of the inflationary period. The first star formation, instead, is linked to the fate of baryons which collapsed under the gravitational effect of the dark matter. This collisional process resulted in the formation of the first generation of stars, named Pop III. Astronomers generally classify stars as either Population I (Pop I, metal-rich) or Population II (Pop II, metal-poor). However, even the most metal-poor Pop II stars have metallicities way above that of the primordial gas from the Big Bang. For this reason Population III (Pop III) stars were introduce which are composed entirely of primordial gas i.e. hydrogen, helium and very small amounts of lithium and beryllium which are left over from the Big Bang. Many advancements have been made in the field of the first star formation, nonetheless the physics of the fragmentation process and its relationship with the thermodynamical conditions of the gas are still not fully understood. More details can be found in Baraffe et al. (2001a).

Pop III stars are thought to be very different from local stars. They were characterized by (i) very low metallicities, (ii) large masses, (iii) high surface temperatures. Their metallicity should be comparable with the one produced during the Big Bang, i.e. $Z \sim 10^{-10}$. For comparison, the metallicity of standard Pop II stars is nowadays $Z \sim 10^{-3} - 10^{-4}$. The temperature of the Universe during the period when Pop III stars formed was much higher than the mean present-day value. Since the Jeans mass M_J (i.e. the minimum mass needed for a molecular cloud to collapse and form a bounded object) scales with the temperature as $M_J \propto T^{3/2}$ the characteristic mass scale of these first stars are $\sim 10^2 - 10^3 \, M_\odot$ which is large compared to the present-day value. In addition, the large masses are also due to the lack of metal cooling agents, which drives to a fragmentation only occurring into relatively large units. Only massive stars, reaching very high temperatures and densities, are able to produce enough energy by nuclear fusion through the p-p chain. In fact, due to the lack of carbon, nitrogen, and oxygen the CNO cycle was not active in the first stellar population.

In order to collapse, the gas needs to cool. The cooling was mainly driven by radiative de-excitation of molecular hydrogen, H_2 (see Fig. 1.4). Hence, the fate of a gas clump depends on its ability to rapidly increase its H_2 content during the collapse phase. The description of the Pop III star formation needs the understanding of the various channels available for the gas to cool, the evaluation of their efficiency and the modeling of the physical processes that set the mass scale of the fragments.

These unusually massive stars burned their fuel in a short period of time (the stellar lifetime τ is inversely proportional to the cube of its mass:$\tau \propto M^{-3}$): they eventually exploded as supernovae and possibly collapsed into compact objects. The metals produced during the lifetime of

these stars were then dispersed during the supernova explosion, enriching the surrounding gas and opening the way to the next generation of metal-enriched stars (e.g., Loeb & Furlanetto, 2013).

The amount of UV ionizing photons produced by Pop III stars and the fraction that escapes from the star-forming sites (usually named f_{esc}) are fundamental parameters that have to be taken into account to model the evolution of the subsequent phase of the cosmic history: the epoch of reionization. The dark and neutral IGM, as a consequence of the expansion and of the continuous emission of ionizing photons from the Pop III stars, became once again ionized.

Epoch of Reionization (EoR)

The Epoch of Reionization (EoR) is one of the most active fields of research in cosmology today. It occurred roughly between $z \sim 6 - 13$. During this epoch, the ultraviolet emission from early galaxies ionized the intergalactic medium(IGM) and structure formation progressed far enough to profoundly impact the global state of the universe. Studying the EoR helps us to understand the fundamental physics and cosmology of the early universe and the complicated astrophysics of galaxy formation. Measurements of the different conditions during the EoR promise to hold valuable information about the evolution of structure in the universe.

Though the EoR happened recently compared to the other two epochs discussed previously, it is still not well explored. The traditional probes of cosmology at these redshifts are galaxy and quasar surveys, but they have been limited by the difficulties of near-infrared observations. So far, galaxy surveys have been able to find the brightest end of the galaxy population till $z \sim 7$. The quasar spectra are limited by both their intrinsically low space-densities and the rapidly increasing optical depth of the intergalactic medium (IGM). Hence many fundamental questions about the EoR still remain unanswered. When did the reionization of the universe occur? How long did the reionization last? What were the sources of reionization? Were they early star-forming proto-galaxies? Did AGN/quasars play a significant role? What is the role of the Population III stars in reionization compared to the Population II stars? Did feedback from the ionizing background play an important role in the regulation of early galaxy formation? Even though several high resolution numerical simulations (McQuinn, 2012; Iliev et al., 2012) tried to answer these questions, we are still waiting for observational validations.

However a number of studies have been made in recent years to understand the details of the reionization process. The two strongest constraints on reionization come from observations of the Gunn-Peterson effect in the spectra of high redshift quasars (Levshakov & Kegel, 1998; Gunn & Peterson, 1965), and measurements of the optical depth in free electrons (Shull & Venkatesan, 2008). We explain these effects below.

Observations of high-redshift quasars can reveal the presence of neutral hydrogen along the line of sight, which will absorb Lyman-α photons emitted by the quasar. Quasars at redshifts above $z > 5.7$ show a complete absence of transmission in their spectrum immediately redward

of their intrinsic Lyα line (Fan et al., 2001, 2006) also known as the Gunn-Peterson trough[2] (Gunn & Peterson, 1965). The rapid appearance of the Gunn-Peterson feature at higher redshifts tells us the presence of a significant amount of neutral hydrogen above $z \sim 6$. However we need to know the density distribution of the IGM, since neutral fractions of as little as 10^{-4} can result in complete absorption of Lyα photons (Miralda-Escudé et al., 2000). Therefore, these observations only probe the tail of the IGM density distribution.

Another strong constraint comes from measurements of the optical depth of free electrons. Since the CMB is essentially formed when the universe becomes neutral, any Thomson scattering of CMB photons will be from electrons released into the IGM during reionization. These scatterings affect CMB power on large scales — roughly equivalent to the horizon size during reionization. In the temperature anisotropy angular power spectrum, these effects are largely degenerate with other effects. With measurements of the polarization power spectrum, many degeneracies can be broken. The best constraints come from the recent Planck observation which measures $\tau = 0.089^{+0.012}_{-0.014}$ (Planck Collaboration et al., 2016)[3]. This constraint is only an integral measurement (i.e., it is integrated along the line of sights). So the ionization history remains relatively unconstrained.

Combining these two measurements we can get a general picture for reionization: reionization began before $z = 10$ and was likely complete by $z = 6$. However there have been numerous other studies performed which tell us more about the epoch of reionization. A few of these studies are discussed below

1. **Galaxy Counts:** The infrared-sensitive Wide Field Camera 3 (WFC3) installed on the Hubble Space Telescope in 2009, found hundreds of galaxies between $z = 6$ and $z = 9$. The technique used is known as the Lyman break drop-out technique (Finkelstein et al., 2012). A photon emitted with wavelength shorter than Lyman continuum (912) will be completely absorbed by hydrogen gas both in a galaxy and along the line of sight to us. Hence, there will be no light making it to us from a galaxy with wavelengths shorter than that. So we see a "break" (the Lyman break) in the spectrum of the galaxy. For high redshift galaxies, the Lyman break redshifts into the optical. By looking at the colors of galaxies, we should see high redshift star forming galaxies as objects that "disappear" in the bluest filters, or more correctly are red in blue colors. The question is whether the observed galaxy population produces enough photons to reionize the universe or not. To answer this question one requires both a model for converting broad-band photometric measurements into ionizing photon emissivities and a model for the distribution of dense neutral hydrogen clouds in the IGM. However only the brightest galaxies are observed.

---

[2]The Gunn-Peterson trough is a feature in the spectrum of a source near the Lyman α line, caused by the high density neutral hydrogen in the IGM. The background source may be a quasar, but could also be e.g. a gamma-ray burst or just a regular galaxy with a strong Lyα line. Light emitted from these sources in this neutral Universe would be redshifted as it travels through it i.e all light bluewards of Lyα at this redshift would be continually absorbed at each redshift, leaving only flux on the red side of Lyα line. When the reionization is finished, the photons bluer than Lyα at this redshift are unaffected and can travel freely. The result is a deep trough of almost zero flux ranging from Lyα at the redshift of the emitter to Lyα at the redshift where reionization happens.

[3]The optical depth to reionization, τ, is a unitless quantity which provides a measure of the line-of-sight free-electron opacity to CMB radiation.

So the galaxy luminosity function must be extrapolated to significantly lower luminosities to produce enough ionizing photons.

2. **Lyα Emitters:** We can also study the EoR by observing the Lyα emission from high-redshift galaxies (Taniguchi et al., 2003). If the universe is sufficiently neutral, these Lyα photons emitted by the high redshifted galaxies will be absorbed by the IGM. However, if these galaxies reside deep inside ionized bubbles, then the Lyα photons can redshift out of resonance before being absorbed. Large surveys give us the number density of these objects, and their clustering properties will help us to learn about the state of the IGM. Currently two methods are used to survey for Lyα emitters: (1) using narrow band filters targeting emitters at specific redshifts, and (2) spectroscopically targeting Lyman break galaxies to search for the presence of a Ly emission line. The spectroscopic surveys see a significant decline in the fraction of galaxies with visible Lyα emission between redshifts 6 and 7. These observations are consistent with a neutral fraction of between 10% and 50% at $z = 7$.

3. **The Kinetic Sunyaev-Zel'dovich Effect:** Measurements of small scale anisotropies in the CMB created by the kinetic Sunyaev-Zel'dovich (KSZ) effect have the potential to constrain the duration of reionization. In particular, the "patchiness" of the reionization process creates a small spectral distortion when CMB photons scatter off moving electrons These distortions add small scale power to the CMB angular power spectrum which is proportional to the duration of the "patchy" period (McQuinn et al., 2005).

There are a large range of additional techniques that have also been used to probe this epoch, including: direct measurements of the IGM temperature as a function of redshift (Boera et al., 2014), measurements of the Lyα damping wing tails in high redshift gamma-ray bursts (Totani et al., 2014) and measurements of the Cosmic Infrared Background (CIB) (Helgason et al., 2016).

The Post-Reionization Epoch:

The epoch after reionization from $z \sim 6$ to present is really complex. During this epoch small proto-galaxies turn into big galaxies (Loeb & Barkana, 2001). This era is also the most accessible to the current generation of optical/NIR ground and space based telescopes, and hence fairly well understood. However one of the greatest mysteries in modern cosmology also first appears at $z \sim 2$: when the universe started to accelerate, presumably driven by "dark energy". With essentially no theoretical model that can account for the observed strength of dark energy, current measurements are principally trying to answer whether the observed expansion is consistent with a cosmological constant.

One of the most exciting probes for revealing the nature of dark energy are the Baryon Acoustic Oscillation (BAO) features in the large-scale matter distribution (Eisenstein et al., 2005). These features in the cosmic microwave background (CMB) power spectrum and the matter power spectrum today are imprints from the acoustic oscillations in the primordial photon-baryon plasma that recombined at $z \sim 1100$. The features in the power spectrum appear at multiples of the sound horizon scale at recombination, making them effective standard rulers

to measure cosmological expansion.

Having discussed the cosmic history briefly, we will now overview the pathways to the first SMBHs.

1.1   Introduction to Black Holes

A black hole is an object where gravity is so strong that even light can not get out. Generally, black holes are formed by gravitational collapse of heavy objects such as stars. But they can also be formed by other processes. The escape velocity of a black hole:

$$v_{esc} = \sqrt{\frac{2GM_\bullet}{r}}, \tag{1.1}$$

where $M_\bullet$ is the mass and r is the radius of the black hole respectively, is larger than the speed of light c. So even light can not escape from a black hole. A black hole could be fully characterized by three parameters : (i) mass, (ii) spin and (iii) charge (Misner et al., 1973). However, astrophysical black holes, which we are going to discuss about, are neutral. So they can be described only by mass and spin.

The boundary of the region from which no escape is possible is called the 'event horizon' (Rindler, 1956). Light can not escape from the event horizon. However, most luminous light of the Universe could come from outside the event horizon, due the huge energy radiated by the infalling material.

As the material falls into the deep gravitational potential well of the black holes, the gravitational binding energy could be radiated away. The infalling matter could form an external accretion disk around the black holes and heat up by friction. These are known as quasars, some of the brightest objects in the universe. More than $\sim 10\%$ of the accreting matter can be converted into energy which is more than an order of magnitude larger the maximum efficiency of nuclear fusion reaction. The total luminosity L of the black hole can be expressed as:

$$L = \epsilon \dot{M} c^2 \tag{1.2}$$

where ϵ is the efficiency of radiation (generally $\epsilon \sim 0.1$) and $\dot{M}$ is the accretion rate. The black holes accrete the material which is not radiated away:

$$\dot{M}_\bullet = (1 - \epsilon)\dot{M} \tag{1.3}$$

The Black Holes are usually classified into three different categories according to their masses: (i) **Stellar Mass BHs** (ii) **Intermediate Mass BHs** (IMBH) and (iii) **Supermassive BHs** (SMBH) 1.1.

Stellar mass BHs are formed by the gravitational collapse of the massive stars. When massive stars die, the eject most of the materials via supernova explosion. If the remnant is more massive than the so-called Tolman-Oppenheimer-Volkoff (TOV) limit (Zeldovich & Novikov, 1971) , it collapses into a black hole. The calculations for the TOV limit are so complex due

	Mass Range
Stellar Mass BH	$2\,\mathrm{M_\odot} \lesssim M_\bullet \lesssim 100\,\mathrm{M_\odot}$
Intermediate Mass BH	$100\,\mathrm{M_\odot} \lesssim M_\bullet \lesssim 10^6\,\mathrm{M_\odot}$
Supermassive BH	$10^6\,\mathrm{M_\odot} \lesssim M_\bullet \lesssim 10^{10}\,\mathrm{M_\odot}$

Table 1.1: Categories of black holes classified according to their masses.

to uncertainties about the equation of state fore dense nuclear matter that it is difficult to get a precise value. Gravitational wave observations of merging neutron stars suggested a limit of $2.17\,\mathrm{M_\odot}$ (Margalit & Metzger, 2017). Stellar mass black holes binaries could also exist and have been observed via gravitational wave detection (Abbott et al., 2016; Toubiana et al., 2020). The models of stellar evolution predict that black holes with masses in two ranges cannot be directly formed by the gravitational collapse of a star. These two ranges are known as 'lower' and 'upper' mass gaps which are $2-5\,\mathrm{M_\odot}$ and $50-150\,\mathrm{M_\odot}$, respectively (Abbott et al., 2019).

Observations found that almost every galaxy host a SMBH at it's center (Kormendy & Richstone, 1995; Kormendy & Ho, 2013). SMBHs can accrete huge amount of gas. The galactic cores hosting these type of SMBHs are known as 'active galactic nuclei (AGN)'. SMBHs can also be minimally active e.g. our own galaxy, the Milky Way. An accreting SMBHs emits huge amounts of radiation which have been observed in the past decades in different galaxies at different cosmic epoch (Kulkarni et al., 2019), see fig. 1.2

SMBHs have been also found beyond the AGN population e.g. the SMBH Sagittarius A^* at the center of our own Galaxy. Stars are observed to orbit around the Sagittarius A^* with velocities up to $10^5\,\mathrm{km s^{-1}}$. The high velocities are due to the strong gravitational field near the Sagittarius A^* whose mass is $\sim 4\times 10^6\,\mathrm{M_\odot}$ (Schwarzschild, 1916; Schödel et al., 2002).

AGN surveys suggests AGNs are rare to observe as they are short lived (50 - 100 Myr). SMBHs show AGN activity only when they are accreting matter. When the gas surrounding the SMBH is already depleted via accretion or even expelled from the galaxy by the radiative feedback of the SMBH, through powerful outflows, the AGN activity is ceased. AGN activities release huge amount of energies to the surrounding galaxy through gas outflows and radiation. The energy released by SMBH is comparable to its gravitational binding energy which roughly 10^6 times the binding energy of the galaxy. Therefore, SMBHs can potentially change the global properties of their host galaxies with their energy release. This is also knows as 'AGN feedback'.

1.2 Space time metric around a black hole

We now discuss mathematical description of the black holes, which requires the use of General Relativity. The gravitational field outside a non-rotating spherical mass in the vacuum is
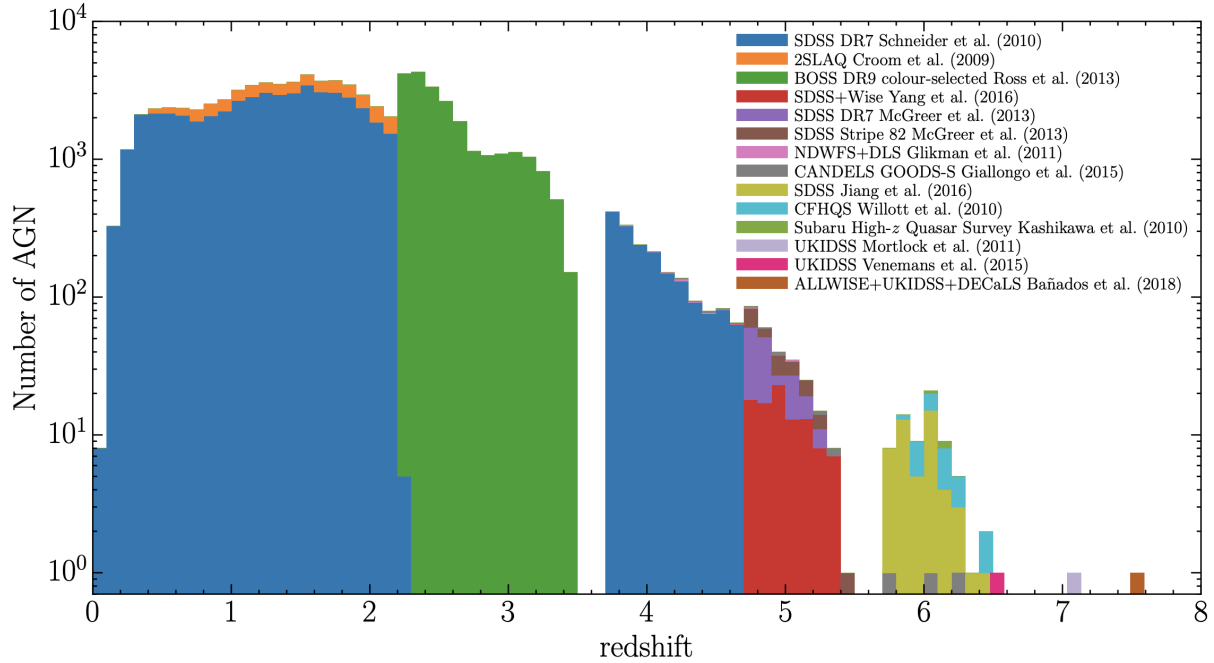
Figure 1.2: Redshift distribution of the AGNs found in different surveys. Figure taken from Kulkarni et al. (2019)

.

described by the Schwarzschild metric (Schwarzschild, 1999):

$$ds^2 = -c^2 d\tau^2 = -\left(1 - \frac{R_S}{r}\right)c^2 dt^2 + \left(1 - \frac{R_S}{r}\right)^{-1} dr^2 + r^2(d\theta^2 + \sin^2\theta d\phi^2), \qquad (1.4)$$

where τ is the proper time i.e. the time measured by a clock moving with the particle, t is the coordinate time i.e the time measured by a stationary clock at infinity, r is the radial coordinate , θ is the polar angle, ϕ is the azimuthal angle and R_S is the Schwarzschild radius which is related to the mass of the black hole as:

$$R_S = \frac{2GM_\bullet}{c^2} . \qquad (1.5)$$

This radius defines the horizon of the black hole also known as the **"event horizon"**. Nothing can escape the event horizon of a black hole.

The space-time metric a spinning black hole was derived in 1963 by Kerr (Kerr, 1963). The Kerr metric is an exact solution of the Einstein field equations of general relativity. It is extremely difficult to find the exact solutions of these equations due to the highly non-linear nature. If J the angular momentum of the spinning black hole then the dimensionless ratio $a = J/\frac{GM_\bullet}{c^2}$ is known as the spin parameter and it ranges between 0 and 1.For a Schwarzschild (non-spinning) black hole $a = 0$. For a maximally-rotating black hole $a = 1$ (Thorne, 1974).

The orbit followed by photons or massive particles around the black hole is determined by it's spin. Hence the spin parameter will have a strong impact on the efficiency (ϵ) of the radiation. The radius of the circular orbit followed by a photon around a black hole of mass $M_\bullet$ with a spin parameter a is given by (Teo, 2003):

$$r_{\mathrm{ph}} = R_{\mathrm{S}} \left[1 + \cos \left(\frac{2}{3} \cos^{-1} \left(\frac{\pm |a|}{M_\bullet} \right) \right) \right] , \tag{1.6}$$

where the plus sign refers to retrograde orbits and the minus sign refers to prograde orbits. These are also known as 'Boyer–Lindquist-radii'. For a Schwarzschild black hole $r_{\mathrm{ph}} = \frac{3}{2} R_{\mathrm{S}}$.

The smallest marginally stable circular orbit in which a massive test particle can stably orbit a massive object such as a black hole is know as the Innermost Stable Circular Orbit (ISCO) (Misner et al., 1973). At smaller radii, massive particles plunge into the black hole on a dynamical time scale. The smaller the ISCO, the larger is the fraction of gravitational energy radiated away and hence, the higher is the radiative efficiency ϵ. The radius of the ISCO is given by (Bardeen et al., 1972):

$$r_{\mathrm{ISCO}} = \frac{1}{2} R_{\mathrm{S}} [3 + Z_2 \pm [(3 - Z_1)(3 + Z_1 + 2Z_2)]^{1/2}] , \tag{1.7}$$

where Z_1 and Z_2 are function of a. The radiative efficiency ϵ is expressed as (Loeb & Rasio, 1994):

$$\epsilon = 1 + \frac{r^2 - R_{\mathrm{S}}r \pm j\sqrt{0.5R_{\mathrm{S}}r}}{r \left(r^2 - \frac{3}{2}R_{\mathrm{S}}r \pm 2j\sqrt{0.5R_{\mathrm{S}}r} \right)^{1/2}} , \tag{1.8}$$

where ϵ ranges from $\sim 5.72\%$ for a Schwarzschild ($a = 0$) black hole to $\sim 42.3\%$ for a maximally rotating ($a = 1$) black hole with prograde orbit. ISCO of a rotating black hole depends on whether the orbit is prograde or retrograde. As the rotation rate of the black hole increases the retrograde ISCO increases while the prograde ISCO decreases. For a Schwarzschild black hole, ISCO is located at $r_{\mathrm{ISCO}} = 3R_{\mathrm{S}}$.

1.3 Accretion rate of black holes

The first accretion model onto a black hole is given by the Eddington rate (Frank et al., 2002). This can be derived from balancing the inward force of gravity on each proton by the outward radiative force on its companion electron at a distance r from the center. The gravitational force is given simply via:

$$F_{\mathrm{grav}} = \frac{GM_\bullet m_{\mathrm{p}}}{r^2} . \tag{1.9}$$

The radiation pressure at a distance R is given by:

$$P_{\mathrm{rad}} = \frac{L}{c} \frac{1}{4\pi R^2} , \tag{1.10}$$

where L is the luminosity of the black hole. In order to calculate the radiation force, we need its opacity, κ. Radiation pressure is force per unit area; opacity is the cross-sectional area per unit mass for radiation scattering.

$$F_{\text{rad}} = P_{\text{rad}}\kappa m_{\text{p}} . \tag{1.11}$$

Balancing the two forces gives:

$$\frac{GM_{\bullet}m_{\text{p}}}{r^2} = \frac{L}{c}\frac{\kappa m_{\text{p}}}{4\pi R^2} . \tag{1.12}$$

At high temperature, the accreting material is mostly ionized hydrogen and the opacity is provided by Thomson scattering. The cross-section will then come almost exclusively from radiation pressure on the electrons, but the mass lies almost exclusively in the protons. Thus $\kappa = \sigma_{\text{T}}/m_{\text{p}}$ where σ_{T} is the Thompson cross section. Then from eq. 1.12 we get,

$$L_{\text{Edd}} = \frac{4\pi GMcm_{\text{p}}}{\sigma_{\text{T}}} . \tag{1.13}$$

Note that the Eddington luminosity derivation assumes that the ions and electrons move together because they are held together by their electrostatic attraction.

Now lets assume the black hole is accreting at a rate $\dot{M}$. Some fraction of the gravitational potential energy can be radiated away. If we express this as a fraction of the rest-mass energy, then the luminosity radiated away becomes

$$L = \epsilon\dot{M}c^2 . \tag{1.14}$$

Equating the above equation with eq. 1.13 one can write the Eddington accretion rate as:

$$\dot{M}_{\text{Edd}} = \frac{4\pi GMm_{\text{p}}}{\epsilon c\sigma_T} = 2.2 \times 10^{-8}\left(\frac{M_*}{\text{M}_\odot}\right)\ \text{M}_\odot\text{yr}^{-1} . \tag{1.15}$$

Finally we consider the Bondi-Hoyle-Lyttleton accretion. Simulations (Bonnell et al., 2001) have shown that in larger clusters the stars accrete unequally, with the stars near the core accreting more than those near the outer envelopes of the cluster. This is due to the fact that the gas mass is accumulating near the core due to the cluster potential where it can be accreted by the stars. Even initially uniform clusters show a position dependent accretion as the gas and stars redistribute themselves in the host cluster potential. As a result of the position-dependent accretion, the final configurations show a significant amount of mass segregation.

In principle the accretion rate of a star will depend on its cross section πR_{acc}^2, where R_{acc} is the accretion radius, on the gas density ρ_∞, and the relative velocity of the star with respect to the gas v_∞, as

$$\dot{M} = \pi v_\infty\rho_\infty R_{\text{acc}}^2. \tag{1.16}$$

In the original Hoyle–Lyttleton (HL) problem the accretion radius in the supersonic regime is given as (Hoyle & Lyttleton, 1939, 1940a,b)

$$R_{\text{HL}} = \frac{2GM}{v_\infty^2}, \tag{1.17}$$

which leads to the HL accretion rate:

$$\dot{M}_{HL} = \frac{4\pi G^2 M^2 \rho_\infty}{v_\infty^3}. \tag{1.18}$$

However, (Bondi, 1952) defined the Bondi radius as

$$R_B = \frac{GM}{c_S^2}. \tag{1.19}$$

The flow outside this radius is subsonic and the density is almost uniform, while inside the Bondi radius the gas becomes supersonic. This led (Bondi, 1952) to propose an interpolated Bondi-Hoyle (BH) formula:

$$\dot{M}_{BH} = \frac{2\pi G^2 M^2 \rho_\infty}{(v_\infty^2 + c_S^2)^{3/2}}. \tag{1.20}$$

Studies have shown that there will be an extra factor of 2 which leads to the final accretion formula given as

$$\dot{M}_{BH} = \frac{4\pi G^2 M^2 \rho_\infty}{(v_\infty^2 + c_S^2)^{3/2}}. \tag{1.21}$$

This accretion rate can be written as in Eq. 2 of (Maccarone & Zurek, 2012):

$$\dot{M}_{BH} = 7 \times 10^{-9} \left(\frac{M}{M_\odot}\right)^2 \left(\frac{n}{10^6 \, \text{cm}^{-3}}\right)^2 \left(\frac{\sqrt{c_S^2 + v_\infty^2}}{10^6 \, \text{cm s}^{-1}}\right)^{-3} M_\odot \text{yr}^{-1}.$$

Assuming typical values for the core of the nuclear clusters with $n \sim 10^6 \, \text{cm}^{-3}$, $c_S \sim 10^6 \, \text{cm s}^{-1}$ (for a core gas temperature of $\sim 10^3$ K), we can write the BH **accretion** rate in a simplified way (Leigh et al., 2013a):

$$\dot{M}_{BH} = 10^{-9} \left(\frac{M}{M_\odot}\right)^2 M_\odot \text{yr}^{-1}. \tag{1.22}$$

1.4   Accretion Disks

Black holes are usually accompanied by their accretion disks. The accretion inflow has a non-zero angular momentum with respect to the black hole. Hence, the gas will reach a centrifugal barrier. The gas can be accreted further inward only if its angular momentum is transported away. This is due to the fact the centrifugal acceleration has a radial scaling $\sim r^{-3}$ whereas the gravitational acceleration has a radial scaling ($\sim r^{-2}$). Hence, for smaller radii, the centrifugal acceleration increases faster than the gravitational acceleration. The accretion disk forms on a plane perpendicular to its rotation axis. The accretion timescale is determined by the time needed to transport away the angular momentum which be significantly larger than the free-fall time. Accretion regimes are categorized into two different disk regimes: (i) the thin disk regime and (ii) the thick disk regime.

Thin disks are made of relatively cold gas, with a negligible radiation pressure. In the thin disk regime the cooling time of the gas is shorter than the viscous time. The angular momentum of the gas is transported away by both the gas viscosity and by magneto-rotational instability effects (Chandrasekhar, 1960). The gas inflow rate in thin disk regime is roughly $\dot{m} \equiv \dot{M}/\dot{M}_E > 10^{-2}$. Thin disks are relatively luminous and usually found in AGNs. The electromagnetic spectrum emitted from the thin disks regime are estimated by the radial temperature distribution of the disk. It is possible to show that the temperature profile is given by (Loeb & Furlanetto, 2013)

$$T_d \approx 10^5 \left(\frac{M_\bullet}{10^8\,\mathrm{M}_\odot}\right)^{\frac{-1}{4}} \left(\frac{\dot{m}}{0.1}\right)^{\frac{1}{4}} \left(\frac{r}{10R_S}\right)^{\frac{-3}{4}} \left[1 - \left(\frac{r}{r_{\mathrm{ISCO}}}\right)^{\frac{1}{2}}\right] \mathrm{K}, \qquad (1.23)$$

where r_{ISCO} is given by Eq. 1.7. The disk surface temperature increases with decreasing mass. Hence, it reaches the X-rays regime in the case of stellar mass black holes. The accretion disks around smaller black holes are generally hotter. For SMBHs, the accretion disk can be divided radially into three distinct regions: (i) the inner region where radiation pressure and electron scattering opacity dominate, (ii) the middle region where gas pressure and electron scattering opacity dominate and (iii) the outer region where gas pressure and free-free opacity dominate.

When the accretion flow sub-Eddington value ($\dot{m} \equiv \dot{M}/\dot{M}_E < 10^{-2}$) the gas inflow switches to the so-called advection-dominated accretion flow (ADAF). ADAFs are cooled by advection process rather than by radiation. ADAFs very radiatively inefficient and geometrically extended, similar to a sphere rather than a disk. Their analytic description is much more complex than in the thin regime. Most of the local SMBHs are characterized by a very low accretion rate due to the deficiency of gas reservoir due to lack of major merger events and star formations. Hence, the SMBHs are described by the thick disk model. The accretion timescale (~ 100 Myr) in thick disk regime is orders of magnitude longer than the thin disk regime .

Theoretical and observational studies suggest that accretion rates can exceed the Eddington rate ($\dot{M} > \dot{M}_E$, i.e. super-Eddington accretion) (Volonteri & Rees, 2005; Alexander & Natarajan, 2014; Madau et al., 2014; Volonteri et al., 2015; Pacucci et al., 2015, 2017; Begelman & Volonteri, 2017; Takeo et al., 2020). There are three different possibilities what happens when the accretion rate is super-Eddington. First possibility is that the gas accretes and radiates with high efficiency, and that the black hole therefore shines at a super-Eddington luminosity ($L >> L_{\mathrm{Edd}}$). A second possibility is that even if the accretion rate is super-Eddington, the efficiency is low and hence $L \leq L_{\mathrm{Edd}}$. Third possibility is that resulting flow may drive most of the gas out, so that the actual accretion rate is sub-Eddington.

1.5 The first black holes in the universe

In this section we discuss why the observed SMBHs at high redshifts challenge the standard theory of black hole growth. Then, we discuss different theories for the formation of the first black holes.

1.5.1 The problem of the early super-massive black holes

The observation of more than two hundred supermassive black holes (SMBHs) with masses $\gtrsim 10^9\,M_\odot$ at redshift $z \gtrsim 6$(1.3) (Fan et al., 2001; Willott et al., 2010; Mortlock et al., 2011; Wu et al., 2015; Bañados et al., 2018; Matsuoka et al., 2018; Wang et al., 2019; Shen et al., 2019; Matsuoka et al., 2019) has challenged our general understanding of black hole growth and formation. How these massive objects formed and grew over cosmic time is currently one of the biggest puzzles in astrophysics (Smith & Bromm, 2019; Inayoshi et al., 2019; Latif & Schleicher, 2019). With the observations of these supermassive black holes, the idea of SMBHs only existing in our local neighbourhood suffered a huge paradigm shift. The age of the Universe, t_{age}, at $z = 6$ is ~ 930 Myr, and the first stars are believed to be formed around $z \sim 30$ (Baraffe et al., 2001b) when the age of the universe was $t_{age} \sim 100$ Myr , that leaves only ~900 Myr for a SMBH to form and have grown from a stellar mass BH.
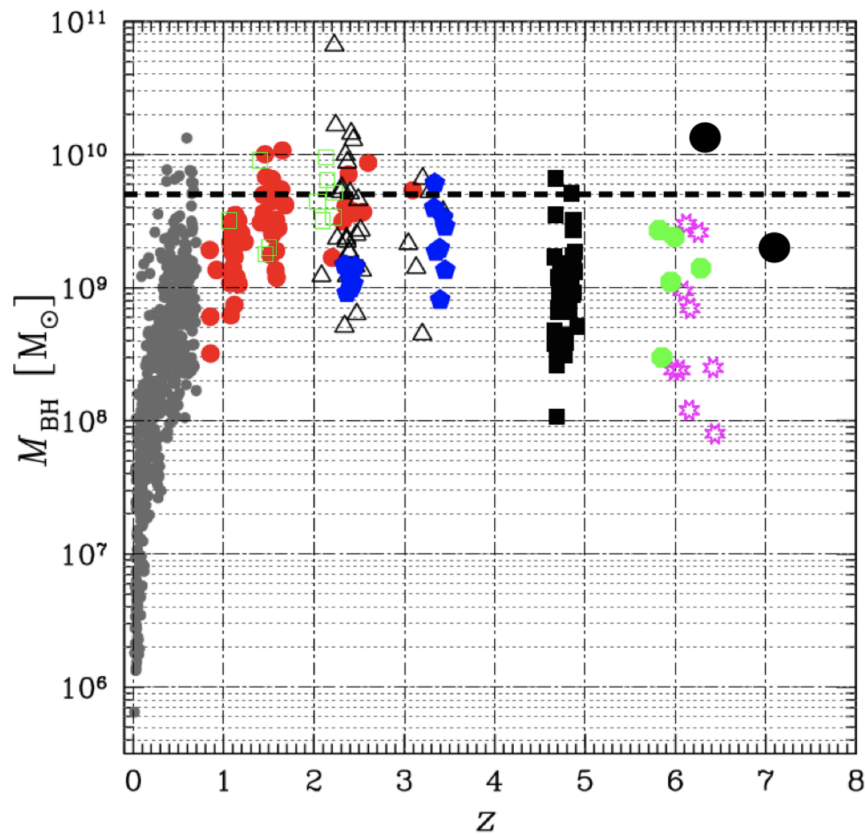
Figure 1.3: The massive black holes discovered so far, shown as a function of their redshift and estimated mass. A small group of these objects is at very high redshifts ($z \gtrsim 6$), and they have very large masses, in excess of about $10^8\,M_\odot$. Figure taken from (Marziani & Sulentic, 2012)

Eq. 3.6 can be expressed in terms of the Eddington fraction, f_{Edd}:

$$f_{\text{Edd}} = \frac{L}{L_{\text{Edd}}} \, , \tag{1.24}$$

where at $f_{\text{Edd}} = 1$, the Eddington luminosity limit is reached. For super-Eddington rate $f_{\text{Edd}} > 1$. Equating eqs. 1.14 and 1.24, we get:

$$\dot{M}_{\text{Edd}} = f_{\text{Edd}} \frac{4\pi G M m_{\text{p}}}{\epsilon c \sigma_T} \, . \tag{1.25}$$

Solving the above differential equation:

$$M(t) = M_0 \exp\left(f_{\text{Edd}} \frac{1 - \epsilon}{\epsilon} \frac{t}{450\text{Myr}} \right) \, , \tag{1.26}$$

where the Salpeter time, $t_{\text{S}} = \frac{\sigma_T c}{4\pi G m_p} = 450\,\text{Myr}$, appears in the denominator of the exponential.

1.5.2   Stellar mass black hole seeds

One possible way to describe the formation of the first quasars is by considering the stellar mass black hole seeds which are the remnants of Pop III star. These seeds can grow via gas accretion. Pop III stars with masses in the range $M_* \sim 30 - 100\,\text{M}_\odot$ and $M_* \gtrsim 250\,\text{M}_\odot$ could end up as BHs with similar masses as their stellar progenitors. From eq. 1.26 it can be shown that if a stellar mass black hole of mass $\sim 100\,\text{M}_\odot$ is formed at $z > 15$ and constantly accretes at $f_{\text{edd}} = 1$, it may grow to $10^9\,\text{M}_\odot$ by $z = 6$. However, there are few challenges to overcome.

1. The first Pop III stars likely formed in haloes with masses $\sim 10^{5-6}\,\text{M}_\odot$ and gas masses in the range $\sim 10^{4-5}\,\text{M}_\odot$. Once the black hole accretes all the gas inside the halo, it is unclear where the gas required for further accretion comes from. One possible solution is galaxy mergers (Capelo et al., 2015; Volonteri et al., 2016; Pacucci & Loeb, 2020). However, note that depending on the masses of the merging systems, the merging time scale could be of the order of the age of the universe .

2. The black hole itself would produce feedback which could heat up the accreting gas resulting into inefficient accretion. Also, the radiation–feedback from the Pop III star induce negative feedback in the surrounding gas.

3. Gravitational recoil may also interrupt the growth process. The amplitude of the gravitational recoil spin and mass of the merging black holes. The recoiled velocity could be of the order of hundreds of kilometers per second which is much higher than the typical escape velocity of a high redshift galaxy. So, the recoil induced by gravitational wave emission can unbind the merger remnants from the shallow potential wells of their host galaxies and hence the mass inflow is abruptly quenched (Haiman, 2004).

Possible solutions are higher accretion rates or massive seed black holes.

1.5.3 Formation of the first black holes

We have discussed in the previous section that black hole masses of $\sim 10^9\,M_\odot$ at $z \sim 6$ starting from stellar mass seeds are difficult to form with the Eddington rate. Two possible solutions are higher accretion rates or massive seed black holes.

- **Massive Seeds:** In this scenario, a large black hole seed of mass up to $\sim 10^{4-5}\,M_\odot$ is formed. These seeds can easily grow upto $10^9\,M_\odot$ stage at $z \sim 6$ with Eddington accretion rate.t here are different models to explain the formation of these massive black hole seeds. In this thesis we are going to discuss two of the most promising models: 1)The direct collapsed black hole (DCBH) scenario where conditions (high inflow rates at the center of the collapsing halo) a super-massive star is formed (Ferrara et al., 2014) which can be collapsed into a similar mass black hole, 2) Formation of massive seeds via gas accretion and runaway collisions in dense stellar cluster. The predicted masses of the black hole seed are different for different models.

- **Super-Eddington accretion rate** : An alternate solution relies on super-Eddington accretion (Volonteri & Rees, 2005; Alexander & Natarajan, 2014; Madau et al., 2014; Volonteri et al., 2015; Pacucci et al., 2015; Begelman & Volonteri, 2017; Takeo et al., 2020). The accretion disks of the black holes could be radiatively inefficient, making the trapping of photons dynamically important (Abramowicz et al., 1988; Paczynski & Abramowicz, 1982; Mineshige et al., 2000; Sądowski, 2009; Sadowski, 2011; McKinney et al., 2014, for the slim disk model). If a large fraction of photons is trapped inside the accretion disk, the effective radiation pressure acting on the surrounding gas is decreased which may lead to accretion rates that are several times larger than the Eddington rate. Unlike the case of stellar mass BH seed, a temporary non-availability of gas is less of a problem in this scenario, as it can be compensated via highly efficient accretion at other times. However, ensuring a sufficiently high streaming efficiency of the gas from the large-scale reservoir down to horizon scales is difficult to achieve because accretion flows onto seed BHs might be reduced by their own radiation (Milosavljević et al., 2009; Sugimura et al., 2018; Regan et al., 2019) and due to the inefficient gas angular momentum transfer (Inayoshi et al., 2018a; Sugimura et al., 2018).

1.5.4 Direct Collapsed Black Holes

The DCBH scenario was first suggested by (Bromm & Loeb, 2003) . This provides one of the possibilities to form high-mass black hole seeds at high redshifts. The basic idea is that a gas cloud in a massive halo with virial temperature $T \gtrsim 8000$ K and no H_2 molecules or metals present inside the gas cloud can collapse without fragmentation directly into a SMS which can collapse into seed black holes of similar mass after their lifetime. This model is extremely promising as it is based the physical conditions of the early Universe. The predicted observational signals are expected to be observed with the current and upcoming surveys.

Cooling processes are key in order to form a gravitationally bound object. Atomic and molecular hydrogen are two of the most important coolants during in the early universe (see fig.
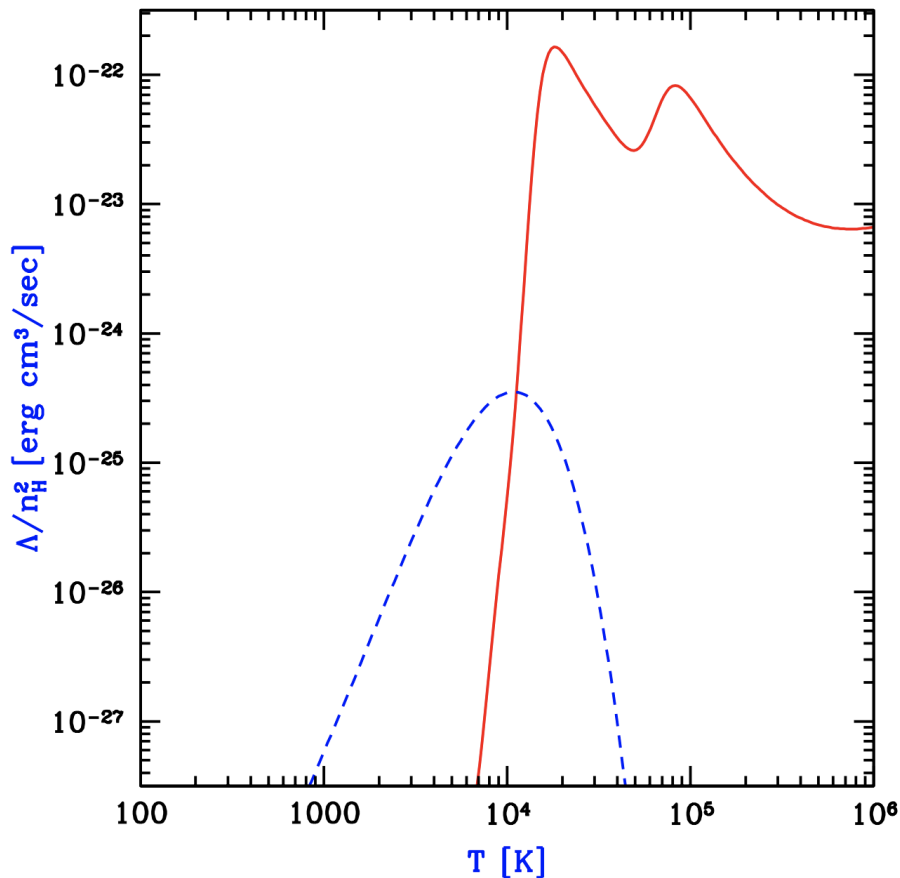
Figure 1.4: Cooling rates as a function of temperature for a primordial gas composed of atomic hydrogen and helium, as well as molecular hydrogen, in the absence of any external radiation. The solid line shows the cooling curve for an atomic gas, with the characteristic peaks due to collisional excitation of H I and He II. The dashed line shows the additional contribution from molecular cooling. Image taken from Baraffe et al. (2001a)

.

1.4). Hence, one of necessary conditions to allow for the collapse of high-mass halos in the early Universe is the existence of a strong Lyman Werner flux J_{LW} which destroys the H_2 molecules. As a result the molecular H_2 cooling is quenched and the halo fragments into smaller clumps. The precise value of the threshold J_{LW} depends on multiple factors e.g. radiative transfer, the chemistry and the spectral shape of the sources which are only poorly constrained due to lack of observational evidences. Theoretical studies and simulations have found that $30 < J_{LW}^{th} < 1000$ in units of 10^{-21} erg s^{-1} cm^{-2} Hz^{-1} sr^{-1} (Agarwal et al., 2012; Latif et al., 2013; Ferrara et al., 2014). Even though the presence of such a strong background radiation is rare, it may be possible to find such conditions (Visbal et al., 2014; Dijkstra et al., 2014; Regan et al., 2017). Recent studies by Wise et al. (2019) and Regan et al. (2020b) have shown that atomic cooling haloes can satisfy above requirements. Wise et al. (2019) have shown that the requirement of the high UV flux can be significantly reduced in halos with rapid merger histories (Inayoshi

et al., 2018b) and in halos located in regions of high baryonic streaming velocities (Naoz et al., 2013; Hirano et al., 2017).

A collapsing metal-free, atomic cooling halo, embedded in a LW flux $J_{LW} > J_{LW}^{th}$, may follow two different pathways to form an IMBH at high redshift (Ferrara et al., 2014). The formation process of the black hole seed starts with the growth of a proto-SMS inside metal-free atomic cooling halos embedded in a strong LW radiation field. The collapse is isothermal and coherent, with accretion rates comparable or larger than the thermal accretion rate (Shu, 1977; Ferrara et al., 2014):

$$\dot{M} = \frac{\pi^2}{8G}c_s^3 \approx 0.162 \left(\frac{T}{10^4 \text{K}}\right)^{3/2} \text{ M}_\odot \text{yr}^{-1}\,. \tag{1.27}$$

where c_s is the speed of sound. With this accretion, it will take only $\sim 10^5$ yr to build a $\sim 10^4\,\text{M}_\odot$ SMS.

Another necessary requirement is high inflow rate ~ 0.1 M$_\odot$yr^{-1} which can be obtained easily in metal free halos (Agarwal et al., 2012; Latif et al., 2013; Shlosman et al., 2016; Regan & Downes, 2018; Becerra et al., 2018; Chon et al., 2018; Agarwal et al., 2019; Latif et al., 2020). The high inflow rate could be blocked by two factors: (i) accretion of polluted gas which might be brought by minor mergers or smooth accretion from the IGM. Metal line cooling will lead to the fragmentation of the gas into clumps and they cannot be accreted as their angular momentum is hard to dissipate (ii) Major mergers which might disrupt the smooth accretion flow onto the central proto-SMS star due to turbulence. These mergers were very common in the early Universe, when these DCBH seeds were formed.

If the accretion flow is disrupted the star stops accreting and rapidly evolves towards a very hot Zero Age Main Sequence (ZAMS) SMS which can emit huge amount of UV radiations which will clear out remaining gas out of the potential well of the hosting halo. After a very brief lifetime ($\lesssim 1$ Myr) (Umeda et al., 2016) the SMS collapses and leaves a black hole seed with similar mass of the SMS. On the other hand, the high accretion rate can be maintained for a longer time, the star can continue to grow. In this radiative feedback is unable to stop the halo gas from accreting due to low effective temperature. The growth continues until the object finally encounters a General Relativistic (GR) instability[4]. The GR instability results into a rapid ($\sim 10^5 s$) direct collapse into a black hole. The name is due to the fact that it collapses directly into a black hole without passing through a normal stellar phase unlike the formation of stellar mass black holes. Ferrara et al. (2014) have found the limiting mass of the non-rotating proto SMS :

$$M_{GR} \approx 8.45 \times 10^5 \left(\frac{\dot{M}}{1\,\text{M}_\odot\text{yr}^{-1}}\right)^{2/3} \text{ M}_\odot\,. \tag{1.28}$$

---

[4]In the case of non-relativistic gravitational equilibrium, an instability of a star occurs when the adiabatic exponent is smaller than 4/3. This happens due to endothermic phase transition of the constituent matter are caused by the dissociation of hydrogen molecules, ionization of atoms, electron pair creation, dissociation of the Fe nucleus and so on. On other hand, in case of general relativistic equilibrium this criterion is revised so that an instability occurs even when adiabatic exponent is greater than 4/3. For SMS the general relativistic effect becomes significant since the Schwarzschild radius increases with mass and gets to be of the same order as the stellar radius.

The two cases are strongly different. Since the collapse is isothermal and the temperature is kept at low levels, virtually no ionizing photons are produced in the second one. Therefore, the DCBH will be embedded in the gas reservoir of the halo and continue to accrete. This accretion phase remains highly obscured. During the latest phases the DCBH might be able to clear the remaining gas by photoionizing and heating. The DCBH at that point can fully grow into a IMBH or SMBH.

The presence of even tiny amounts of metals can trigger strong fragmentation through metal line cooling (Omukai et al., 2008; Dopcke et al., 2011; Latif et al., 2016; Corbett Moran et al., 2018; Chon & Omukai, 2020) and reduce the infall rate.However, Chon & Omukai (2020) have recently shown that even in just slightly metal enriched halos ($Z < 10^{-3}$ $Z_\odot$), where fragmentation takes place, the central massive stars could be fed by the accreting gas and grow into SMSs. Regan et al. (2020a) also have shown that SMSs could still be formed in atomic cooling haloes with higher metal enrichment ($Z > 10^{-3}$ $Z_\odot$) in the early universe due to inhomogeneous metal distribution.

Studies Yue et al. (2014); Dijkstra et al. (2014) suggest that the formation of DCBHs was possible only during a brief era of cosmic evolution, between $z = 20$ and $z = 13$. After this time, the gas in the potential formation sites might photo-evaporated.

1.6   Formation of SMBH in dense stellar clusters

Galactic centers are considered as the most favorable places for SMBH formation. Gaseous and stellar material without the orbital support will falls on to the deepest part of the galactic gravitational potential (Escala, 2006). Various processes e.g. gravitational torques in galaxy mergers (Mayer et al., 2010), clump migration by dynamical friction (Escala, 2007) and bars within bars (Hopkins & Quataert, 2010) produce strong inflows at galactic scales on dynamical timescales [5]. These processes funnel large amount of gaseous material of mass $\sim 10^{10}\,\mathrm{M_\odot}$ to the galactic center. These processes are expected to be more dominant at high z, because of the higher gas fractions and the absence of AGN feedback from preexisting SMBHs (Prieto & Escala, 2016). The absence of feedback limiting factors (Prieto et al., 2017) will result in high amount of material funneled into galactic nuclei without any upper limit externally set by processes at galactic scales. Thus, galactic centers are expected to be hosting the densest gaseous and stellar configurations in the universe. One key question is if these materials do not end up forming a SMBH then what other stable configuration they could form?

One possible stable configuration could be the formation of a Very Massive quasi-Star (VMS) (Volonteri, 2010; Schleicher et al., 2013) which could collapse into a MBH due to post Newtonian instability (Tolman, 1934; Oppenheimer & Volkoff, 1939). This could happen under very efficient heating mechanisms ($T_{\mathrm{vir}} > 10^4$K) (Bromm & Loeb, 2003; Lodato & Natarajan, 2006; Latif et al., 2015) where fragmentation is suppressed on smaller scales and the whole gas cloud collapses into a VMS. On the other hand, in the absence of efficient heating the gaseous

---

[5]Dynamical timescale is the measure of the time scale on which a star (or gas cloud) would expand or contract if the balance between pressure gradients and gravity was suddenly disrupted

material funneled to the galactic center can efficiently cool down (Rees & Ostriker, 1977) which eventually becomes unstable and fragments in a broad range of scales (Toomre, 1964). These could lead to the formation of the densest stellar clusters in the galactic center (Bate et al., 2003). Such dense stellar configurations have been observed (Balcells et al., 2007; Walcher et al., 2006; Côté et al., 2006) and they are known as the "Nuclear Stellar Clusters" (NSCs). NSCs are considered as the densest stellar configurations in the local Universe. In many galaxies nuclear star clusters and SMBHs are found to be co-existing (Seth et al., 2008; Graham & Spitler, 2009; Nguyen et al., 2019; Leigh et al., 2012; Georgiev et al., 2016). Therefore it makes sense to consider the possible joint formation of the nuclear star clusters and SMBHs. The key question here is how these dense stellar system could become unstable leading to the formation of the SMBHs.

A natural physical process for triggering instability in stellar clusters is stellar collisions which is an efficient mechanism for losing orbital energy support. In general physical collisions between stars are considered an exotic phenomena that rarely happen in the universe (Binney & Tremaine, 2008). However, it is well established that the cores dense stellar systems are unstable to suffer catastrophic runaway stellar collisions (Portegies Zwart & McMillan, 2002) which could lead to the formation of a supermassive star (SMS) in dense stellar clusters (Portegies Zwart & McMillan, 2002; Portegies Zwart et al., 2004; Freitag et al., 2007; Freitag, 2008; Glebbeek et al., 2009; Moeckel & Clarke, 2011; Lupi et al., 2014; Katz et al., 2015; Sakurai et al., 2017; Boekholt et al., 2018; Reinoso et al., 2018; Schleicher et al., 2019; Alister Seguel et al., 2020). In dense stellar clusters at high redshift, black hole seeds of masses $\sim 10^3 - 10^4 \, M_\odot$ could be formed due to enhanced accretion and collisions (Leigh et al., 2013b; Boekholt et al., 2018).

In the next chapter we show that considering the DCBH scenario, the mass function of SMBHs can be described as a broken power-law.

Bibliography

Abbott B. P., Abbott R., Abbott T. D., Abernathy M. R., Acernese F., Ackley K. e. a., LIGO Scientific Collaboration Virgo Collaboration 2016, Phys. Rev. Lett., 116, 061102

Abbott B. P., et al., 2019, ApJ, 882, L24

Abramowicz M. A., Czerny B., Lasota J. P., Szuszkiewicz E., 1988, ApJ, 332, 646

Agarwal B., Khochfar S., Johnson J. L., Neistein E., Dalla Vecchia C., Livio M., 2012, MNRAS, 425, 2854

Agarwal B., Cullen F., Khochfar S., Ceverino D., Klessen R. S., 2019, MNRAS, 488, 3268

Alexander T., Natarajan P., 2014, Science, 345, 1330

Alister Seguel P. J., Schleicher D. R. G., Boekholt T. C. N., Fellhauer M., Klessen R. S., 2020, MNRAS, 493, 2352

Bañados E., et al., 2018, Nature, 553, 473

Balcells M., Graham A. W., Peletier R. F., 2007, ApJ, 665, 1104

Baraffe I., Heger A., Woosley S. E., 2001a, ApJ, 550, 890

Baraffe I., Heger A., Woosley S. E., 2001b, ApJ, 550, 890

Bardeen J. M., Press W. H., Teukolsky S. A., 1972, ApJ, 178, 347

Bate M. R., Bonnell I. A., Bromm V., 2003, MNRAS, 339, 577

Becerra F., Marinacci F., Bromm V., Hernquist L. E., 2018, MNRAS, 480, 5029

Begelman M. C., Volonteri M., 2017, MNRAS, 464, 1102

Binney J., Tremaine S., 2008, Galactic Dynamics: Second Edition

Boekholt T. C. N., Schleicher D. R. G., Fellhauer M., Klessen R. S., Reinoso B., Stutz A. M., Haemmerlé L., 2018, MNRAS, 476, 366

Boera E., Murphy M. T., Becker G. D., Bolton J. S., 2014, MNRAS, 441, 1916

Bondi H., 1952, MNRAS, 112, 195

Bonnell I. A., Bate M. R., Clarke C. J., Pringle J. E., 2001, MNRAS, 323, 785

Bromm V., Loeb A., 2003, ApJ, 596, 34

Capelo P. R., Volonteri M., Dotti M., Bellovary J. M., Mayer L., Governato F., 2015, Monthly
   Notices of the Royal Astronomical Society, 447, 2123

Chandrasekhar S., 1960, Proceedings of the National Academy of Science, 46, 253

Chon S., Omukai K., 2020, MNRAS, 494, 2851

Chon S., Hosokawa T., Yoshida N., 2018, MNRAS, 475, 4104

Corbett Moran C., Grudić M. Y., Hopkins P. F., 2018, arXiv e-prints, p. arXiv:1803.06430

Côté P., et al., 2006, ApJS, 165, 57

Dijkstra M., Ferrara A., Mesinger A., 2014, MNRAS, 442, 2036

Dopcke G., Glover S. C. O., Clark P. C., Klessen R. S., 2011, ApJ, 729, L3

Eisenstein D. J., et al., 2005, APJ, 633, 560

Escala A., 2006, ApJ, 648, L13

Escala A., 2007, ApJ, 671, 1264

Fan X., et al., 2001, AJ, 122, 2833

Fan X., et al., 2006, AJ, 131, 1203

Ferrara A., Salvadori S., Yue B., Schleicher D., 2014, MNRAS, 443, 2410

Finkelstein S. L., et al., 2012, APJ, 758, 93

Frank J., King A., Raine D. J., 2002, Accretion Power in Astrophysics: Third Edition

Freitag M., 2008, in Beuther H., Linz H., Henning T., eds, Astronomical Society of the Pacific
   Conference Series Vol. 387, Massive Star Formation: Observations Confront Theory. p. 247
   (arXiv:0711.4057)

Freitag M., Guerkan M. A., Rasio F. A., 2007, in St. -Louis N., Moffat A. F. J., eds, Astronomical
   Society of the Pacific Conference Series Vol. 367, Massive Stars in Interactive Binaries. p. 707
   (arXiv:astro-ph/0410327)

Georgiev I. Y., Böker T., Leigh N., Lützgendorf N., Neumayer N., 2016, MNRAS, 457, 2122

Glebbeek E., Gaburov E., de Mink S. E., Pols O. R., Portegies Zwart S. F., 2009, A&A, 497,
   255

Graham A. W., Spitler L. R., 2009, MNRAS, 397, 2148

Gunn J. E., Peterson B. A., 1965, APJ, 142, 1633

Haiman Z., 2004, ApJ, 613, 36

Helgason K., Ricotti M., Kashlinsky A., Bromm V., 2016, MNRAS, 455, 282

Hirano S., Hosokawa T., Yoshida N., Kuiper R., 2017, Science, 357, 1375

Hopkins P. F., Quataert E., 2010, MNRAS, 407, 1529

Hoyle F., Lyttleton R. A., 1939, Proceedings of the Cambridge Philosophical Society, 35, 592

Hoyle F., Lyttleton R. A., 1940a, Proceedings of the Cambridge Philosophical Society, 36, 325

Hoyle F., Lyttleton R. A., 1940b, Proceedings of the Cambridge Philosophical Society, 36, 424

Iliev I. T., Mellema G., Shapiro P. R., Pen U.-L., Mao Y., Koda J., Ahn K., 2012, MNRAS, 423, 2222

Inayoshi K., Ostriker J. P., Haiman Z., Kuiper R., 2018a, MNRAS, 476, 1412

Inayoshi K., Li M., Haiman Z., 2018b, MNRAS, 479, 4017

Inayoshi K., Visbal E., Haiman Z., 2019, arXiv e-prints, p. arXiv:1911.05791

Katz H., Sijacki D., Haehnelt M. G., 2015, MNRAS, 451, 2352

Kerr R. P., 1963, Phys. Rev. Lett., 11, 237

Kormendy J., Ho L. C., 2013, ARA&A, 51, 511

Kormendy J., Richstone D., 1995, ARA&A, 33, 581

Kulkarni G., Worseck G., Hennawi J. F., 2019, MNRAS, 488, 1035

Latif M., Schleicher D., 2019, Formation of the First Black Holes, doi:10.1142/10652.

Latif M. A., Schleicher D. R. G., Schmidt W., Niemeyer J., 2013, MNRAS, 433, 1607

Latif M. A., Bovino S., Grassi T., Schleicher D. R. G., Spaans M., 2015, MNRAS, 446, 3163

Latif M. A., Omukai K., Habouzit M., Schleicher D. R. G., Volonteri M., 2016, ApJ, 823, 40

Latif M. A., Khochfar S., Whalen D., 2020, ApJ, 892, L4

Leigh N., Böker T., Knigge C., 2012, MNRAS, 424, 2130

Leigh N. W. C., Böker T., Maccarone T. J., Perets H. B., 2013a, MNRAS, 429, 2997

Leigh N. W. C., Böker T., Maccarone T. J., Perets H. B., 2013b, MNRAS, 429, 2997

Levshakov S. A., Kegel W. H., 1998, MNRAS, 301, 323

Lodato G., Natarajan P., 2006, MNRAS, 371, 1813

Loeb A., Barkana R., 2001, ARAA, 39, 19

Loeb A., Furlanetto S. R., 2013, The First Galaxies in the Universe

Loeb A., Rasio F. A., 1994, ApJ, 432, 52

Lupi A., Colpi M., Devecchi B., Galanti G., Volonteri M., 2014, MNRAS, 442, 3616

Maccarone T. J., Zurek D. R., 2012, MNRAS, 423, 2

Madau P., Haardt F., Dotti M., 2014, ApJ, 784, L38

Margalit B., Metzger B. D., 2017, ApJ, 850, L19

Marziani P., Sulentic J. W., 2012, New Astron. Rev., 56, 49

Matsuoka Y., et al., 2018, PASJ, 70, S35

Matsuoka Y., et al., 2019, ApJ, 883, 183

Mayer L., Kazantzidis S., Escala A., Callegari S., 2010, Nature, 466, 1082

McKinney J. C., Tchekhovskoy A., Sadowski A., Narayan R., 2014, MNRAS, 441, 3177

McQuinn M., 2012, MNRAS, 426, 1349

McQuinn M., Furlanetto S. R., Hernquist L., Zahn O., Zaldarriaga M., 2005, APJ, 630, 643

Milosavljević M., Couch S. M., Bromm V., 2009, ApJ, 696, L146

Mineshige S., Kawaguchi T., Takeuchi M., Hayashida K., 2000, PASJ, 52, 499

Miralda-Escudé J., Haehnelt M., Rees M. J., 2000, APJ, 530, 1

Misner C. W., Thorne K. S., Wheeler J. A., 1973, Gravitation

Moeckel N., Clarke C. J., 2011, MNRAS, 410, 2799

Mortlock D. J., et al., 2011, Nature, 474, 616

Naoz S., Yoshida N., Gnedin N. Y., 2013, ApJ, 763, 27

Nguyen D. D., et al., 2019, ApJ, 872, 104

Omukai K., Schneider R., Haiman Z., 2008, ApJ, 686, 801

Oppenheimer J. R., Volkoff G. M., 1939, Physical Review, 55, 374

Pacucci F., Loeb A., 2020, ApJ, 895, 95

Pacucci F., Volonteri M., Ferrara A., 2015, MNRAS, 452, 1922

Pacucci F., Natarajan P., Volonteri M., Cappelluti N., Urry C. M., 2017, ApJ, 850, L42

Paczynski B., Abramowicz M. A., 1982, ApJ, 253, 897

Planck Collaboration et al., 2016, AAP, 594, A13

Portegies Zwart S. F., McMillan S. L. W., 2002, ApJ, 576, 899

Portegies Zwart S. F., Baumgardt H., Hut P., Makino J., McMillan S. L. W., 2004, Nature, 428, 724

Prieto J., Escala A., 2016, MNRAS, 460, 4018

Prieto J., Escala A., Volonteri M., Dubois Y., 2017, ApJ, 836, 216

Rees M. J., Ostriker J. P., 1977, MNRAS, 179, 541

Regan J. A., Downes T. P., 2018, MNRAS, 478, 5037

Regan J. A., Visbal E., Wise J. H., Haiman Z., Johansson P. H., Bryan G. L., 2017, Nature Astronomy, 1, 0075

Regan J. A., Downes T. P., Volonteri M., Beckmann R., Lupi A., Trebitsch M., Dubois Y., 2019, MNRAS, 486, 3892

Regan J. A., Haiman Z., Wise J. H., O'Shea B. W., Norman M. L., 2020a, The Open Journal of Astrophysics, 3, E9

Regan J. A., Wise J. H., O'Shea B. W., Norman M. L., 2020b, MNRAS, 492, 3021

Reinoso B., Schleicher D. R. G., Fellhauer M., Klessen R. S., Boekholt T. C. N., 2018, A&A, 614, A14

Rindler W., 1956, MNRAS, 116, 662

Sadowski A., 2011, arXiv e-prints, p. arXiv:1108.0396

Sakurai Y., Yoshida N., Fujii M. S., Hirano S., 2017, MNRAS, 472, 1677

Schleicher D. R. G., Palla F., Ferrara A., Galli D., Latif M., 2013, A&A, 558, A59

Schleicher D. R. G., et al., 2019, Boletin de la Asociacion Argentina de Astronomia La Plata Argentina, 61, 234

Schödel R., et al., 2002, Nature, 419, 694

Schwarzschild K., 1916, Sitzungsberichte der Königlich Preußischen Akademie der Wissenschaften (Berlin, pp 189–196

Schwarzschild K., 1999, arXiv e-prints, p. physics/9905030

Seth A., Agüeros M., Lee D., Basu-Zych A., 2008, ApJ, 678, 116

Shen Y., et al., 2019, ApJ, 873, 35

Shlosman I., Choi J.-H., Begelman M. C., Nagamine K., 2016, MNRAS, 456, 500

Shu F. H., 1977, ApJ, 214, 488

Shull J. M., Venkatesan A., 2008, APJ, 685, 1

Sądowski A., 2009, ApJS, 183, 171

Smith A., Bromm V., 2019, Contemporary Physics, 60, 111

Sugimura K., Hosokawa T., Yajima H., Inayoshi K., Omukai K., 2018, MNRAS, 478, 3961

Takeo E., Inayoshi K., Mineshige S., 2020, arXiv e-prints, p. arXiv:2002.07187

Taniguchi Y., Shioya Y., Ajiki M., Fujita S. S., Nagao T., Murayama T., 2003, Journal of Korean Astronomical Society, 36, 123

Teo E., 2003, General Relativity and Gravitation, 35, 1909

Thorne K. S., 1974, ApJ, 191, 507

Tolman R. C., 1934, Proceedings of the National Academy of Science, 20, 169

Toomre A., 1964, ApJ, 139, 1217

Totani T., et al., 2014, PASJ, 66, 63

Toubiana A., Marsat S., Babak S., Barausse E., Baker J., 2020, Phys. Rev. D, 101, 104038

Umeda H., Hosokawa T., Omukai K., Yoshida N., 2016, ApJ, 830, L34

Visbal E., Haiman Z., Bryan G. L., 2014, MNRAS, 445, 1056

Volonteri M., 2010, The Astronomy and Astrophysics Review, 18, 279

Volonteri M., Rees M. J., 2005, ApJ, 633, 624

Volonteri M., Silk J., Dubus G., 2015, ApJ, 804, 148

Volonteri M., Bogdanović T., Dotti M., Colpi M., 2016, IAU Focus Meeting, 29B, 285

Walcher C. J., Böker T., Charlot S., Ho L. C., Rix H. W., Rossa J., Shields J. C., van der Marel R. P., 2006, ApJ, 649, 692

Wang R., et al., 2019, ApJ, 887, 40

Willott C. J., et al., 2010, AJ, 139, 906

Wise J. H., Regan J. A., O'Shea B. W., Norman M. L., Downes T. P., Xu H., 2019, Nature, 566, 85

Wu X.-B., et al., 2015, Nature, 518, 512

Yue B., Ferrara A., Salvaterra R., Xu Y., Chen X., 2014, MNRAS, 440, 1263

Zeldovich Y. B., Novikov I. D., 1971, Relativistic astrophysics. Vol.1: Stars and relativity

Chapter 2

THE MASS FUNCTION OF SUPERMASSIVE BLACK HOLES IN THE DIRECT COLLAPSE SCENARIO

2.1 Introduction

A key challenge to the theory of the formation of supermassive black holes (SMBH) in the early universe is the observation of very massive ($M \approx 10^9 \, \mathrm{M_\odot}$) and luminous ($L \gtrsim 10^{13} \, \mathrm{L_\odot}$) quasars already in place by $z \sim 7$, when the universe is just ~ 800 Myr old (e.g., Fan et al., 2006; Mortlock et al., 2011; Wu et al., 2015; Bañados et al., 2018, ; see also the review by Woods et al. (2018)). Objects that accumulate at least a billion $\mathrm{M_\odot}$ in less than a billion years after the Big Bang put a strain on the normal ideas of Eddington-limited growth of black hole seeds that originate from Population III stellar remnants. Starting from a seed mass M_0, Eddington-limited growth leads to a mass $M(t) = M_0 \exp[\epsilon^{-1}(1 - \epsilon)t/t_E]$, where $t_E \approx 450$ Myr and $\epsilon \, (\approx 0.1)$ is a radiative efficiency factor. Population III stars are thought to have masses $\lesssim 40 \, \mathrm{M_\odot}$ (Hosokawa et al., 2011), and their remnants would be less massive, so that there is apparently not enough time available to reach $M \sim 10^9 \, \mathrm{M_\odot}$. These constraints show that a combination of both more massive initial seeds and a super-Eddington growth rate may be necessary to account for the observed SMBH at $z \sim 7$.

One promising pathway is that of direct collapse black holes (DCBH) (Bromm & Loeb, 2003). The idea is that Lyman-Werner (LW) photons (having energies 11.2 to 13.6 eV) from the first Population III stars can propagate far from their sources and dissociate H_2 in other primordial gas clouds. Without H_2 cooling these gas clouds equilibrate to temperatures $T \sim 8000$ K set by atomic cooling, which means that the Jeans mass is $\sim 10^5 \, \mathrm{M_\odot}$ at a number density $n = 10^4 \, \mathrm{cm^{-3}}$, as opposed to $\sim 10^3 \, \mathrm{M_\odot}$ in a normal Population III star formation environment or $\sim 1 \, \mathrm{M_\odot}$ in present day star formation. Due to their large mass these collapsing cloud fragments may be able to collapse directly into black holes, after a brief period as a supermassive star (Bromm & Loeb, 2003) or quasi-star (Begelman et al., 2006, 2008), if the infalling matter can overcome the angular momentum barrier and disruptive effects of radiative feedback. An interesting joint solution to these barriers is proposed by Sakurai et al. (2016) based on the episodic accretion scenario of Vorobyov et al. (2013) that is powered by

gravitational instability in a circumstellar disk. In this model the episodic accretion results in a lower surface temperature of a supermassive star, thereby also reducing the effect of radiative feedback that can limit mass accumulation in the case of normal Population III star formation (Hosokawa et al., 2011). The DCBH model has been extensively developed in the context of galaxy formation models, resulting in a scenario where the formation of atomic cooling halos is seeded by the first stars, and the subsequent DCBH produce LW radiation that triggers the formation of other atomic cooling halos and DCBH in a kind of chain reaction process (Yue et al., 2014). A rapid period of growth of atomic cooling halos and therefore DCBH formation ensues, with the growth rate at any time related to the instantaneous number of DCBH. The rapidly growing phase of DCBH creation is also a period of possible rapid mass growth through super-Eddington accretion (Inayoshi & Haiman, 2016; Pacucci et al., 2017). The whole process comes to a rapid halt however, when the gas in the atomic cooling halos is photoevaporated by the ambient radiation field. According to Yue et al. (2014) the DCBH era lasts from $z \approx 20$ to $z \approx 13$, or a time period $T \approx 150$ Myr, after which DCBH formation is completely suppressed. Here we adopt the picture emerging from their semi-analytic model, however we note that numerical simulations (e.g., Agarwal et al., 2012; Chon et al., 2016; Habouzit et al., 2016) have not reached a consensus on the DCBH formation rate or the termination time of their formation.

In this Letter, we seek a simple model of the growth of DCBH in the early universe that captures just the essential features of the scenario described above, in order to reach an analytic understanding of the mass and luminosity functions of observable quasars that form through the DCBH scenario.

2.2 Background

Yue et al. (2014) estimate that the rapid formation of DCBH occurs between $z \approx 20$ and $z \approx 13$, after which it ends abruptly. The semi-analytic model of Dijkstra et al. (2014) is broadly consistent with this and shows that the number density of DCBH n_{DCBH} grows rapidly during a similar interval.

Figure 2.1 shows the results of Dijkstra et al. (2014) plotted against time after the Big Bang, for two possible values of the critical flux of LW photons J_{crit} (written in units of 10^{-21} erg s^{-1} cm^{-2} Hz^{-1} sr^{-1}) that is needed to create the atomic cooling halos that are DCBH progenitors. The calculation of J_{crit} (e.g., Shang et al., 2010) includes the additional effect of near-infrared radiation with energy above 0.76 eV that can also inhibit the formation of H_2 by dissociating the H^- ion that is an intermediary in the H_2 formation chain. Although significant uncertainties exist in the actual number of DCBH created, due to uncertainties in the value of J_{crit} that depends on the source density and spectra, escape fraction from the host halos, etc., the slope of growth, $\lambda(t) \equiv d \log n_{\text{DCBH}}/dt$, is similar in all their modeled cases. For the two cases shown here, we find an average value λ measured between data points from $z = 20$ to $z = 12$, which corresponds roughly to the period of rapid DCBH formation. For their canonical model $J_{\text{crit}} = 300$ the best fit line yields $\lambda = 27.7$ Gyr^{-1}, and for $J_{\text{crit}} = 100$ the best fit is $\lambda = 17.7$ Gyr^{-1}. Here we use the canonical model and adopt $\lambda = 28.0$ Gyr^{-1}, slightly steeper than the best fit. This in the interest of rounding off and also because there is evidence that the DCBH growth era ended just prior to this data point, at $z \approx 13$ (Yue et al., 2014), which would tend to drive the slope to a slightly greater value.
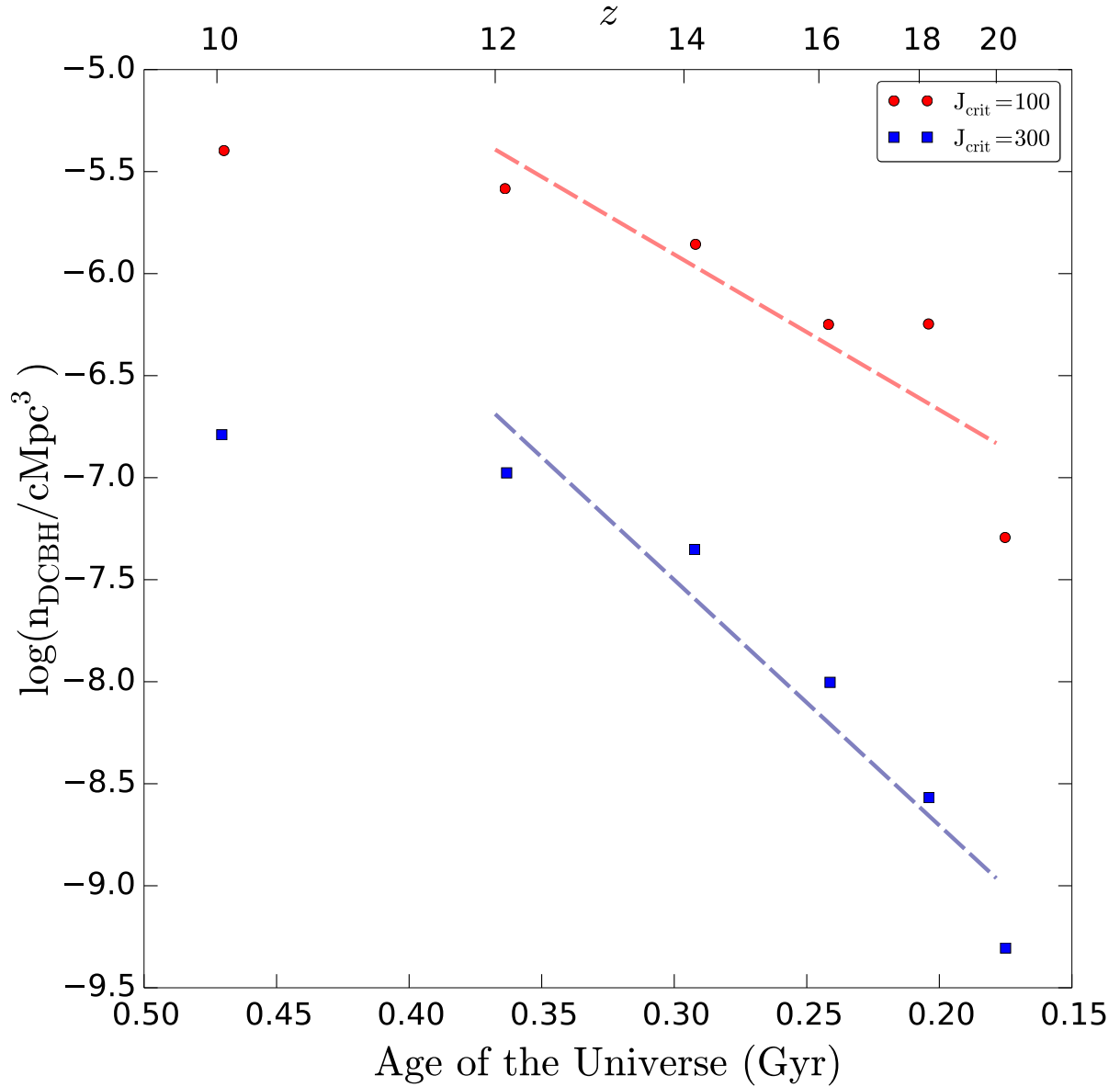
Figure 2.1: The growth of the number density of DCBH n_{DCBH}. The data points correspond to n_{DCBH} (in cMpc^{-3}) at redshift values $z = 20.3, 18.2, 16.2, 14.1, 12.1, 10.0$ corresponding to cosmic times $0.18, 0.20, 0.24, 0.29, 0.36, 0.47$ Gyr after the Big Bang, and are taken from Dijkstra et al. (2014).

Each DCBH can be modeled as growing in mass at an exponential rate, but the starting times of the accretion process will be spread throughout the DCBH formation era. However, the super-Eddington growth will cease for all DCBH at about the same time, so that there will be a distribution of accretion times among the population of DCBH. This is a key part of our model as developed in Section 2.3.

The growth of an individual DCBH is thought to proceed by default at an Eddington-limited rate, but periods of super-Eddington growth are also possible (Pacucci et al., 2017). The

Eddington luminosity is

$$L_{\mathrm{E}} = \frac{4\pi c G m_{\mathrm{p}} M}{\sigma_T}. \tag{2.1}$$

where M is the black hole mass, m_{p} is the proton mass, and $\sigma_T = (8\pi/3)(e^2/m_{\mathrm{e}}c^2)^2$ is the Thomson cross section in which m_{e} is the electron mass. At this luminosity the radiation pressure can balance the gravitational pressure. The accretion of mass to very small radii comparable to the Schwarzschild radius will release a significant portion of the rest mass energy, hence the luminosity is normally estimated as $L_{\mathrm{acc}} = \epsilon \dot{M}_{\mathrm{acc}} c^2$, where $\dot{M}_{\mathrm{acc}}$ is the mass accretion rate and ϵ is the radiative efficiency, typically set to 0.1. Since the accretor will gain rest mass at the rate $\dot{M} = (1 - \epsilon)\dot{M}_{\mathrm{acc}}$, we equate L_{acc} with L_{E} to find that

$$\frac{dM}{dt} = \gamma_0 M \Rightarrow M(t) = M_0 \exp(\gamma_0 t), \tag{2.2}$$

where $\gamma_0 = (1 - \epsilon)/(\epsilon t_{\mathrm{E}})$ and $t_{\mathrm{E}} = 2e^4/(3Gm_{\mathrm{p}}m_{\mathrm{e}}^2 c^3) = 450$ Myr is the Eddington time. Here we follow Pacucci et al. (2017) in accounting for the idea that accretion (especially of the super-Eddington variety) may be episodic, by identifying the duty cycle $\mathcal{D}$ as the fraction of time spent accreting, and the Eddington ratio f_{Edd} that is = 1 for Eddington-limited accretion but can be < 1 for sub-Eddington accretion and > 1 for super-Eddington accretion. We use a generalized accretion rate $\gamma = \chi \gamma_0$ where $\chi = \mathcal{D} f_{\mathrm{Edd}}$ is a correction factor to account for the fact that the accretion rate could be super-Eddington for some periods of time. The quantitatively relevant parameter is $\chi = \mathcal{D} f_{\mathrm{Edd}}$. Pacucci et al. (2017) find that objects with $M \gtrsim 10^5 \, \mathrm{M}_\odot$ can have high efficiency accretion, $0.5 \leq \mathcal{D} \leq 1$ and $1 \leq f_{\mathrm{Edd}} \leq 100$, but objects with $M \lesssim 10^5 M_\odot$ have low efficiency accretion, $0 \leq \mathcal{D} \leq 0.5$ and $0 \leq f_{\mathrm{Edd}} \leq 1$. The simplest assumption is that $\chi = 1$ for Eddington-limited growth, but our model allows for the putative super-Eddington growth in the DCBH formation era.

2.3   Mass Function

We assume that the distribution of initial black hole masses is lognormal, i.e., the differential number density per logarithmic mass bin is distributed normally:

$$\frac{dn}{d \ln M_0} = \frac{1}{\sqrt{2\pi}\sigma_0} \exp\left(-\frac{(\ln M_0 - \mu_0)^2}{2\sigma_0^2}\right). \tag{2.3}$$

Here μ_0 and σ_0 are the mean and standard deviation of the distribution of $\ln M_0$, respectively. A lognormal distribution for the birth mass function of DCBH seeds is consistent with the results of Ferrara et al. (2014) for intermediate masses ($4.75 < \log(M/\mathrm{M}_\odot) < 6.25$), and we fit those results with $\mu_0 = 11.7$ (corresponding to a peak at $\log M/\mathrm{M}_\odot = 5.1$) and $\sigma_0 = 1.0$.

Since the growth law implies that

$$\ln M(t) = \ln M_0 + \gamma t, \tag{2.4}$$

we can write the mass function at a later time as

$$\frac{dn}{d \ln M} = \frac{1}{\sqrt{2\pi}\sigma_0} \exp\left(-\frac{(\ln M - \mu_0 - \gamma t)^2}{2\sigma_0^2}\right). \tag{2.5}$$

The accretion time t may not be a fixed constant that applies to all objects, therefore we can integrate over a function $f(t)$ (which has units of inverse time) that describes the distribution of accretion times. In this case the final observed mass function $f(\ln M) \equiv dn/d \ln M$ is

$$\int_0^T \frac{1}{\sqrt{2\pi}\sigma_0} \exp\left(-\frac{(\ln M - \mu_0 - \gamma t')^2}{2\sigma_0^2}\right) f(t') \, dt'. \tag{2.6}$$

Here $f(t')$ is a normalized distribution of accretion times t' and T is the maximum possible accretion time. The function $f(t')$ is determined by considering the creation rate of black holes in the DCBH scenario. The number density n of black holes grows in a type of chain reaction (Yue et al., 2014; Dijkstra et al., 2014) with the instantaneous creation rate $dn/dt = \lambda(t)\, n$. The simplest case where $\lambda(t) = \lambda$ has a constant value leads to pure exponential growth. If this growth continues from a time $t = 0$ when the first DCBH is created until a time T when the creation of all DCBH is terminated, then each black hole that was created at time t has an accretion lifetime $t' = T - t$ in the range $[0, T]$. The normalized distribution of accretion lifetimes t' is then

$$f(t') = \frac{\lambda \exp(-\lambda t')}{[1 - \exp(-\lambda T)]}. \tag{2.7}$$

Using the indefinite integral identity

$$\int \exp[-(ax^2 + bx + c)]dx$$
$$= \frac{1}{2}\sqrt{\frac{\pi}{a}} \exp\left(\frac{b^2 - 4ac}{4a}\right) \mathrm{erf}\left(\sqrt{a}\left[x + \frac{b}{2a}\right]\right), \tag{2.8}$$

valid for $a > 0$, we evaluate the integral in Equation (2.6) using Equation (2.7) and obtain a full expression

$$\begin{aligned}
f(\ln M) &= \frac{\alpha \exp\left(\alpha\mu_0 + \alpha^2\sigma_0^2/2\right)}{2[1 - \exp\left(-\alpha\beta\right)]} M^{-\alpha} \\
&\times \left[\mathrm{erf}\left(\frac{1}{\sqrt{2}}\left(\alpha\sigma_0 - \frac{\ln M - \mu_0 - \beta}{\sigma_0}\right)\right)\right. \\
&- \left.\mathrm{erf}\left(\frac{1}{\sqrt{2}}\left(\alpha\sigma_0 - \frac{\ln M - \mu_0}{\sigma_0}\right)\right)\right].
\end{aligned} \tag{2.9}$$

Here $\alpha \equiv \lambda/\gamma$, the dimensionless ratio of the growth rate of DCBH formation to the growth rate of the mass of individual DCBH, and $\beta \equiv \gamma T$, the dimensionless number of DCBH growth times within the DCBH formation era.

In the limit $T \to \infty$, the function becomes

$$\begin{aligned}
f(\ln M) &= \frac{\alpha}{2} \exp\left(\alpha\mu_0 + \alpha^2\sigma_0^2/2\right) M^{-\alpha} \\
&\times \mathrm{erfc}\left(\frac{1}{\sqrt{2}}\left(\alpha\sigma_0 - \frac{\ln M - \mu_0}{\sigma_0}\right)\right),
\end{aligned} \tag{2.10}$$

which is the modified lognormal power law (MLP) function (Basu et al., 2015). Equation (2.9) represents a tapered version of the MLP, with the break in the power-law occurring at

$\log M \approx (\mu_0 + \beta)/2.3$, meaning that the peak of the original lognormal is shifted in $\ln M$ by an amount $\beta = \gamma T$. Henceforth, we refer to Equation (2.9) as the tapered power law (TPL) function.

Figure 2.2 shows the TPL function using parameter values obtained from models of the DCBH growth era. We pick $\mu_0 = 11.7$ and $\sigma_0 = 1.0$ based on the model of Ferrara et al. (2014). From Dijkstra et al. (2014) (see Figure 2.1) we adopt $\lambda = 28.0$ Gyr^{-1} for the era of rapid DCBH formation using their canonical model. The length of the DCBH growth era is $T = 0.15$ Gyr (Yue et al., 2014). For accretion growth during this period we expect that super-Eddington growth can occur (Dijkstra et al., 2014) but with a wide range of possible values. We pick a series of values $\chi = [1, 2, 3]$ covering Eddington-limited growth and two values of super-Eddington growth. Since $\gamma = \chi \gamma_0 = 20\chi$ Gyr^{-1}, this leads to $\alpha = [1.4, 0.7, 0.47]$ and $\beta = [3, 6, 9]$ for our adopted values of λ and T. Figure 2.2 shows that the super-Eddington growth models allow for the development of a mass function that has both a visually evident power-law profile as well as a notable break in the power law at high mass. This break is a marker of the end of the DCBH growth era, since both the creation of new DCBH as well as their super-Eddington growth ceases after the time interval T.

2.4   The Quasar Luminosity Function

Once the DCBH growth era has ended at $z \approx 13$, the population of DCBH may continue to undergo Eddington-limited accretion, and the luminosity function can be estimated using Equation (2.1). Over time, the mass function $f(\ln M)$ will retain its shape but move to the right since $\ln M$ at the end of the DCBH era will shift by an amount $\gamma \Delta t_z$ where Δt_z is the time interval between the end of the DCBH era ($z \approx 13$) and an observable redshift z. However, the duty cycle $\mathcal{D}$ and therefore $\chi = \mathcal{D} f_{\mathrm{Edd}}$ may be $\ll 1$ in this era, rendering mass growth to small fractional levels. A random sampling of $\mathcal{D}$ and f_{Edd} for individual object growth after $z \approx 13$ shows that the overall distribution maintains its shape and moves to the right in $\log M$. We also note that the mass growth of SMBH may be quenched above $\sim 10^{10}$ M$_\odot$ (Inayoshi & Haiman, 2016; Ichikawa & Inayoshi, 2017), in agreement with results of current quasar surveys (Ghisellini et al., 2010; Trakhtenbrot, 2014).

Assuming that observed quasars are undergoing Eddington-limited accretion, we use Equation (2.1) to transform the mass function into a luminosity function. We expect that the mass of the quasars are not growing substantially during this time, for reasons discussed above, and we are really most interested in fitting the shape of the function, which should remain much the same for a variety of redshifts in the post-DCBH-growth era. Figure 2.3 shows the inferred quasar luminosity function (QLF) $\phi(L) \propto dn/d \log L$ for a suitable pair of values for α and β, overlaid on $z = 3$ quasar bolometric luminosities compiled by Hopkins et al. (2007). Here we are only interested in fitting the shape of the luminosity function and not the absolute number of sources. The normalization can be scaled to fit the observed number at any redshift.

We hold (μ_0, σ_0) fixed at their model-inspired values $(11.7, 1.0)$ since they are most important in determining the unobserved low end of the luminosity function. We effectively fit observations with two parameters (α, β). This is in contrast to the usual practice of fitting the observed QLF with a double power law (e.g., Hopkins et al., 2007; Masters et al., 2012; Schindler et al., 2019) that requires three parameters: the two power-law indices and a joining

point.

In our model, the values of α, β that fit the QLF are not merely mathematical parameters. Instead, they reveal the history of the putative DCBH growth era. For the adopted DCBH number growth rate $\lambda = 28.0$ Gyr^{-1} and a duration $T = 0.15$ Gyr, and individual masses growing at a rate $\gamma = \chi \gamma_0$, the two fitted parameters are related to the super-Eddington factor χ by

$$\alpha = 1.4\chi^{-1}, \tag{2.11}$$
$$\beta = 3\chi. \tag{2.12}$$

We find an excellent match to the QLF with $[\alpha, \beta] = [0.5, 8.4]$. Both the values of α and β imply a super-Eddington factor $\chi = 2.8$, revealing the self-consistency of our model. In principle the QLF could have been fit with any α and β that could individually imply very different values of χ. In that case our underlying model would be inconsistent, or at least need to explore values of λ and T that were quite different than those implied by current models of the DCBH growth era.

To elaborate on the above point, our model could in principle also be applied to SMBH formation from alternate scenarios such as Population III remnants (Madau & Rees, 2001; Whalen & Fryer, 2012) or mergers of primordial Population III stars (Boekholt et al., 2018; Reinoso et al., 2018). It could apply as long as the black hole production could be described as growing exponentially at some rate λ and for a finite time T, during which the individual masses grew at an Eddington-limited or super-Eddington rate.

2.5   Summary

We have presented an analytic model that captures some essential features of the DCBH growth scenario and uses them to derive an analytic mass function and by implication a luminosity function. A double power-law function has been commonly used in the literature to mathematically fit the quasar luminosity function (QLF). Here, we instead use a physically-motivated formula based on the scenario of the DCBH growth era that has been developed by many researchers. It is not a double-power law at high mass and luminosity, but rather a tapered power-law. We believe that the rapid fall off in the QLF at high luminosity is better modeled as a tapered part of a power law rather than as a second power law. The break point of the power law identifies the end of the era of DCBH creation.

We have fit an observed QLF with a power-law index $\alpha = 0.5$ and the break-point related parameter $\beta = 8.4$. These are consistent with a period of rapid mass growth of DCBH with super-Eddington factor $\chi = 2.8$, for a time period $T = 150$ Myr during which the growth rate of the number density n_{DCBH} was $\lambda = 28.0$ Gyr^{-1}. In principle, the best fit values to QLF data can be used to constrain such theoretical models of DCBH growth.

Our model has two key components. Initially high mass $\sim 10^5$ M$_\odot$ seeds grow rapidly in number during a limited time period in the early universe, since DCBH formation leads to the emission of LW photons that seed the formation of other DCBH. These objects also live within gas-rich halos and undergo super-Eddington mass accretion. Then at some time both the formation of DCBH as well as the super-Eddington accretion of the existing DCBH

comes to a rapid halt due to the photoevaporation of the host halos. What remains is a tapered power-law (TPL) distribution of masses and therefore also of luminosity if the observed quasars are undergoing subsequent Eddington-limited accretion. Future modeling can relax some of these assumptions, for example the formation of DCBH may continue long enough to outlive the period of rapid (super-Eddington) mass growth, especially if driven by mechanisms other than the LW flux (Wise et al., 2019), and the super-Eddington accretion may not apply to all objects (Pacucci et al., 2017; Latif et al., 2018).

Acknowledgements

Connection to next chapter

In the next chapter we discuss how SMBH seeds of masses 10^{3-4} $M_\odot$ can be created via runaway collisions and gas accretion inside dense nuclear star clusters. That is an alternate formation scenario to the DCBH scenario studied here.
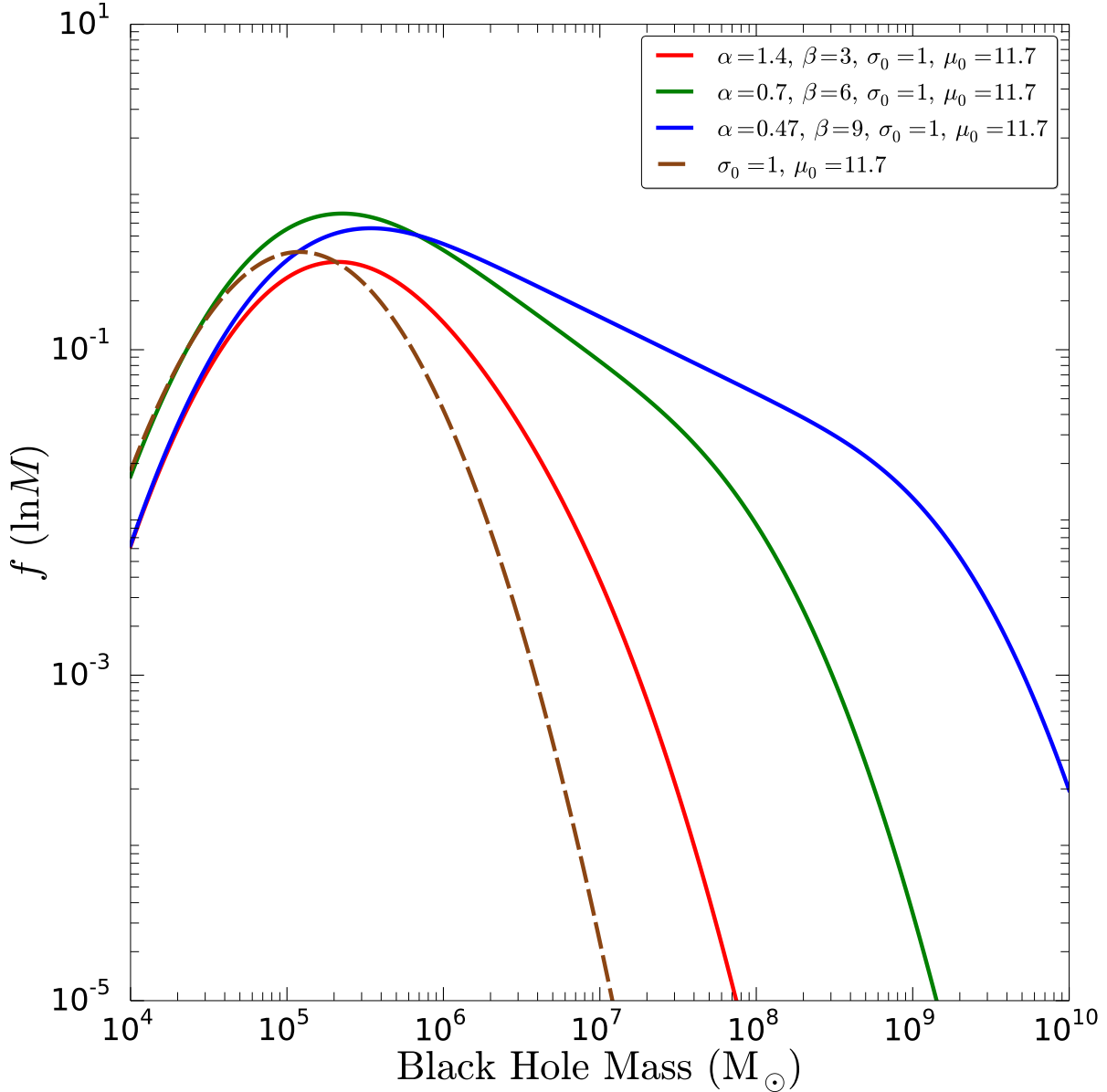
Figure 2.2: The tapered power law (TPL) distribution and an underlying lognormal distribution. Parameters are chosen as plausible values based on models of the DCBH growth era and also illustrate important features of the distribution. Shown is an underlying lognormal distribution (dashed line) with $\mu_0 = 11.7, \sigma_0 = 1$, and the TPL distributions generated from it assuming either of the following: Eddington-limited growth with $\chi = 1$ (red line), super-Eddington growth with $\chi = 2$ (green line), and super-Eddington growth with $\chi = 3$ (blue line). Note that $\mu_0 = 11.7$ corresponds to a peak mass $10^{5.1}$ M$_\odot$.
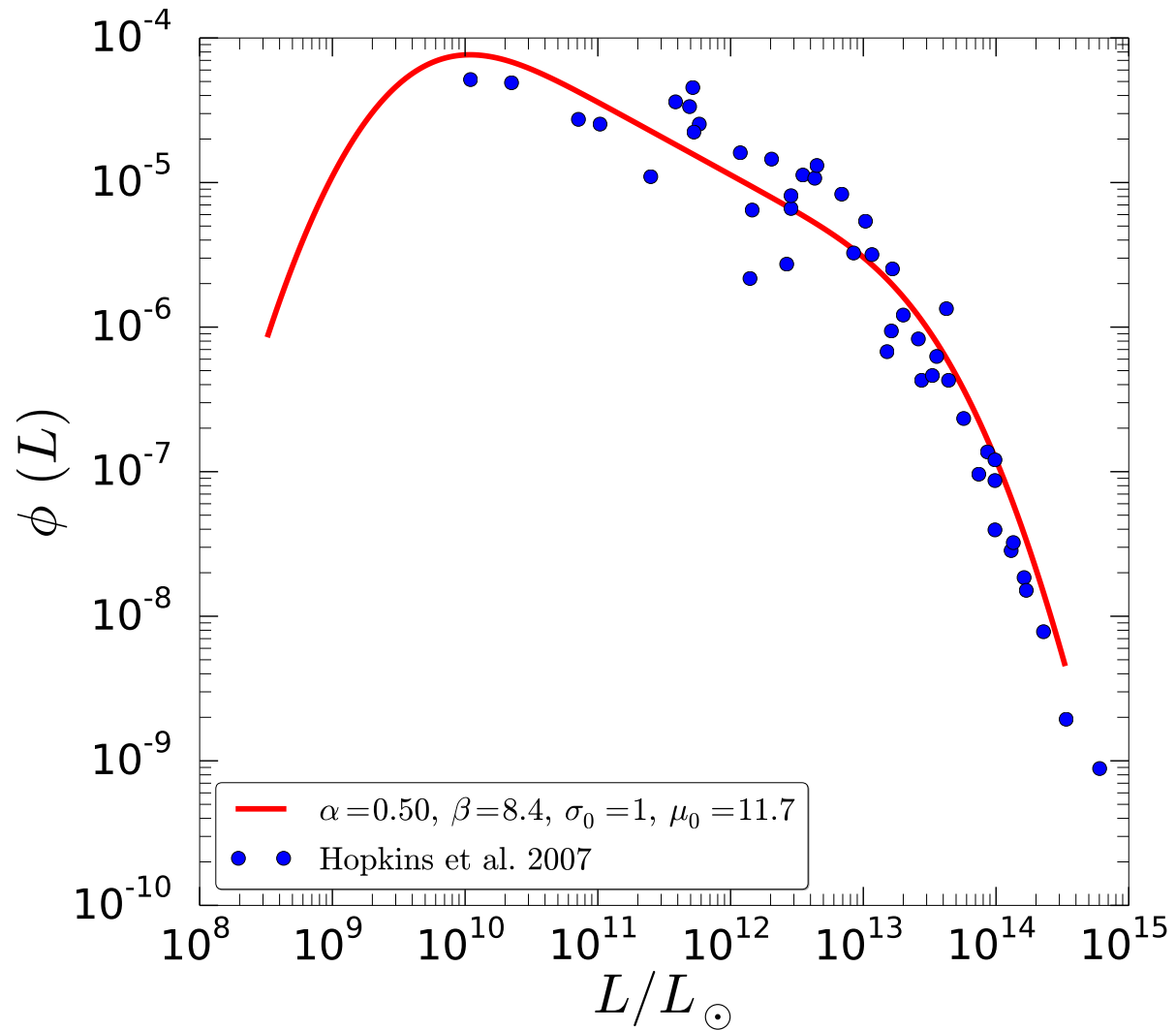
Figure 2.3: Probability distribution of quasar luminosities. The TPL function is plotted with parameters $\alpha = 0.5$ and $\beta = 8.4$ in which μ_0 and σ_0 are held fixed at 11.7 and 1.0, respectively. Data points are estimates of bolometric luminosities of quasars at $z = 3$ taken from Hopkins et al. (2007).

Bibliography

Agarwal B., Khochfar S., Johnson J. L., Neistein E., Dalla Vecchia C., Livio M., 2012, MNRAS, 425, 2854

Bañados E., et al., 2018, Nature, 553, 473

Basu S., Gil M., Auddy S., 2015, MNRAS, 449, 2413

Begelman M. C., Volonteri M., Rees M. J., 2006, MNRAS, 370, 289

Begelman M. C., Rossi E. M., Armitage P. J., 2008, MNRAS, 387, 1649

Boekholt T. C. N., Schleicher D. R. G., Fellhauer M., Klessen R. S., Reinoso B., Stutz A. M., Haemmerlé L., 2018, MNRAS, 476, 366

Bromm V., Loeb A., 2003, ApJ, 596, 34

Chon S., Hirano S., Hosokawa T., Yoshida N., 2016, ApJ, 832, 134

Dijkstra M., Ferrara A., Mesinger A., 2014, MNRAS, 442, 2036

Fan X., et al., 2006, AJ, 131, 1203

Ferrara A., Salvadori S., Yue B., Schleicher D., 2014, MNRAS, 443, 2410

Ghisellini G., et al., 2010, MNRAS, 405, 387

Habouzit M., Volonteri M., Latif M., Dubois Y., Peirani S., 2016, MNRAS, 463, 529

Hopkins P. F., Richards G. T., Hernquist L., 2007, ApJ, 654, 731

Hosokawa T., Omukai K., Yoshida N., Yorke H. W., 2011, Science, 334, 1250

Ichikawa K., Inayoshi K., 2017, ApJ, 840, L9

Inayoshi K., Haiman Z., 2016, ApJ, 828, 110

Latif M. A., Volonteri M., Wise J. H., 2018, MNRAS, 476, 5016

Madau P., Rees M. J., 2001, ApJ, 551, L27

Masters D., et al., 2012, ApJ, 755, 169

Mortlock D. J., et al., 2011, Nature, 474, 616

Pacucci F., Natarajan P., Volonteri M., Cappelluti N., Urry C. M., 2017, ApJ, 850, L42

Reinoso B., Schleicher D. R. G., Fellhauer M., Klessen R. S., Boekholt T. C. N., 2018, A&A, 614, A14

Sakurai Y., Vorobyov E. I., Hosokawa T., Yoshida N., Omukai K., Yorke H. W., 2016, MNRAS, 459, 1137

Schindler J.-T., et al., 2019, ApJ, 871, 258

Shang C., Bryan G. L., Haiman Z., 2010, MNRAS, 402, 1249

Trakhtenbrot B., 2014, ApJ, 789, L9

Vorobyov E. I., DeSouza A. L., Basu S., 2013, ApJ, 768, 131

Whalen D. J., Fryer C. L., 2012, ApJ, 756, L19

Wise J. H., Regan J. A., O'Shea B. W., Norman M. L., Downes T. P., Xu H., 2019, Nature, 566, 85

Woods T. E., et al., 2018, arXiv e-prints, p. arXiv:1810.12310

Wu X.-B., et al., 2015, Nature, 518, 512

Yue B., Ferrara A., Salvaterra R., Xu Y., Chen X., 2014, MNRAS, 440, 1263

Chapter 3

Formation of supermassive black hole seeds in nuclear star clusters via gas accretion and runaway collisions

3.1 Introduction

The observation of more than two hundred SMBHs with masses $\gtrsim 10^9\,M_\odot$ at redshift $z \gtrsim 6$ (Fan et al., 2001; Willott et al., 2010; Mortlock et al., 2011; Wu et al., 2015; Bañados et al., 2018; Matsuoka et al., 2018; Wang et al., 2019; Shen et al., 2019; Matsuoka et al., 2019; Onoue et al., 2019; Vito et al., 2019) has challenged our general understanding of black hole growth and formation. How these massive objects formed and grew over cosmic time is currently one of the biggest puzzles in astrophysics (Volonteri, 2010, 2012; Latif & Ferrara, 2016; Gallerani et al., 2017; Smith & Bromm, 2019; Inayoshi et al., 2019; Latif & Schleicher, 2019). Our current understanding is that the initial populations of black holes seeds were formed at $z \sim 20 - 30$ (Barkana & Loeb, 2001), and then they rapidly grow to their final masses by gas accretion and mergers (Dayal et al., 2019; Pacucci & Loeb, 2020; Piana et al., 2021). In depth reviews about the formation and growth of SMBHs in the early universe can be found in Inayoshi et al. (2019); Latif & Schleicher (2019); Haemmerlé et al. (2020).

The discovery of billion solar mass black holes at a time when the Universe was less than 1 Gyr old has created the so called "seeding" problem. In the standard Eddington limited accretion scenario a black hole of mass $M_\bullet$ grows exponentially over time,

$$M_\bullet(t) = M_{\bullet,0} \exp\left(\frac{1 - \epsilon}{\epsilon} \frac{t}{t_S}\right), \tag{3.1}$$

where $M_{\bullet,0}$ is the initial mass of the black hole or the 'seed' mass, ϵ is the radiation efficiency with standard value 0.1 (Shapiro, 2005) and t_S is the Salpeter time-scale, $t_S = 450$ Myr. In the standard light seeding models the SMBH starts growing from a Pop III stellar remnant of mass $M_\bullet \lesssim 100\,M_\odot$ (Madau & Rees, 2001; Abel et al., 2002; Volonteri & Rees, 2006; Yoshida et al., 2008; Hirano et al., 2014; Stacy et al., 2016). To reach a mass of $\gtrsim 10^9\,M_\odot$ at $z \gtrsim 6$ from a $100\,M_\odot$ Pop III star, the growth process requires continuous Eddington accretion (or nearly continuous Bondi accretion (e.g. Leigh et al., 2013a)). However this is extremely

difficult to achieve as the radiative and kinetic feedback from the stellar winds slow down the accretion of the gas (Tanaka & Haiman, 2009; Regan et al., 2019). One possible solution to this problem could be galaxy mergers (Capelo et al., 2015; Volonteri et al., 2016; Pacucci & Loeb, 2020), which could lead to the mergers of massive BHs. However, during mergers the large recoil induced by gravitational wave emission can unbind the merger remnants from the shallow potential wells of their host galaxies (Haiman, 2004).

An alternate solution relies on super-Eddington accretion (Volonteri & Rees, 2005; Alexander & Natarajan, 2014; Madau et al., 2014; Volonteri et al., 2015; Pacucci et al., 2015, 2017; Begelman & Volonteri, 2017; Toyouchi et al., 2019; Takeo et al., 2020). Unlike the previous scenario, a temporary non-availability of gas is less of a problem in this scenario, as it can be compensated via highly efficient accretion at other times. However, ensuring a sufficiently high streaming efficiency of the gas from the large-scale reservoir down to horizon scales is difficult to achieve because accretion flows onto seed BHs might be reduced by their own radiation (Milosavljević et al., 2009; Sugimura et al., 2018; Regan et al., 2019) and due to the inefficient gas angular momentum transfer (Inayoshi et al., 2018a; Sugimura et al., 2018).

Another alternate and more optimistic scenario is the direct collapse of black holes (DCBH) (Oh & Haiman, 2002; Bromm & Loeb, 2003; Begelman et al., 2006; Agarwal et al., 2012; Latif et al., 2013; Dijkstra et al., 2014; Ferrara et al., 2014; Basu & Das, 2019; Chon & Omukai, 2020; Luo et al., 2020). The seed mass produced by this mechanism is $\sim 10^{4-5}$ M$_\odot$, sufficiently high for the seed BH to grow to a 10^9 M$_\odot$ black hole until $z \sim 7$. The basic idea is that a gas cloud in a massive halo with virial temperature $T \gtrsim 8000$ K and no H$_2$ molecules or metals present inside the gas cloud can collapse without fragmentation directly into a SMS which can collapse into seed black holes of similar mass after their lifetime (Umeda et al., 2016). To prevent the formation of H$_2$ molecules, a very high background UV radiation flux is required (Latif et al., 2015; Wolcott-Green et al., 2017). Another key requirement for this scenario are large inflow rates of ~ 0.1 M$_\odot$yr^{-1} which can be obtained easily in metal free halos (Agarwal et al., 2012; Latif et al., 2013; Shlosman et al., 2016; Regan & Downes, 2018; Becerra et al., 2018; Chon et al., 2018; Agarwal et al., 2019; Latif et al., 2020). As a result of the high accretion rate, the SMS becomes inflated and the effective temperature of the SMS drops to several 1000 K (Hosokawa et al., 2012, 2013; Schleicher et al., 2013; Woods et al., 2017; Haemmerlé et al., 2018). Therefore, the radiative feedback becomes inefficient and the rapid accretion flow continues, allowing the SMS to reach the mass of $\sim 10^{4-5}$ M$_\odot$. Recent numerical studies by Latif et al. (2020) and Regan et al. (2020a) have confirmed such large inflow rates lasting for millions of years required to form the DCBHs. However, the presence of even tiny amounts of metals can trigger strong fragmentation through metal line cooling (Omukai et al., 2008; Dopcke et al., 2011; Latif et al., 2016; Corbett Moran et al., 2018; Chon & Omukai, 2020) and reduce the infall rate. Even in metal enriched halos ($Z < 10^{-3} Z_\odot$) where fragmentation takes place, the central massive stars could be fed by the accreting gas and grow supermassive (Chon & Omukai, 2020). Above this threshold value, the gas fragments into lower mass stars and a single object could not be formed. Alternatively, the requirement of a high infall rate could be met by dynamical heating during rapid mass growth of low-mass halos in over-dense regions at high redshifts (Wise et al., 2019), or by massive nuclear inflows in gas-rich galaxy mergers (Mayer et al., 2015). Regan et al. (2020b) have shown that atomic cooling haloes with higher metal enrichment ($Z > 10^{-3} Z_\odot$) can also be possible candidates for the formation of SMSs in the early universe if the metal distribution is inhomogeneous.

As another caveat, we note that even tiny amounts of dust can initiate fragmentation through enhanced cooling. While the presence of such a strong background radiation is rare, it may be possible to find such conditions (Visbal et al., 2014; Dijkstra et al., 2014; Regan et al., 2017). Wise et al. (2019) and Regan et al. (2020c) have recently studied atomic cooling haloes which satisfy the above requirements. Wise et al. (2019) have shown that the requirement of the high UV flux can be significantly reduced in halos with rapid merger histories (Inayoshi et al., 2018b) and in halos located in regions of high baryonic streaming velocities (Naoz et al., 2013; Hirano et al., 2017). In realistic scenarios, there will always be at least some fragmentation happening even if H_2 cooling is suppressed. Using high resolution numerical simulations Latif et al. (2013) have found that fragmentation occurs even in the atomic-cooling regime in 7 out of 9 simulations, unless a subgrid model is added which can provide additional viscosity in the simulation. The final mass of the collapsed object may further be limited by X-ray feedback (Aykutalp et al., 2014). Thus, it motivates to explore other mechanisms of formation of SMBH seed at high redshift.

A third possibility is formation of massive black hole seeds in dense stellar clusters either via runaway collisions of stars, leading to the formation of a supermassive star (SMS) (Portegies Zwart & McMillan, 2002; Portegies Zwart et al., 2004; Freitag et al., 2007; Freitag, 2008; Glebbeek et al., 2009; Moeckel & Clarke, 2011; Lupi et al., 2014; Katz et al., 2015; Sakurai et al., 2017; Boekholt et al., 2018; Reinoso et al., 2018; Schleicher et al., 2019; Alister Seguel et al., 2020) or via the mergers of stellar-mass black holes with other black holes or stars (Giersz et al., 2015; Haster et al., 2016; Rizzuto et al., 2021). In dense high redshift dense stellar clusters, black hole seeds of masses $\sim 10^{2-4}\,M_\odot$ could be formed (Greene et al., 2020) which could grow either via tidal capture and disruption events (Stone et al., 2017; Alexander & Bar-Or, 2017; Sakurai et al., 2019) or via enhanced accretion and collisions (Vesperini et al., 2010; Leigh et al., 2013a; Boekholt et al., 2018). A recent study by Tagawa et al. (2020) has shown that seeds of masses $\sim 10^{5-6}\,M_\odot$ can also be produced via frequent stellar mergers.

Even though the SMSs are one of the most promising progenitors of the observed high redshift quasars, this hypothesis still requires observational verification. Upcoming next generation telescopes e.g. James Webb Space Telescope (*JWST*), *Euclid* and *WFIRST* will be able to detect SMSs at $z \sim 6 - 20$ (Surace et al., 2018, 2019; Woods et al., 2020; Martins et al., 2020). The number of SMSs per unit redshift per unit solid angle, which are expected to be detected at a redshift z, is given by:

$$\frac{dn}{dzd\Omega} = \dot{n}_{\rm SMS}t_{\rm SMS}r^2\frac{dr}{dz}, \tag{3.2}$$

where $\dot{n}_{\rm SMS}$ is the SMS formation rate per unit comoving volume, $t_{\rm SMS}$ is the average lifetime of a SMS as given by eq. 3.9 , and $r(z)$ is the comoving distance to redshift z given by:

$$r(z) = \frac{c}{H_0}\int_0^z \frac{dz'}{\sqrt{\Omega_m(1+z')^3+\Omega_\Lambda}}. \tag{3.3}$$

However, the actual number of SMSs that will be detected will depend on the sensitivity of the instruments (see discussion below). At present the $\dot{n}_{\rm SMS}$ is very poorly constrained.

SMSs could be observed both to be cool and red or hot and blue (Surace et al., 2018, 2019). Whether an observed SMS will be red or blue depends on how quickly and persistently the SMS is growing, whether it is rapidly accreting gas from an atomic-cooling halo or growing from

runaway collisions in a stellar cluster. For rapidly-accreting SMSs, if the star is growing with a rate of $10^{-3}\,M_\odot yr^{-1}$ (Haemmerlé et al., 2018) or less, or if accretion is halted for longer than the thermal timescale of the envelope (Sakurai et al., 2015), then the SMS will contract to the main sequence and becomes a hyper-luminous Pop III star and will be observed as blue, implying a spectral temperature of 10^4 K or higher. For a higher accretion rate $\gtrsim 10^{-3}\,M_\odot yr^{-3}$ the SMS will be red and bloated (Omukai & Palla, 2003; Hosokawa et al., 2012, 2013; Haemmerlé et al., 2018), and the atmospheric temperature will be less than 10^4 K, implying a negligible amount of UV radiation. Haemmerlé et al. (2018) have argued that the critical value decreases below $10^{-2}\,M_\odot yr^{-1}$ if the mass of the SMS is $\gtrsim 600\,M_\odot$. For SMSs growing from runaway collisions in a cluster, it is assumed that a SMS persistently growing via collisions will similarly remain red and bloated as long as it is steadily bombarded (Reinoso et al., 2018). The deposition of the kinetic energy causes the star to bloat post-collision, which then radiates away on a Kelvin-Hemholtz timescale (Eq. 3.9). However, if after coalescence the star is allowed to thermally relax, then it will contract to become blue. If the star goes through complete thermal relaxation, it will become a very hot source of ionization (Woods et al., 2020). The relevant timescales both for collisions and accretion depend on the environment, but will be of order of one million years or so (e.g. Boekholt et al., 2018); and also the Kelvin-Helmholtz timescale will be of similar magnitude. However the timescale is expected to depend on environmental conditions e.g. the number density of stars (Leigh et al., 2017a) and may also be enhanced in the presence of accretion. If detected via JWST or other missions, the star may be either in the hot or blue state depending on its environment. In general, however, the SMS phase is expected to be short lived, so the most likely observable would be a SMBH in a star cluster, potentially still with gas in its environment.

Using existing data such as the Hubble Ultra Deep Field, it is currently not possible to detect either of these SMSs, as the AB magnitude limit is 29 at 1.38 μm, well below that expected for either type of SMS even at $z \sim 6$. However, with JWST which has NIRCam AB magnitude limits of 31.5, it will be possible to detect cooler, redder SMSs at $z \sim 18 - 20$ and hotter, bluer SMSs at $z \lesssim 13 - 10$ due to quenching by their accretion envelopes (Surace et al., 2019). Even though current Euclid and WFIRST detection limits (26 and 28, respectively) are well below the H band magnitudes of both stars at $z \sim 6 - 20$, both of them would be able to detect blue SMSs as even a slight amount of gravitational lensing will boost the fluxes of these blue SMSs above the detection limits of these two missions. Martins et al. (2020) found some important spectral features in the observational properties of SMSs with mass range $\sim 10^3 - 5 \times 10^4\,M_\odot$. They have computed the spectra of SMSs for non-local thermal equilibrium spherical stellar atmosphere models. According to their model, cool SMSs with effective temperatures of $\sim 10^4$ K will exhibit a Balmer break in emission, which is not expected for normal stars. Hotter SMSs with effective temperatures of $\gtrsim 4 \times 10^4$ will exhibit a Lyman break in emission. However, the resonant scattering of Lyα photons by the neutral IGM at $z > 6$ will be a great challenge for observations. It is important to note that the detections of SMSs discussed in Surace et al. (2018, 2019) are for high accretion rate $\sim 1\,M_\odot yr^{-1}$. Also, it will be difficult to observe the hotter blue supergiants at high redshifts due to the quenching effect mentioned above. Moreover, we do not expect the observations to measure anything related to SMSs directly. It would purely be a color measurement, which would be possible even if the entire cluster is unresolved and observed as a point-source. As our measurement capabilities increase with the upcoming telescopes to probe higher redshifts, a simple color measurement could be quite useful and informative,

purely because these processes we quantify would yield a color inconsistent with a single burst of star formation. So potentially one can just compare to stellar population synthesis models. What future telescopes can do is still an open question.

As another potential caveat, we note the importance to distinguish SMS signatures from other types of stars in massive star clusters, such as extended horizontal branch stars or A-type, which could even be brighter than blue stragglers in the same clusters (Leigh et al., 2016). Another challenge related to the observation of blue SMSs will be to distinguish them from hot blue dark stars powered by dark matter annihilation (e.g. Freese et al., 2010, 2016; Surace et al., 2019). One way to distinguish them is using the prominent continuum absorption features on the spectra redward of Lyα in the rest frame of the SMS due to the high accretion rate, which are absent from the spectra of blue dark stars. A very prominent Lyα line is found in blue SMS spectra due to pumping of the accretion envelope by high-energy UV photons from the star. These spectral features will be really important to distinguish blue SMSs from hot dark stars of similar mass. A dark star will not have these spectral features due to the absence of a dense accretion shroud.

Studies have found that many galaxies harbor massive NSCs (Carollo et al., 1997; Böker et al., 2002; Leigh et al., 2012, 2015; Georgiev et al., 2016) with masses of $\sim 10^{4-8}$ M$_\odot$. Many of these galaxies host a central SMBH (Kormendy & Ho, 2013). Interestingly, studies have found correlations between both the SMBH mass and the NSCs mass with the galaxy mass (Ferrarese et al., 2006; Rossa et al., 2006; Leigh et al., 2012; Scott & Graham, 2013; Seth et al., 2020). In many galaxies NSCs and SMBHs co-exist (Seth et al., 2008; Graham & Spitler, 2009; Georgiev et al., 2016; Nguyen et al., 2019). Galaxies like our own (Schödel et al., 2014), M31 (Bender et al., 2005a) and M32 (Bender et al., 2005b) host a SMBH and a NSC in the center. It therefore makes sense to consider a link between NSCs and SMBHs. Studies have shown that SMBH seeds could be formed inside NSCs via runaway tidal encounters (Stone et al., 2017) or from core collapse and stellar collisions (Devecchi & Volonteri, 2009; Devecchi et al., 2010; Davies et al., 2011) or by gas inflows (Lupi et al., 2014). Recent studies by Kroupa et al. (2020) and Natarajan (2021) investigated black hole accretion inside NSCs. In depth reviews about NSCs can be found in Neumayer et al. (2020).

In this paper, we explore high-redshift, metal-poor NSCs as the possible birthplaces of SMSs via gas accretion and runaway stellar collisions. Low metallicity may favor the formation of very dense clusters, as fragmentation will occur at higher density, while the mass loss from winds becomes negligible (Vink et al., 2001), thereby making this formation channel more effective. In addition, in low metallicity environments the gas will be warmer, thereby contributing to higher accretion rates through a higher speed of sound.[1] Here we explore how runaway collisions between stars and gas accretion onto the stars can lead to the formation of a SMS in such clusters.

We use N-body simulations to model runaway collisions and gas accretion in dense NSCs. We describe our simulation setup in Sec. 3.2. Our results are presented in Sec. 3.3 and the final discussion is given in Sec. 4.5 along with a summary of our main conclusions.

Similar work had been done by Boekholt et al. (2018); Reinoso et al. (2018) for Pop III

---

[1]In the regime where self-gravity regulates fragmentation and at least the initial masses of the clumps, the accretion rate can be estimated as the Jeans mass over the free-fall time, leading to a dependency on sound speed cubed.

stellar clusters. The most important distinctions between our work and the previous works are that we study clusters with higher initial stellar mass (10^5 M$_\odot$), higher number of stars (5000), a Salpeter type initial mass function (IMF), and more sophisticated and physically motivated accretion scenarios. We further provide a more detailed analysis here on the comparison of the timescales for collisions and accretion.

3.2   Simulation Setup

The complicated physical processes operating together in stellar clusters include gravitational N-body dynamics, gravitational coupling between the stars and the gas, accretion physics, stellar collisions and mass growth due to accretion and collisions. Properly accounting for all of these physical processes provides a significant challenge with respect to the modeling. Moreover, it is computationally costly to model clusters consisting mostly of massive main sequence (MS) stars, due to the large number of stars. We use the Astrophysical MUlti-purpose Software Environment (AMUSE) (Portegies Zwart et al., 2009, 2013; Pelupessy et al., 2013; Portegies Zwart & McMillan, 2018) to model the nuclear clusters and include all the physics mentioned above. AMUSE is very efficient in including new physics such as the mass-radius relation, accretion physics, collisional dynamics, and coupling all of these to existing N-body codes. In this section, we present and discuss all the physical processes that we include in our simulation and how we couple them into the numerical model.

3.2.1   Initial Conditions

We model the NSCs with MS stars embedded in a stationary gas cloud. For simplicity, we assume that the stars and the gas are equally distributed, i.e., both the gas mass (M_g) and gas radius (R_g) are equal to the mass (M_{cl}) and radius (R_{cl}) of the stellar cluster. Both the cluster and gas follow a Plummer distribution with the same characteristic Plummer radius (Plummer, 1911). The Plummer density distribution is given as

$$\rho(r) = \frac{3M_{cl}}{4\pi b^3}\left(1 + \frac{r^2}{b^2}\right)^{-\frac{5}{2}}, \tag{3.4}$$

where M_{cl} is the mass of the cluster and b is the Plummer length scale or the Plummer radius that sets the size of the cluster core. The Plummer length scale of the cluster (or the gas) is equal to one fifth of R_{cl} (or R_g). We introduce a cut-off radius, equal to five times the Plummer radius, after which the density is set to zero in order to create a stable cluster with finite total mass and to make sure each star initially is within the gas cloud. The initial parameters for the numerical setup are M_{cl}, R_{cl}, M_g, R_g, and the number of stars N. For the initial mass of the stars we consider a Salpeter initial mass function (IMF) (Salpeter, 1955) given by :

$$\xi(m)\Delta m = \xi_0\left(\frac{m}{M_\odot}\right)^{-\alpha}\left(\frac{\Delta m}{M_\odot}\right), \tag{3.5}$$

with three different mass ranges, $10\,M_\odot - 100\,M_\odot$, $10\,M_\odot - 120\,M_\odot$, $10\,M_\odot - 150\,M_\odot$, assuming a power-law slope of $\alpha = 2.35$. Since our main goal is to explore the interplay between

accretion physics and the dynamics of the runaway collisions producing a massive object, we do not take into account complicating factors such as the effect of cluster rotation or an initial binary fraction, which would also be highly uncertain in the context considered here, while significantly increasing the computational expense of our simulations.

The gravitational interactions between the stars are modelled using the N-body code ph4 based on a fourth-order Hermite algorithm (Makino & Aarseth, 1992). The Hermite 4th order integrator is a widely used N- body integrator scheme. It is based on a predictor-corrector scenario, i.e. it uses an extrapolation of the equations of motion to get a predicted position and velocity at some time, then using this information it calculates the new accelerations, then based on finite differences terms it corrects the predicted values using interpolation. A polynomial adjustment in the gravitational forces evolution among the time is used, because the force acting over each particle changes smoothly. It is called fourth-order, because the predictor consider the contributions of the third order polynomial and after obtaining the accelerations, it adds a fourth-order corrector term. The gravitational effect of the gas cloud is included via an analytical background potential coupled to the N-body code using the BRIDGE method (Fujii et al., 2007). The BRIDGE method consider a star cluster orbiting a parent galaxy. Interactions among the particles comprising the galaxy, and between galaxy particles and cluster stars, are computed using a hierarchical tree force evaluation method (Barnes & Hut, 1986). More details about ph4 and BRIDGE can be found in (Portegies Zwart & McMillan, 2018). This allows us to incorporate the gravitational forces felt by the stars both due to the gas and the stellar component. In other words, the motions of the stars are controlled by the total combined potential of the gas and stars. As explained in more detail in the subsequent sections, we consider direct accretion onto stars but do not factor in gas dynamical friction. This is because in previous works it has been shown to be inefficient, although over sufficiently long timescales it can contribute to cluster contraction (Leigh et al., 2013b, 2014).

3.2.2 Mass-radius relation

The mass-radius ($M_* - R_*$) relation of the stars will play an important role in determining the number of collisions via the collisional cross section. Since the runaway collisions have to start before the most massive stars in the cluster turn into compact remnants, it is justified to consider all stars to be initially on the MS. In Fig. 3.1 we show the $M_* - R_*$ relations obtained from different studies (Bond et al., 1984; Demircan & Kahraman, 1991; Schaller et al., 1992). The Demircan & Kahraman (1991) and Schaller et al. (1992) data points match quite well below $M_* \lesssim 50 \, \mathrm{M_\odot}$, while the Bond et al. (1984) and Schaller et al. (1992) data points match quite well above $M_* \gtrsim 50 \, \mathrm{M_\odot}$. We therefore combine these relations and adopt a $M_* - R_*$ relation as outlined below. The $M_* - R_*$ relation for stars more massive than $M_* \gtrsim 100 \, \mathrm{M_\odot}$ is of crucial importance, as it determines the size of the runaway collision product. Unfortunately, the radius of stars with $M_* \gtrsim 100 \, \mathrm{M_\odot}$ is poorly understood. SMSs may develop a very extended envelope of very low density (Ishii et al., 1999; Baraffe et al., 2001). However, this extended envelope contains only a few percent of the total stellar mass, so it may play a negligible role in collisions. Moreover, such extended envelopes are not present in low metallicity main sequence stars (Baraffe et al., 2001), which are our main focus in this paper. Overall, the relation we

employ is given as

$$\frac{R_*}{R_\odot} = 1.60 \times \left(\frac{M_*}{M_\odot}\right)^{0.47} \quad \text{for } 10\,M_\odot \lesssim M_* < 50\,M_\odot, \tag{3.6}$$

$$\frac{R_*}{R_\odot} = 0.85 \times \left(\frac{M_*}{M_\odot}\right)^{0.67} \quad \text{for } 50\,M_\odot \lesssim M_*, \tag{3.7}$$

where Eq. 3.6 is adopted from Bond et al. (1984) and Eq. 3.7 is adopted from Demircan & Kahraman (1991). One key quantity in our work is the stellar lifetime. The MS lifetime is given as (Harwit, 1988)

$$\tau_{MS} = 10^{10} \left(\frac{M_\odot}{M_*}\right)^{2.5} \text{yr}. \tag{3.8}$$

For a $M_* \sim 20\,M_\odot$ it is ~ 5.6 Myr. However, for $M_* \gtrsim 40\,M_\odot$, the lifetime is almost constant ($\sim 3.5 - 5$ Myr) and independent of metallicity (Hurley et al., 2000). On the other hand, the SMS evolves over Kelvin-Helmholtz (KH) timescale (Janka, 2002)

$$t_{KH} = 6.34 \times 10^8 \left(\frac{M_*}{M_\odot}\right)^{-1} \text{yr}. \tag{3.9}$$

We stop our simulation at 5 Myr as we are mostly interested in the early phases of cluster evolution corresponding to the most rapid rates of black hole seeds mass growth, in order to quantify the attainable final black hole masses for each of our simulation models. We do not take into account the change in stellar radius due to stellar evolution of MS stars despite the fact that stellar evolution could play an important role determining the final mass of the SMS (Glebbeek et al., 2013; Katz, 2019). We also ignore the rotation of the stars which could significantly influence the evolution of the massive stars and hence the final mass of the SMS (Maeder & Meynet, 2000; Leigh et al., 2016). Our main goal here is to build a simple model and to better understand the complicated physics involved in the study.

3.2.3   Gas accretion

Gas accretion plays a crucial role in our simulations as the stellar masses and radii can increase significantly depending on the accretion model, and hence the number of collisions will be increased. In our model the gas that is being accreted by the stars is assumed to be in a stationary state. We impose momentum conservation during the accretion process, which means the stars will slow down as they gain mass, and fall into the potential well of the cluster. The mass accreted onto the stars is removed from the (static) gas, leading to its depletion and eventually to a transition where the cluster evolution is determined only by N-body dynamics. However, gas motions do not follow the stellar motions and as a result sometimes accretion could add or remove momentum, less or more, respectively. In order to model the gas dynamics we need hydrodynamic simulations.

We have considered different accretion scenarios in our work. As a first simplified choice we study the effect of a constant accretion rate three different accretion rates of 10^{-4}, 10^{-5} and $10^{-6}\,M_\odot \text{yr}^{-1}$, which roughly correspond to the Eddington and Bondi accretion rates under different assumptions for the mass of the central object. Even though it is highly unlikely that
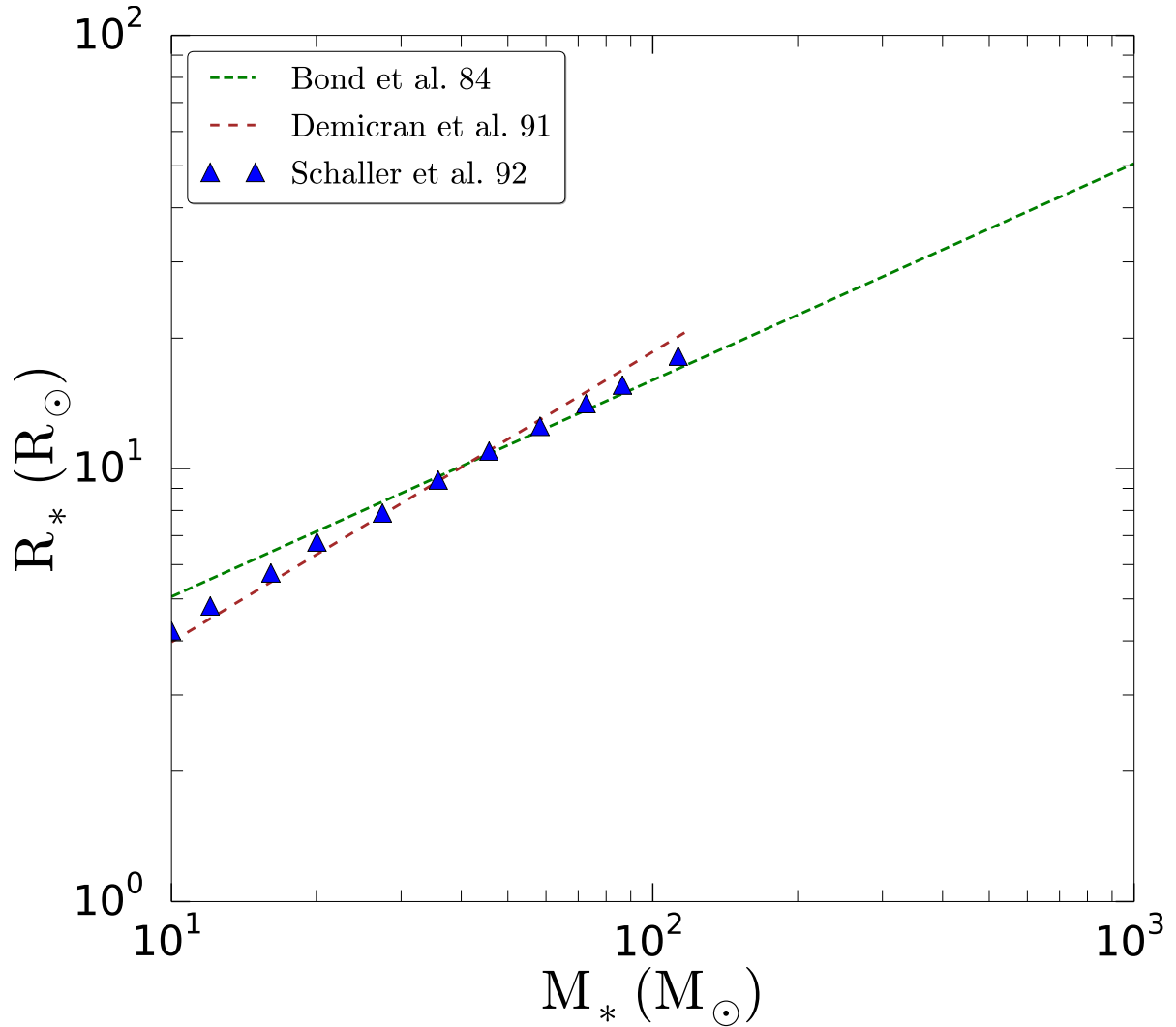
Figure 3.1: $M_* - R_*$ relations for MS stars from different studies. For masses in the range $10 - 120 \, M_\odot$ we adopted the Demircan & Kahraman (1991); Schaller et al. (1992) data. The green dashed lines show the data from Bond et al. (1984). Even though the model is for really massive stars of mass $\gtrsim 10^4 \, M_\odot$, we can see it fits perfectly for masses $\gtrsim 50 \, M_\odot$.

all stars in the cluster will accrete at the same constant rate, and individual star accretion might even be episodic (Vorobyov & Basu, 2006, 2015), this ad-hoc approximation is a good starting point to understand how the interplay of accretion and collisions works in the cluster.

Next we consider the Eddington accretion rate given as

$$\dot{M}_{\mathrm{Edd}} = \frac{4\pi G M_*}{\epsilon \kappa c_{\mathrm{s}}},$$ (3.10)

where c_{s} is the speed of sound in the gas, ϵ is the radiative efficiency, i.e. the fraction of the rest mass energy of the gas that is radiated and κ is the electron scattering opacity. Using $\kappa = 0.4\,\mathrm{cm}^2\,\mathrm{g}^{-1}$ and $\epsilon = 0.1$, Eq. 3.10 can be written as

$$\dot{M}_{\mathrm{Edd}} = 2.20 \times 10^{-8} \left(\frac{M_*}{\mathrm{M}_\odot} \right)\ \mathrm{M}_\odot \mathrm{yr}^{-1}.$$ (3.11)

Finally we consider the Bondi-Hoyle-Lyttleton accretion. Simulations (Bonnell et al., 2001) have shown that in larger clusters the stars accrete unequally, with the stars near the core accreting more than those near the outer envelopes of the cluster. This is due to the fact that the gas mass is accumulating near the core due to the cluster potential where it can be accreted by the stars. Even initially uniform clusters show a position dependent accretion as the gas and stars redistribute themselves in the host cluster potential. As a result of the position-dependent accretion, the final configurations show a significant amount of mass segregation.

In principle the accretion rate of a star will depend on its cross section πR_{acc}^2, where R_{acc} is the accretion radius, on the gas density ρ_∞, and the relative velocity of the star with respect to the gas v_∞, as

$$\dot{M} = \pi v_\infty \rho_\infty R_{\mathrm{acc}}^2.$$ (3.12)

In the original Hoyle–Lyttleton (HL) problem the accretion radius in the supersonic regime is given as (Hoyle & Lyttleton, 1939, 1940a,b)

$$R_{\mathrm{HL}} = \frac{2 G M_*}{v_\infty^2},$$ (3.13)

which leads to the HL accretion rate:

$$\dot{M}_{\mathrm{HL}} = \frac{4\pi G^2 M_*^2 \rho_\infty}{v_\infty^3}.$$ (3.14)

However, Bondi (1952) defined the Bondi radius as

$$R_{\mathrm{B}} = \frac{G M_*}{c_{\mathrm{s}}^2}.$$ (3.15)

The flow outside this radius is subsonic and the density is almost uniform, while inside the Bondi radius the gas becomes supersonic. This led Bondi (1952) to propose an interpolated Bondi-Hoyle (BH) formula:

$$\dot{M}_{\mathrm{BH}} = \frac{2\pi G^2 M_*^2 \rho_\infty}{(v_\infty^2 + c_{\mathrm{s}}^2)^{3/2}}.$$ (3.16)

Studies have shown that there will be an extra factor of 2 which leads to the final accretion formula given as

$$\dot{M}_{\text{BH}} = \frac{4\pi G^2 M_*^2 \rho_\infty}{(v_\infty^2 + c_s^2)^{3/2}}.$$ (3.17)

This accretion rate can be written as in Eq. 2 of Maccarone & Zurek (2012):

$$\dot{M}_{\text{BH}} = 7 \times 10^{-9} \left(\frac{M_*}{M_\odot}\right)^2 \left(\frac{n}{10^6 \, \text{cm}^{-3}}\right)^2 \left(\frac{\sqrt{c_s^2 + v_\infty^2}}{10^6 \, \text{cm s}^{-1}}\right)^{-3} \, M_\odot \text{yr}^{-1}.$$ (3.18)

A recent study by Kaaz et al. (2019) has shown that the BH accretion rate will depend on the characteristic accretion radius of the cluster R_{acc} and the mean separation between stars $R_\perp$, where $R_\perp = R_{\text{cl}} N^{-1/3}$. The average accretion rate of an individual star is given as

$$\langle \dot{M}_{\text{BH}} \rangle = \begin{cases} \dot{M}_{\text{BH}}, & \text{when } R_\perp \gg R_{\text{acc}}, \\ N \times \dot{M}_{\text{BH}}, & \text{when } R_\perp \leq R_{\text{acc}} \end{cases}$$ (3.19)

In our work we consider a BH accretion rate given by Eq. 3.19, where $\dot{M}_{\text{BH}}$ is given by Eq. 3.18.

3.2.4 Handling collisions

We adopt the sticky-sphere approximation to model collisions between the main sequence stars (see, for example, Leigh & Geller (2012); Leigh et al. (2017b). If the distance between the centers of two stars is less than the sum of their radii, we assume that the stars have merged and we replace them with a single object whose mass is equal to the sum of the masses of the colliding stars. We consider the collision product to be a MS star and the radius of the object to be determined by the $M_* - R_*$ relation described in Eqs. 3.6 and 3.7. We assume that linear momentum is conserved during the collision.

However, studies have shown that the mass is not necessarily conserved during the collision of stars (Sills et al., 2002; Dale & Davies, 2006; Trac et al., 2007). Alister Seguel et al. (2020) have shown that the final mass of the colliding objects could change a lot depending on the mass loss rate. Glebbeek et al. (2013) have shown that the mass loss rate depends on the type of stars colliding. In our study, all the stars are MS stars and we have assumed both a mass loss recipe as given by Eq. 3 of Katz et al. (2015),

$$\Delta M = \min \left[0.062 \frac{M_2}{0.7 M_1}, 0.062\right] (M_1 + M_2),$$ (3.20)

where M_1 and M_2 are the masses of the colliding stars, as well as constant mass loss rates of 3% and 5%. Henceforth, we refer to Eq. 3.20 as K15.

3.2.5 Stability of numerical setup

While our work is based on the setup previously tested and employed by Boekholt et al. (2018) and Alister Seguel et al. (2020), we test the stability pursuing a reference run where both the accretion and collisions are deactivated, to show that our setup corresponds to an overall stable

initial condition. For this setup, we employ $N = 5000$ particles, $M_{cl} = M_g = 1.12 \times 10^5 \, M_\odot$, $R_{cl} = R_g = 1$ pc, and we assume a Salpeter IMF with masses between $10 - 100 \, M_\odot$. As accretion and collisions are switched off, we find the gas and stellar mass to be consistent. The time evolution of the Lagrangian radii which is the radius of an imaginary sphere around the centre of the stellar cluster containing a fixed fraction of its mass, is shown in Fig. 3.2.

3.3 Results

The main results of our simulations are presented in this section. We start by presenting our reference run in section 3.3.1. The dependence on the prescription for the accretion rate is explored in section 3.3.2, and an analysis in terms of collision and accretion time scales is provided in section 3.3.3. The influence of the IMF is examined in section 3.3.4, the dependence on the cluster radius in section 3.3.5, and the implications of mass loss are finally examined in section 3.3.6. The summary of the initial conditions and results is presented in table 3.1.

3.3.1 Reference run

We start by describing our reference run with $N = 5000$, $M_{cl} = M_g = 1.12 \times 10^5 \, M_\odot$, $R_{cl} = R_g = 1$ pc, assuming a Salpeter IMF within a stellar mass interval of $10 - 100 \, M_\odot$ and a constant accretion rate of $\dot{m} = 10^{-6} \, M_\odot \, \text{yr}^{-1}$. The result of the simulation is shown in Fig. 3.3. In this configuration, accretion occurs rather gradually, and the gas mass decreases only by about 20% over 5 Myr, while the stellar mass increases by the same amount. As shown in Leigh et al. (2014) and as reflected in the evolution of the Lagrangian radii, the inner part of the cluster, containing 10% of the mass, goes through contraction and even the radius containing 50% of the mass shows slight contraction, while the outer 90% radius is moderately expanding. The first collision in the cluster occurs after about 1 Myr and in total about 20 collisions occur over 5 Myr, where the time interval between the collisions decreases at later times, potentially due to the larger cross section of the central massive object. It is important to say that not all these collisions are with the central object, but nevertheless they lead to the formation of more massive objects within the star cluster, and particularly in the last 1.5 Myr the collision products eventually merge with the central object, thereby contributing to its growth.

We now explore how these results depend on the adopted value of the accretion rate. We first note that if we decrease the accretion rate by a factor of 5, no collisions occur and the results are consistent with a simulation where the accretion and collisions are switched off. On the other hand, if the accretion rate is increased to a value of $\dot{m} = 10^{-5} \, M_\odot \, \text{yr}^{-1}$, it has a considerable impact on the evolution of the cluster (see Fig. 3.4). First, we note in this case that the gas mass will be fully depleted after slightly more than 2 Myr, and the stellar mass therefore reaches a total value of $2.24 \times 10^5 \, M_\odot$. Stellar collisions are considerably enhanced. They occur relatively early on and increase more rapidly after about 1.5 Myr, reaching a total of about 500 collisions within 5 Myr. The mass of the MMO reaches about $3 \times 10^4 \, M_\odot$ in the same time, predominantly driven by the merger of collision products. The 10% Lagrangian radius undergoes initially moderate contraction as before. It however decreases rapidly after 3 Myr, as the accretion rapidly accelerates core collapse; our highest accretion rates achieve core collapse within one million years (see below). The 50% Lagrangian radius slightly decreases
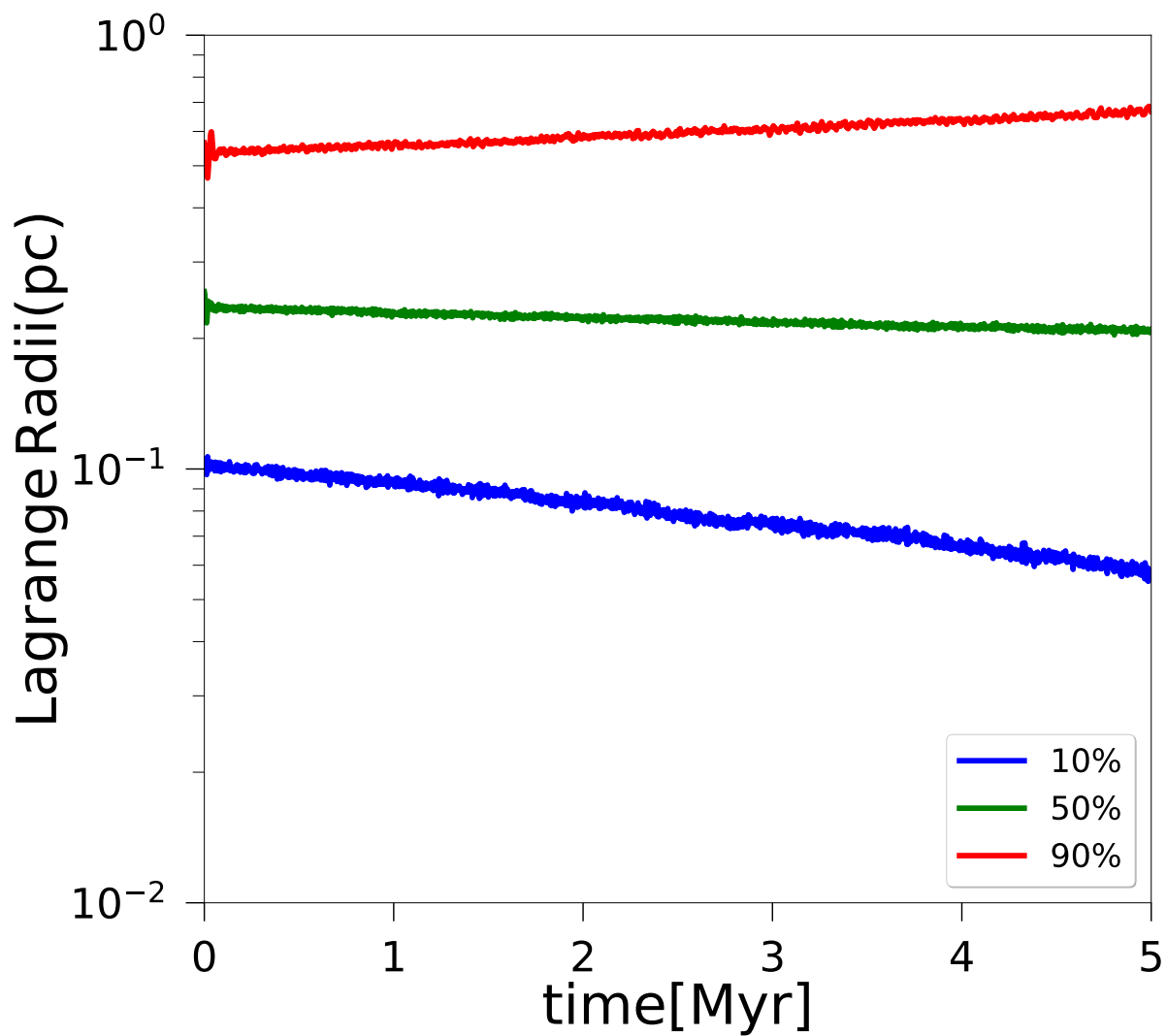
Figure 3.2: Evolution of the Lagrange Radii for a test run without accretion with $N = 5000$ particles, $M_{cl} = M_g = 1.12 \times 10^5 \, M_\odot$, $R_{cl} = R_g = 1$ pc, assuming a Salpeter IMF with mass range $10 - 100 \, M_\odot$.

for the first 1.3 Myr and subsequently shows moderate expansion. The trend is very similar for the 90% Lagrangian radius. This trend has been seen in previous simulations (e.g. Leigh et al., 2014), especially after the formation of a massive object in the center (Boekholt et al., 2018; Alister Seguel et al., 2020).

As an even more extreme case, we consider the evolution for an accretion rate of $\dot{m} = 10^{-4}\,M_\odot\,yr^{-1}$, as shown in Fig. 3.5. In this case, the gas mass is fully depleted after ~ 0.2 Myr. Collisions are considerably enhanced and grow rapidly from about 0.2 Myr onwards, reaching a total number of about 550 collisions after 5 Myr. The mass of the MMO increases very rapidly due to mergers of collision products, reaching $10^4\,M_\odot$ already after 0.8 Myr, and about $3 \times 10^4\,M_\odot$ after 5 Myr. The final mass of the MMO is thus very similar to what is found in the case of an accretion rate of $\dot{m} = 10^{-5}\,M_\odot\,yr^{-1}$, however the evolution is considerably accelerated, thus reaching the final mass earlier. The result indicates that the mass of the MMO does not become much larger than about 10% of the initial cluster mass. However, this not a fundamental limit. If all the gas gets accreted (which was seen in some of our simulations), the MMO can gain more mass via accretion and then collisions will only increase it more. We verified that for all our models the free-fall time of the gas is shorter than the gas depletion time, i.e., all the gas will be replenished and stars will keep accreting.[2] Dynamically high accretion rates will push clusters into core collapse on very short timescales compared to the rate from two-body relaxation.

3.3.2 Dependence on the physical recipe for the accretion rate

As a next step, we explore the dependence of the evolution in the NSCs for different physical assumptions regarding the accretion rate, i.e. going beyond the simplified assumption of a constant accretion rate. In Fig. 3.6, we show the expected time evolution for the case of Eddington accretion scenario given by Eq. 4.10. In this case, we find that the evolution is comparable to what we found for a constant accretion rate of $\dot{m} = 10^{-6}\,M_\odot\,yr^{-1}$. The gas mass decreases by about 15% over 5 Myr, while the stellar mass increases by the same amount. The evolution of the Lagrangian radii is rather stable, with the 10% and 50% radii slightly contracting, and the 90% radius moderately expanding. The first collision occurs after about 1.5 Myr, and about 15 collisions are reached after 5 Myr. The growth of the MMO occurs most rapidly after about 3.5 Myr, and reaches about $900\,M_\odot$. The results show that relevant numbers of collisions could occur, which can lead to a SMS mass of $\sim 10^3\,M_\odot$ in the Eddington case.

As a more optimistic scenario, we also consider the case of Bondi accretion given by Eq. 4.11. The results are shown in Fig. 3.7. As the Bondi accretion rate $\dot{M}_{BH} \propto M_*^2$, this recipe has a strong impact on the evolution of the MMO. Initially the evolution takes place more slowly, due to an initially lower accretion rate, but is rapidly enhanced at late times as the mass of the accretor grows. As seen in the evolution of the gas and stellar mass, for a long time the accretion rates are lower than in the Eddington scenario, and only after about 4.7 Myr the evolution becomes very rapid, and accelerates so much that the gas becomes fully depleted within a short time, while the stellar mass increases in the same way. The first collision

---

[2]If the free-fall time is longer than the gas depletion time, then there will be a rapid initial phase of accretion, followed by very little accretion while the gas slowly sinks down the cluster potential, eventually increasing again once the gas density gets high enough.
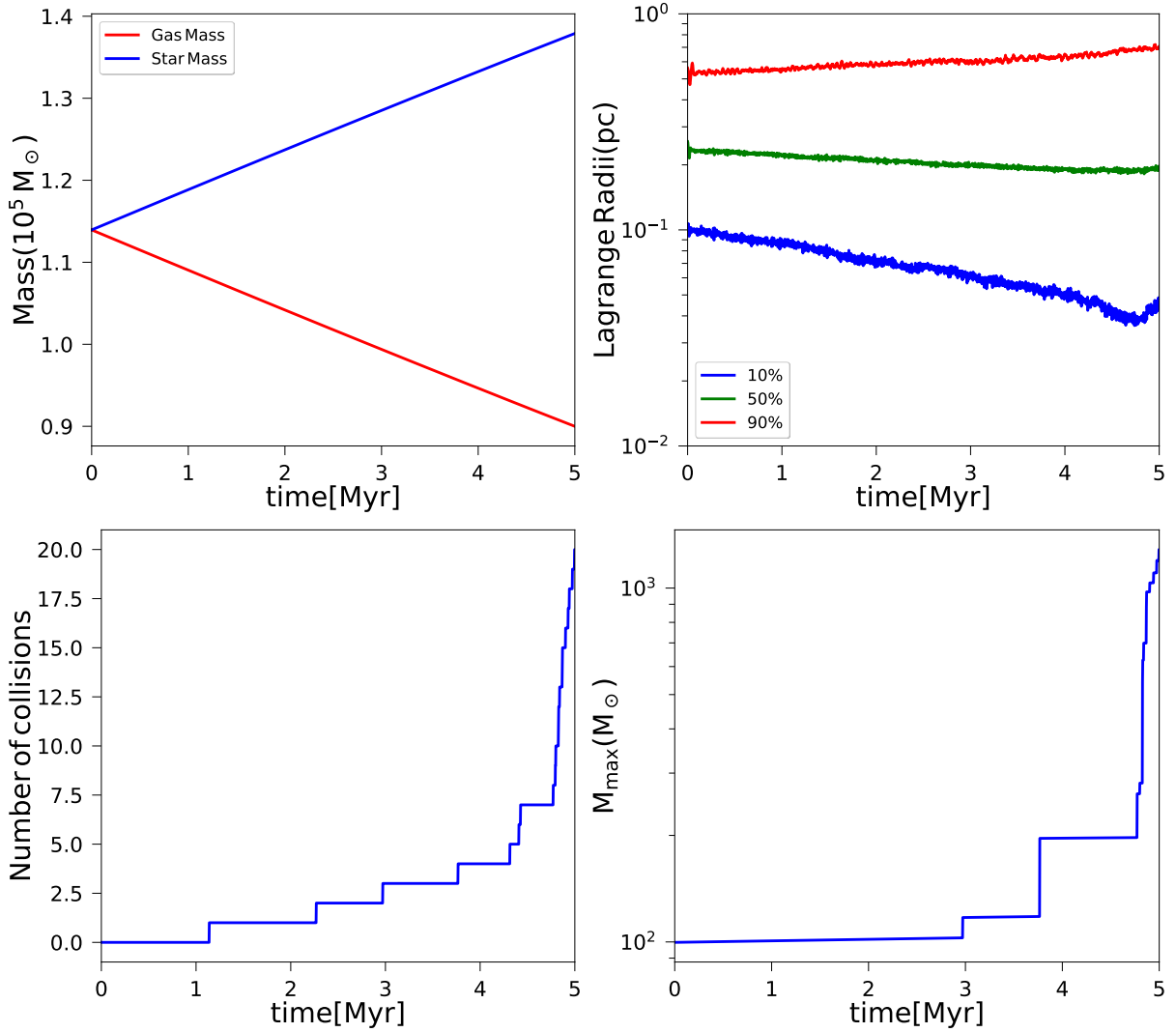
Figure 3.3: Simulation with $N = 5000$, $M_{cl} = M_g = 1.12 \times 10^5 \, M_\odot$, $R_{cl} = R_g = 1$ pc, assuming a Salpeter IMF between $10 - 100 \, M_\odot$ and an accretion rate of $\dot{m} = 10^{-6} \, M_\odot \text{yr}^{-1}$. The top left panel shows the evolution of gas and stellar mass as a function of time, the top right panel the evolution of the Lagrangian radii, the bottom left panel the total number of collisions as a function of time, and the bottom right panel the evolution of the mass of the MMO as a function of time.
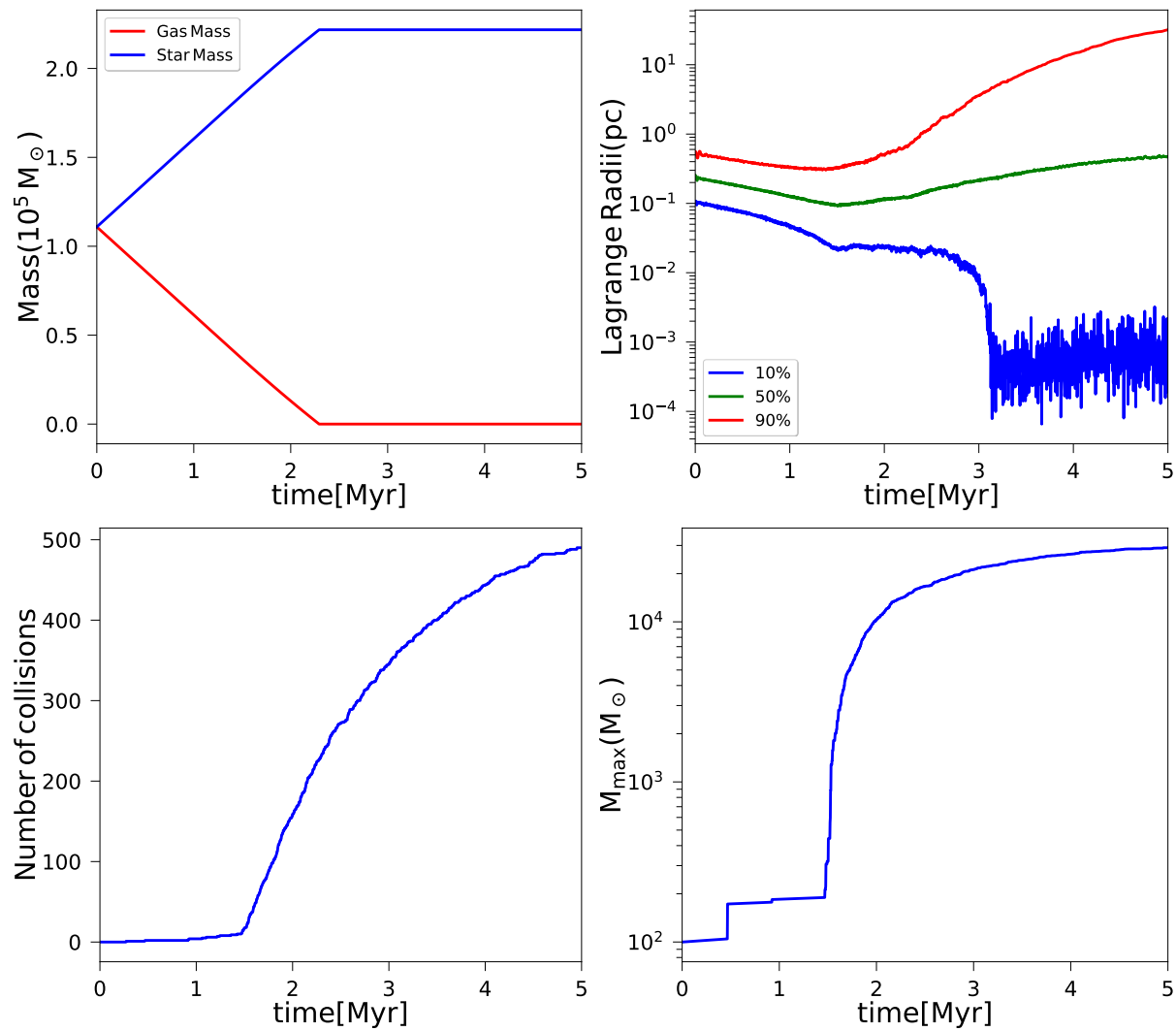
Figure 3.4: Same as in Figure 3.3, but assuming instead $\dot{m} = 10^{-5}\,\mathrm{M_\odot yr^{-1}}$.
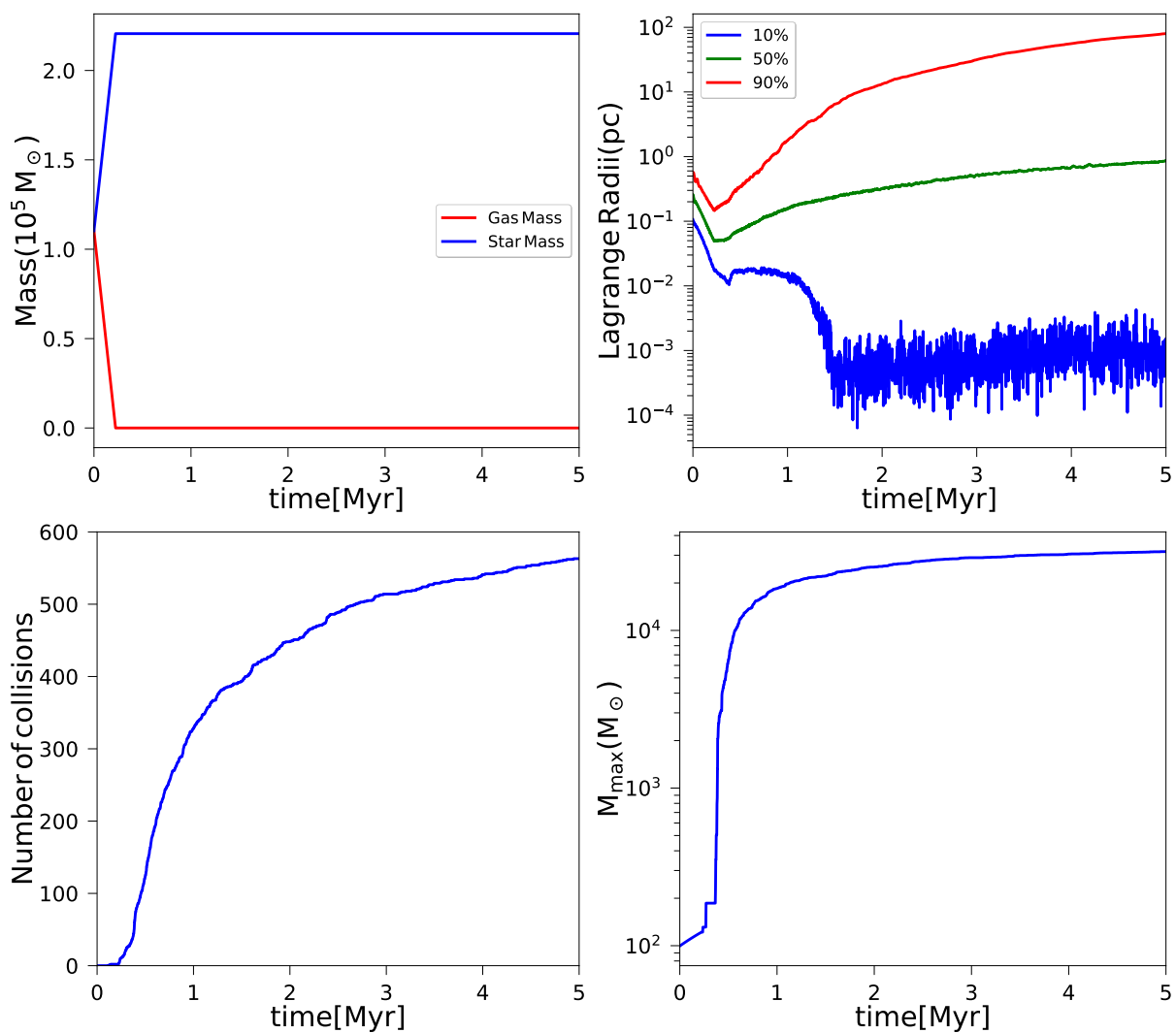
Figure 3.5: Same as in Figure 3.3, but assuming instead $\dot{m} = 10^{-4}\,\mathrm{M_\odot yr^{-1}}$.

occurs after about 1.5 Myr and in total about 20 collisions occur before the accretion becomes strongly accelerated, with the MMO reaching about $200\,M_\odot$ within the first 4 Myr. During the accelerated phase of the evolution, more than 120 additional collisions occur, and the final mass reaches about $10^5\,M_\odot$. While the Lagrangian radii are very stable for the first 4.7 Myr, they react to the extreme evolution occurring subsequently, with the 10% Lagrangian radius strongly decreasing due to the formation of the MMO, and the same slightly later even for the 50% radius. The 90% radius shows first a minor decrease at the time when the evolution accelerates and subsequently expands. The evolution in this scenario is sufficiently extreme that our model assumptions will break down early on due to a lack of gas replenishment, so this part of our results needs to be regarded with caution.

The evolution of both the average accretion rate in the cluster and the maximum accretion rate is shown for the models with Eddington and Bondi accretion in Fig. 3.8 (in the case of constant accretion rates, the plots would be trivial). The average accretion rates are almost constant as a function of time and increase only at late times. In the Eddington scenario, this increase is hardly visible by eye, while it is much more pronounced in the case of Bondi accretion, due to the steep increase of the accretion rate of the MMO, which then affects also the calculation of the average. We indeed find that the Bondi accretion rate for the MMO increases by more than two orders of magnitude, while it is about an order of magnitude in the case of Eddington accretion.

3.3.3 Collision vs accretion time scale

To determine the respective relevance of collisions vs accretion for a single object, we aim in the following at a systematic comparison of the collision timescale (t_{coll}) and accretion timescale (t_{acc}). To evaluate collision timescale for the MMO, we adopt the formulation of Leigh et al. (2017b) for a system consisting of heavy particles with mass m_A and light particles with mass m_B:

$$t_{\text{coll}} = \frac{G^3 m_A^{1/2} \bar{m} M_{\text{cl}}^{13/2}}{12\sqrt{2} m_B^{3/2} N_B (R_A + R_B)^2 |E|^{7/2}}, \qquad (3.21)$$

where $\bar{m}$ is the average mass of all particles, R_A and R_B the radii of particles of type A and B, N_B is the number of particles of type B, and $|E|$ the total energy of the stars in the cluster, which we evaluate using the virial theorem and taking into account the gravitational potential from gas and stars via

$$|E| = \frac{G M_{\text{tot}} M_{\text{cl}}}{2 R_{\text{cl}}}, \qquad (3.22)$$

with $M_{\text{tot}} = M_{\text{cl}} + M_g$ being the total mass. It is important to note that eq. 3.21 does not incorporate the effect of accretion on the collisions probability, while our numerical experiments in section 3.3.1 establish that accretion enhances collisions. The collision timescale employed here for collisions with the MMO can in this sense be regarded as an upper limit. As demonstrated by Barrera et al. (2020), in the absence of accretion, the prescription works best for lower particle numbers and less extreme mass ratios. Once one object becomes more massive than the rest, quasi-Keplerian motions and a loss cone formalism start to become more relevant. We do not account for that here and neglect these effects in the context of the collision
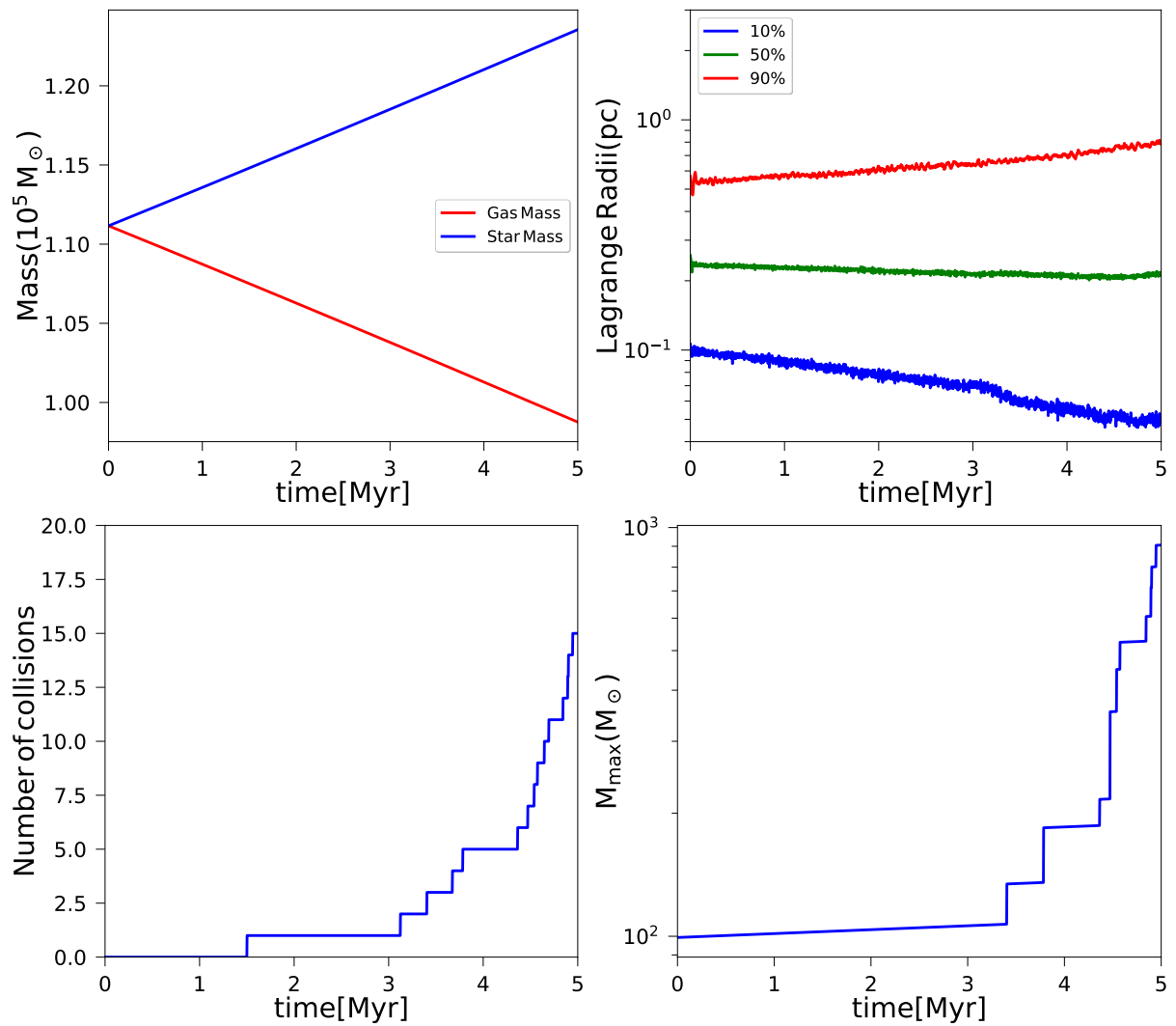
Figure 3.6: Same as in Figure 3.3, but assuming instead Eddington accretion.
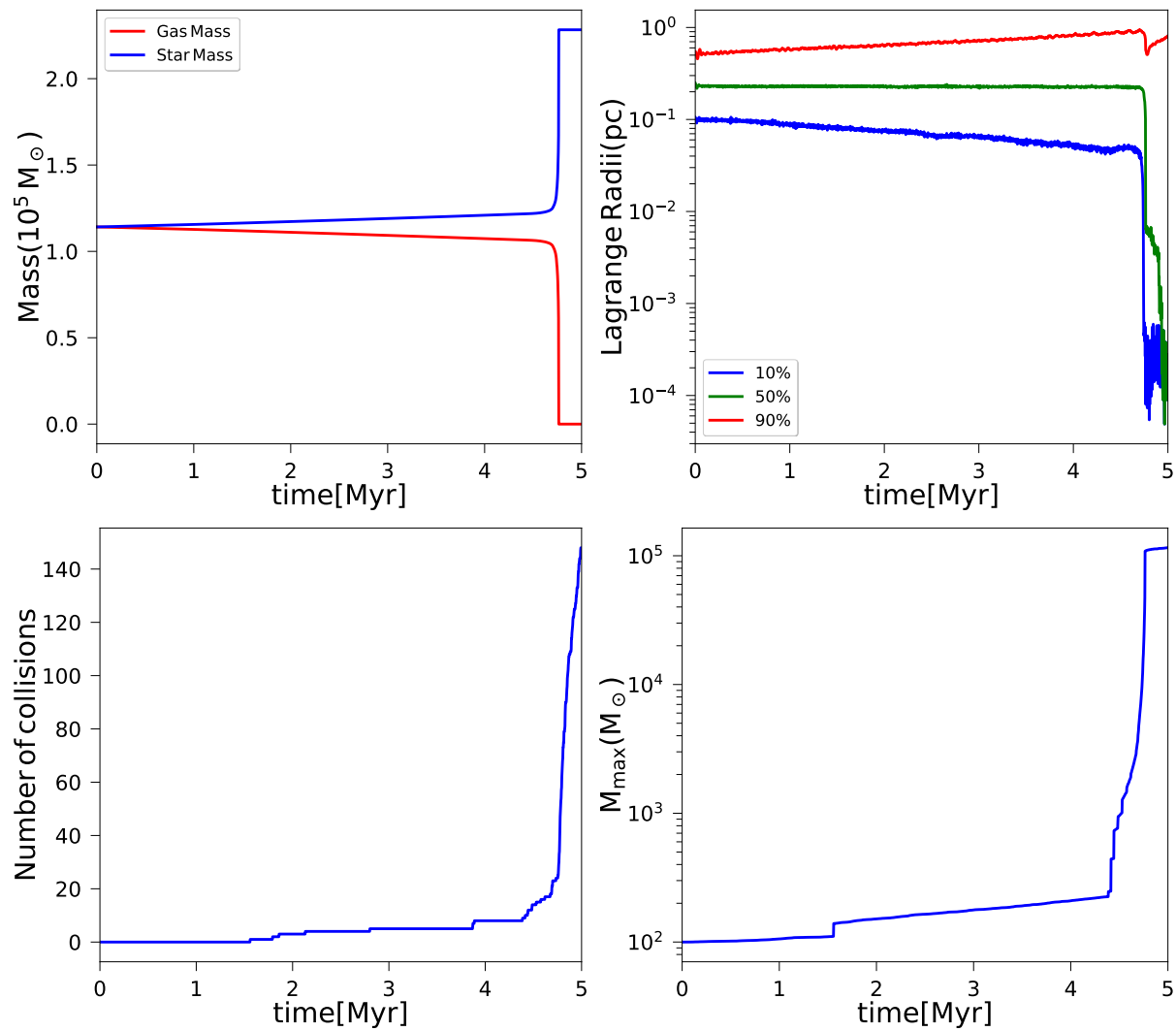
Figure 3.7: Same as in Figure 3.3, but assuming instead Bondi accretion.
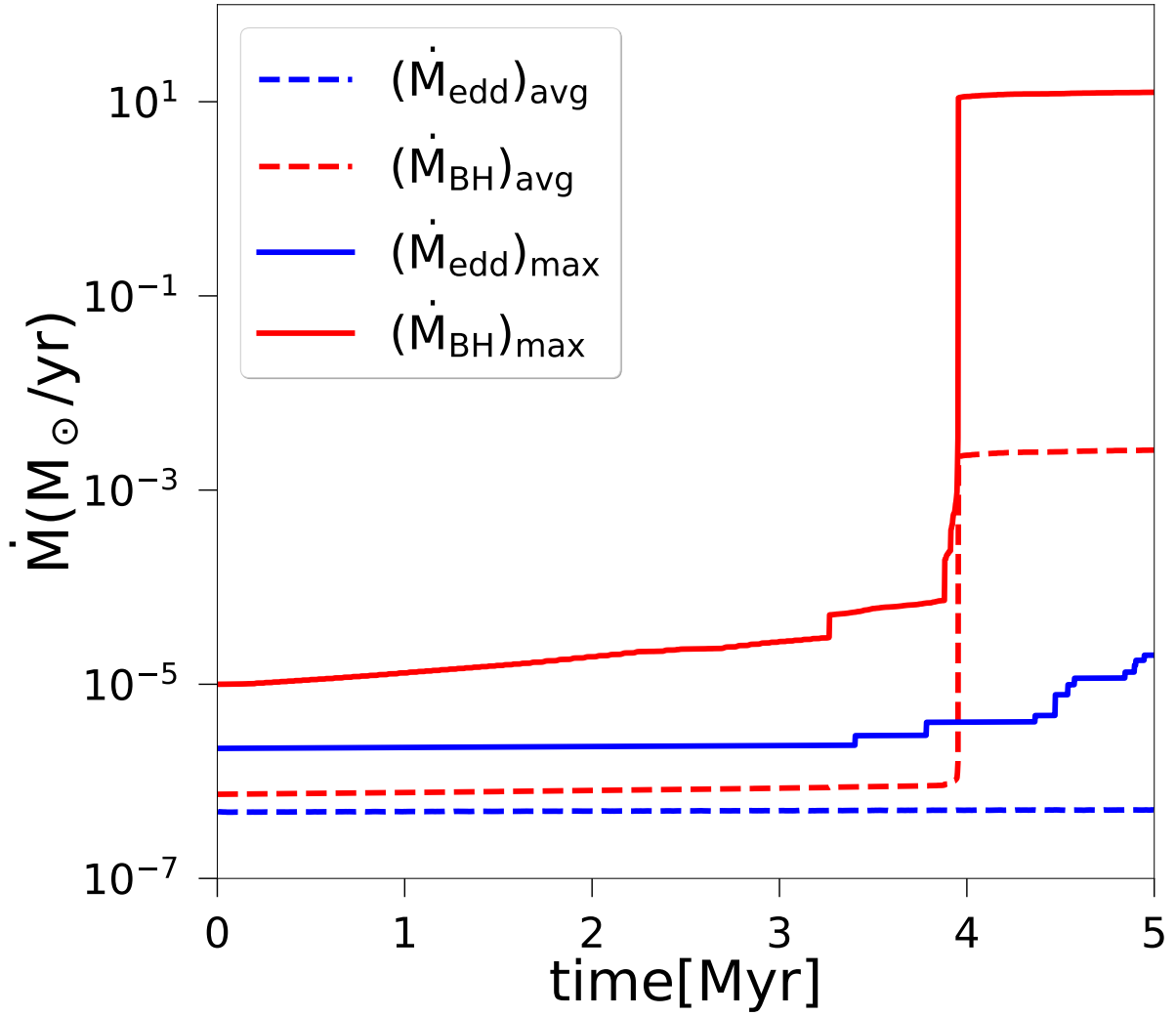
Figure 3.8: Average accretion rate and maximum accretion rate in the cluster as a function of time, for the models assuming Eddington or Bondi accretion. We assume an IMF with stellar masses of 10-100 $M_\odot$.

timescale. The accretion timescale of the MMO is given by

$$t_{\mathrm{acc}} = \frac{M_{\max}}{\dot{m}}, \tag{3.23}$$

with $M_{\max}$ being the mass of the MMO and $\dot{m}$ is given by constant, Eddington and Bondi accretion rates.

We plot the theoretically expected ratio of these timescales in Fig. 3.9, considering the cases of a constant accretion rate of $10^{-5}\,\mathrm{M_\odot yr^{-1}}$, as well as Eddington accretion and Bondi accretion, as a function of the mass of the MMO. The color bar represents different ratios of gas to cluster mass. We consider $m_A = 20\,\mathrm{M_\odot}$, $\bar{m} = 22\,\mathrm{M_\odot}$ and $N_B = 5000$ (motivated from the initial conditions of our simulations). The radii R_A and R_B are calculated using eq. 3.6 and 3.7.

In the considered parameter space covering several orders of magnitude, the ratio $\frac{t_{\mathrm{coll}}}{t_{\mathrm{acc}}} \gg 1$, suggesting that accretion dominates over collisions in this regime. For $t_{\mathrm{coll}} \approx t_{\mathrm{acc}}$, we would require extremely compact clusters with $R_{\mathrm{cl}} \ll 0.1$ pc or the mass of the MMO would have to be much less than $100\,\mathrm{M_\odot}$. So in principle a situation can occur for which collisions will dominate over accretion, but it will be for a small part of the parameter space. We find a very similar result if we plot the ratio of these timescales directly from the conditions obtained in the simulations, which we plot in Fig. 3.10. Since our simulations have an initial range of masses between 10-100 $\mathrm{M_\odot}$ we assumed the most massive particle to be the type A and consider the rest of the particles as type B. The ratio of the timescales is again considerably larger than 1.

In principle this suggests that accretion should be more important than collisions for the clusters considered here. However, it is important to note from the results in section 3.3.1 that only a moderate number of collisions occurs for an accretion rate of accretion rate $\sim 10^{-6}\,\mathrm{M_\odot yr^{-1}}$ (and we checked that no collisions occur for a low accretion rate $\sim 2 \times 10^{-7}\,\mathrm{M_\odot yr^{-1}}$), but a relevant number of collisions occurs for a high accretion rate of $\sim 10^{-5}\,\mathrm{M_\odot yr^{-1}}$ or $10^{-4}\,\mathrm{M_\odot yr^{-1}}$. It is thus important to realize that the collision probability is affected by accretion, an effect which is not incorporated into the formula above for the collision timescale. This is compatible with the work of Davis et al. (2010), who have shown that the number of stellar collisions should be $\propto N^{5/3}\dot{M}^{2/3}$, where in their work $\dot{M}$ is the accretion rate onto the cluster, which is however reflected in accretion onto individual stars.

We also emphasize that collision timescale in Eq. 3.21 is for a single object. To obtain the timescale for the collision of any two objects in the cluster, the collision timescale adopted here should be multiplied with $2/(N-1)$ (Leigh et al., 2017b), bringing both timescales much closer together, or allowing collision timescale to be shorter for part of the parameter space. Hence, stellar collisions will be strongly favoured in clusters with high N such as in all our models. However, it is important to note that this collision probability was computed using a simplified model where all the stars in the cluster are of the same mass, in contrast to a realistic IMF adopted in our models. The presence of an IMF will lead to mass segregation as massive stars tend to sink to the core through dynamical friction where they may eventually decouple from the remainder of the cluster. This is also known as "Spitzer Instability" (Spitzer, 1969). The Spitzer instability will lead to a shorter relaxation time in the core and an increased collisional cross section, both of which will increase the collision rate. What we can derive from the considerations in this subsection, is that collisions overall will be relevant and frequently occur, which may in turn may even accelerate the accretion process, due to the mass dependence in

the Eddington and Bondi rate, and in particular early collisions may then determine the point when accretion starts to become more efficient.

3.3.4 Effect of the IMF

To understand how the results so far depend on additional assumptions, we explore how the results for the different accretion rates change using different assumptions regarding the IMF. We generally assume a Salpeter IMF with a lower-mass cutoff of $10\,M_\odot$, and vary the upper mass limit in the initial stellar mass distribution, considering 100, 120 and $150\,M_\odot$. In the first case with a constant accretion rate of $\dot{m} = 10^{-5}\,M_\odot\,\mathrm{yr}^{-1}$, Fig. 3.11 shows that such a variation has only a very moderate impact. The intrinsic scatter, when varying the initial conditions, means that the evolution at late times basically cannot be uniquely distinguished between the different cases, but it is likely that overlap in the parameter space of the results will occur when considering a larger set of initial conditions.

For the case of Eddington accretion, we see very clearly that the MMO in our simulations grows more rapidly where the IMF extends to a higher mass. This is expected due to the dependence of the Eddington accretion rate on the mass of the accretor, accelerating both the accretion of the MMO as well as the conversion of gas mass into stellar mass in general. We note that the first collisions tend to occur earlier in the case of a larger initial mass, and we find a difference in the final mass by about a factor of 3 comparing the most extreme cases. In case of mass-dependent accretion recipes, the growth of the MMO is thus further enhanced if the initial IMF already extends to higher masses.

Finally, in the case of Bondi accretion, the dependence on the initial mass and the resulting behavior is even more extreme. Due to the steep dependence of the rate on the accretor mass, the central mass remains low for extended periods of time, then suddenly accelerates in a run-away fashion, as seen in the previous subsection. When the upper-mass cutoff of the stellar mass is higher, this rapid acceleration occurs earlier. For the cases considered here, a final mass of $10^5\,M_\odot$ is reached in all cases, only at different times. We note again that the latter corresponds to a rather extreme assumption, so this part of the results needs to be regarded with caution. It is interesting to note that a more moderate increase of the mass of the MMO is found at earlier times when the Bondi accretion rate is low and a larger higher-mass cutoff in the IMF will favor this growth. Similar results were also found by Leigh et al. (2013a).

3.3.5 Dependence on cluster radius

To also understand how the different accretion mechanisms operate for different central densities of the cluster, we vary R_{cl} and thus the central density of the cluster. Specifically, R_{cl} has been varied between 0.3 and 5 pc, leading to an evolution as shown in Fig. 3.12 for the different scenarios. Depending on R_{cl}, the initial central stellar densities range from $10^5\,M_\odot\,\mathrm{pc}^{-3}$ up to $10^9\,M_\odot\,\mathrm{pc}^{-3}$, and due to subsequent evolution and depending on accretion scenarios, even core densities of $10^8\,M_\odot\,\mathrm{pc}^{-3}$ to $10^{12}\,M_\odot\,\mathrm{pc}^{-3}$ can be reached.

For a constant accretion rate of $\dot{m} = 10^{-5}\,M_\odot\,\mathrm{yr}^{-1}$, we find a considerable dependence on R_{cl}, with collisions in principle occurring in all cases, but their number depending significantly on the size of the cluster (see table 3.1). For a large cluster with $R_{\mathrm{cl}} = 5$ pc, the MMO still grows to about $2000\,M_\odot$, with most of the growth occurring after 3.5 Myr due to the collisions. Even
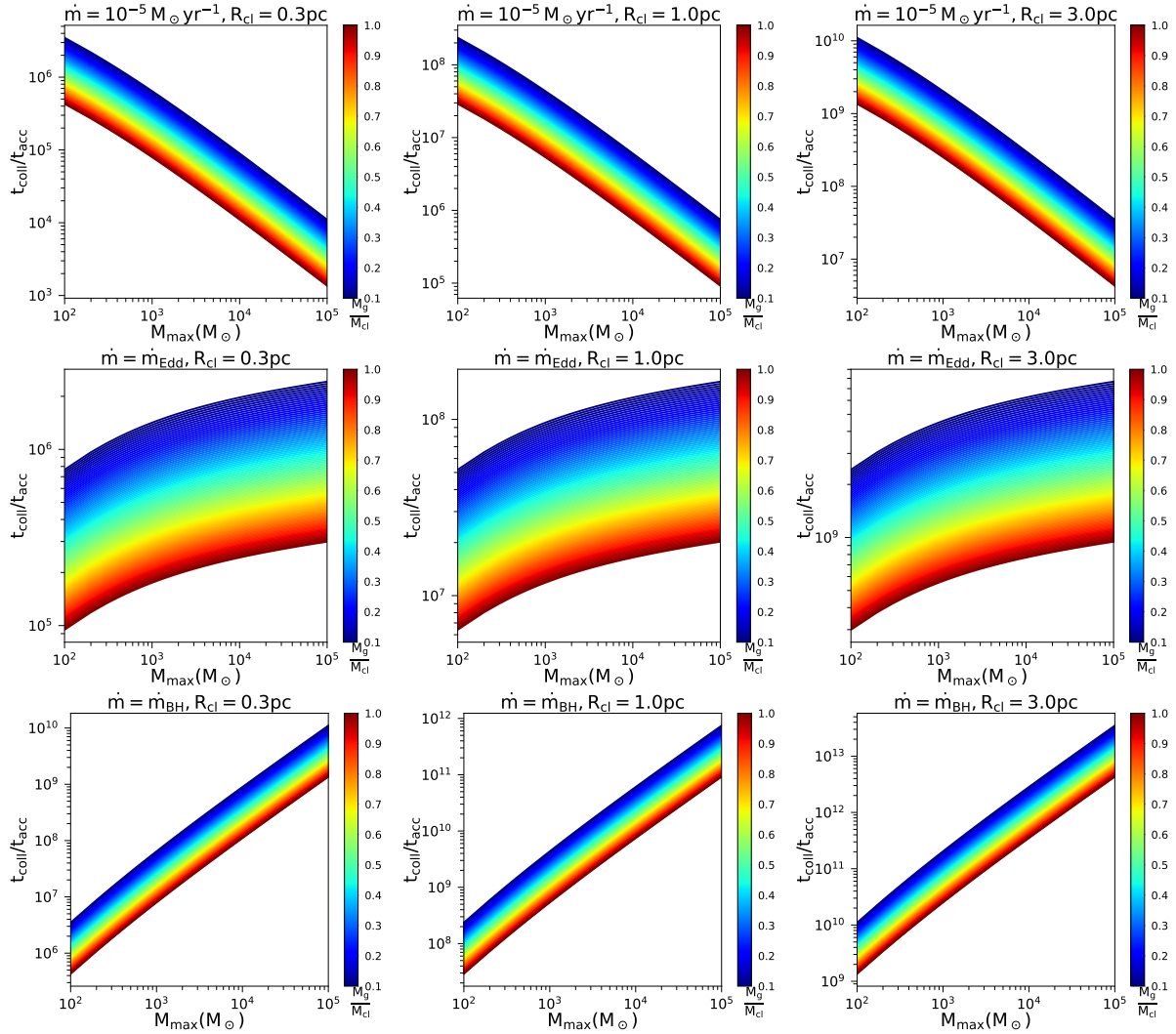
Figure 3.9: The ratio of collision over accretion timescales, t_{coll}/t_{acc}, as a function of stellar mass for the case of a constant accretion rate of $10^{-5}\,M_\odot yr^{-1}$ (top panel), Eddington accretion rate (mid panel) and Bondi accretion rate (bottom panel). We show the results for clusters sizes of 0.3 pc (left), 1 pc (middle) and 3 pc (right), assuming different ratios of gas to cluster mass. The expected ratio $t_{coll}/t_{acc} \gg 1$, suggesting that accretion dominates over collisions in this regime.
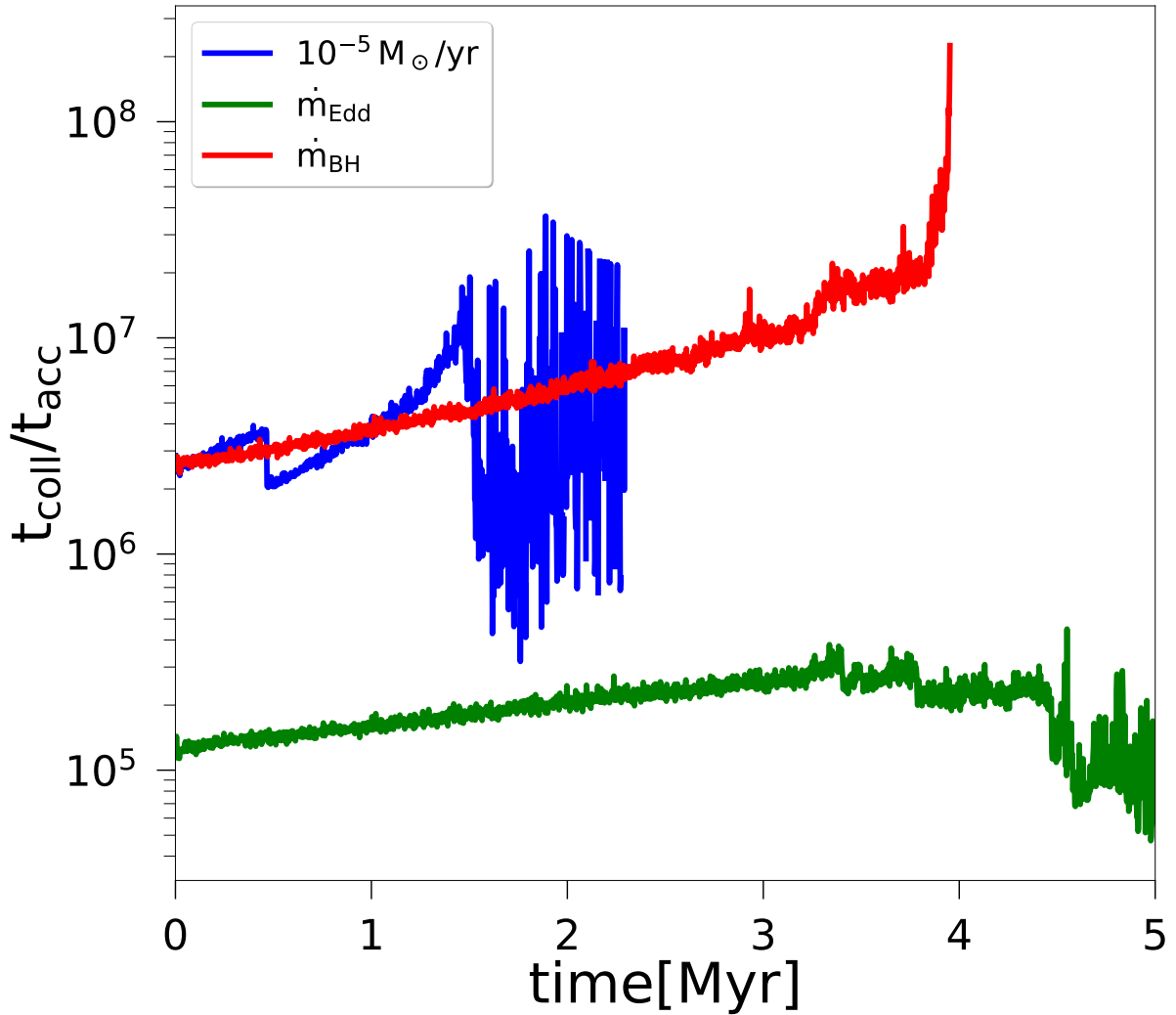
Figure 3.10: The ratio t_{coll}/t_{acc}, evaluated from simulations with N=5000, $M_{cl} = M_g = 10^5\,M_\odot$, $R_{cl} = R_g = 1$pc as initial conditions, plotted for a constant accretion rate of $10^{-5}\,M_\odot yr^{-1}$ (blue line), Eddington accretion rate (green line) and Bondi accretion rate (green line). The ratio $t_{coll}/t_{acc} \gg 1$, showing that accretion dominates over collisions in the simulations.
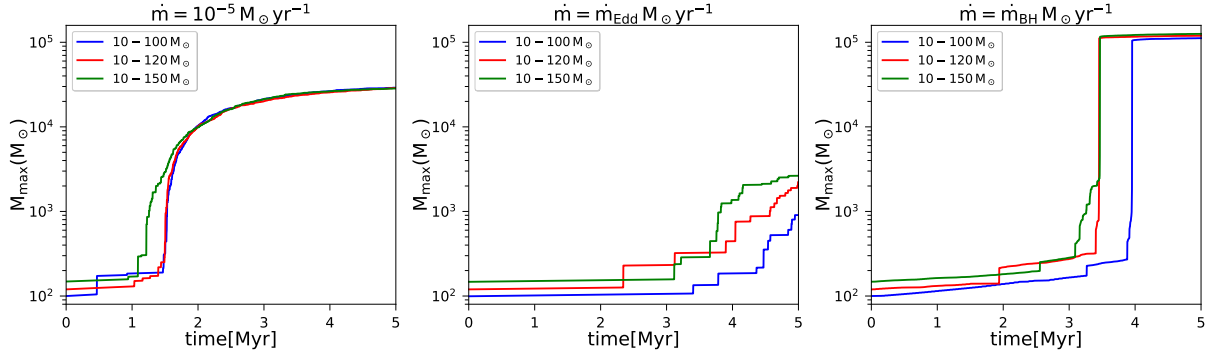
Figure 3.11: Effect of varying the upper-mass end of the IMF on the mass of the MMO. The left panel shows the time evolution in case of a constant accretion rate of $\dot{m} = 10^{-5}\,\mathrm{M_\odot yr^{-1}}$, the mid panel for the case of Eddington accretion, and the right panel for the case of Bondi accretion.

for $R_{\mathrm{cl}} = 2$ pc, the growth starts considerably earlier, with a steep rise in the mass of the MMO after 2 Myr, and reaching a final mass of more than $10^4\,\mathrm{M_\odot}$. For the most compact cluster with $R_{\mathrm{cl}} = 0.3$ pc, rapid growth starts after 0.5 Myr and the final mass reaches about $5 \times 10^4\,\mathrm{M_\odot}$. The growth of the central object in these cases is mostly due to collisions, driven by the increase of the central density in the cluster, driven by contraction to the increase in mass. The mass of the MMO correlates well with the compactness of the cluster in the cases considered here.

In the Eddington accretion scenario where at least initially the accretion rate tends to be lower, the evolution depends more strongly on the size of the cluster, and for $R_{\mathrm{cl}} = 2$ pc or more, no significant growth of the mass of the MMO is found. In the case of $R_{\mathrm{cl}} = 1$ pc, the central mass starts growing after about 3.5 Myr, reaching about $800\,\mathrm{M_\odot}$. In the case of more compact clusters, the evolution starts earlier, even within the first Myr in case of a 0.3 pc cluster, with the MMO reaching a final mass of about $2 \times 10^4\,\mathrm{M_\odot}$. The growth overall is less steep in this scenario, as the Eddington accretion rate is initially lower, thus leading to a more gradual increase in total stellar mass and the contraction of the cluster occurs more gradually. Again, the mass of the MMO correlates well with the compactness of the cluster for these configurations.

In the case of Bondi accretion, the behavior becomes somewhat more extreme. It is not directly related to the initial R_{cl}, but depends more on when the first collision happens to occur, thereby producing an object of larger mass, to which the Bondi rate reacts very sensitively. The occurrence of this first collision will statistically vary for different cluster sizes, and in fact Fig. 3.12 shows no clear dependence of the overall evolution on the R_{cl}. In all cases, the evolution initially occurs very slowly, though at different times for the different simulations, a sudden acceleration occurs once the Bondi rate becomes sufficiently large. The final mass is always about $10^5\,\mathrm{M_\odot}$, forming in between 2 and 5 Myr for all cases considered here. In this case, the evolution is mostly driven by accretion, with collisions not playing a relevant role.

In the cases considered here, the cluster size has the lowest impact in the case of the Bondi accretion rate, due to the very steep dependence on the mass of the MMO in this scenario. For more moderate mass dependencies, the cluster size is however found to be highly relevant, and can strongly affect the resulting evolution. Understanding the physical mechanism of accretion along with its dependence of mass will thus be crucial to determine the relevance of this
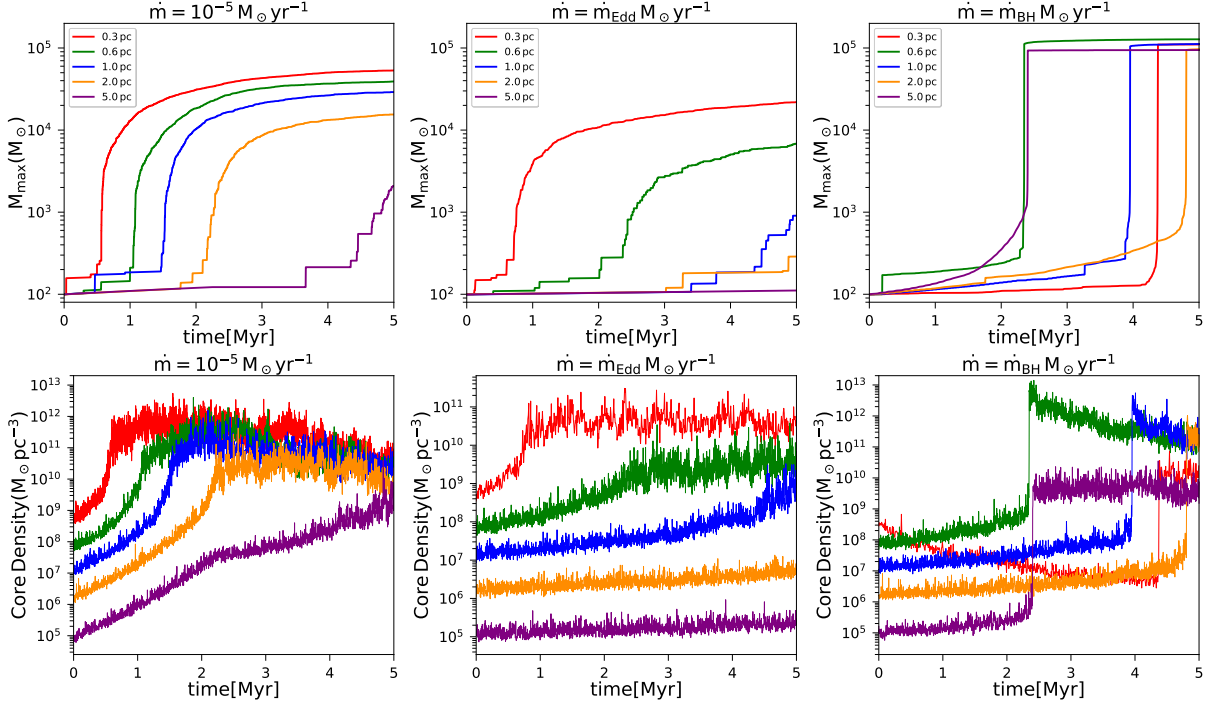
Figure 3.12: Effect of R_{cl} (or the density) on the mass of the MMO. The left panel shows the time evolution in case of a constant accretion rate of $\dot{m} = 10^{-5}$ $M_\odot yr^{-1}$, the mid panel for the case of Eddington accretion, and the right panel for the case of Bondi accretion. In the bottom panel we show the evolution of the core density as a function of time, the color represents the same as the top panel. We adopt here our reference IMF between 10 and $100 \, M_\odot$.

parameter. While a more compact cluster in principle shortens the timescale for collisions, we also note that the latter is not necessarily the dominant effect. Particularly in the case of Bondi accretion, early collisions in the cluster will rather accelerate the accretion process due to the steep dependence on mass, thereby leading to an even more rapid growth via accretion. For the Eddington scenario and in case of a constant accretion rate, the shortening of collision timescale in comparison is more relevant, and in these cases there is a clear correlation between having a more compact cluster and a more massive central object.

3.3.6 Effect of mass loss during collisions

Finally, the possible effect of mass loss during collisions is explored for different scenarios and the results are shown in Fig. 3.13, considering different accretion scenarios, all for our reference IMF with masses between $10 - 100 \, M_\odot$.

The mass loss during collisions is particularly relevant in the case of a constant accretion rate, where we consider the reference case of $\dot{m} = 10^{-5} \, M_\odot yr^{-1}$. Both in the cases without mass loss as well as in K15, we find almost the same final mass of the MMO of about $3 \times 10^4 \, M_\odot$. This shows that most of the collisions occur at very high mass ratios, where K15 suggests the mass loss to have little impact. However, if this assumption is not correct or rather an underestimate, our calculation with a mass loss fraction of 3% shows that the final mass could be considerably
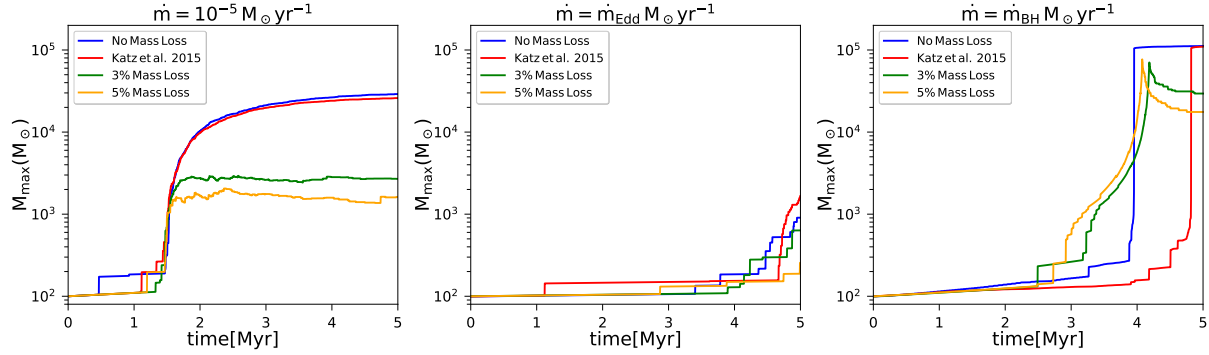
Figure 3.13: Effect of mass loss due to collisions on the mass of the MMO. The left panel shows the time evolution in case of a constant accretion rate of $\dot{m} = 10^{-5}$ $M_\odot yr^{-1}$, the mid panel for the case of Eddington accretion, and the right panel for the case of Bondi accretion. The blue line, the red line and the green line represent the cases of no mass loss, mass loss according to Eq. 3.20, a constant mass loss fraction of 3% and a constant mass loss fraction of 5%, respectively. We adopt here our reference IMF between 10 and $100 \, M_\odot$.

reduced by roughly a factor of 10, consistent with similar results by Alister Seguel et al. (2020) for primordial protoclusters. The reason is that in this case, particularly for high mass ratios during the collisions, the mass loss can become comparable to the mass that is added during the collision, or potentially even larger, and then compensate for part of the accretion. The final mass is similar but a bit further reduced in case of a 5% mass loss fraction, reflecting the flattening that was also found by Alister Seguel et al. (2020) when plotting final masses as a function of the mass loss fraction.

In the case of Eddington accretion, we first have to note that here the results depend somewhat sensitively on when the first collision occurs, as subsequently the accretion rate will be enhanced, thereby providing a somewhat statistical element that depends on the nonlinear evolution. For this reason, the simulation with the K15 obtains the highest mass of a few times $10^3 \, M_\odot$, a very similar value as the simulation with no mass loss. In case of a 3% mass loss fraction, the final mass is reduced to about $600 \, M_\odot$, and about $250 \, M_\odot$ for a 5% fraction. The latter reflects roughly the expected trend regarding the final masses, with some super-imposed scatter due to the time of when the first collision occurs in the models.

Finally, in the case of Bondi accretion, in principle a similar behavior is found, only with an even steeper increase of the final masses at late times, and a more flat evolution initially, as also found before in our exploration of Bondi accretion. The highest final mass is attained here in the case with no mass loss, with about $10^5 \, M_\odot$ after about 4 Myr. Using K15, a very similar final mass is obtained after almost 5 Myr. The curves with 3% and 5% mass loss fractions behave similarly, starting to increase more significantly after about 3 Myr, reaching a maximum close to $10^5 \, M_\odot$ after about 4 Myr, while subsequently showing a decrease of their mass once the gas reservoir is exhausted and accretion stops, while mass loss still continues due to collisions. The final mass after 5 Myr is thus between $2 - 4 \times 10^4 \, M_\odot$ in these cases.

Summary of the results

$\dot{m}_{\mathrm{acc}}$ ($M_\odot \mathrm{yr}^{-1}$)	ΔM ($M_\odot$)	IMF($M_\odot$)	$M_{\mathrm{cl}} = M_{\mathrm{g}}$ ($M_\odot$)	$R_{\mathrm{cl}} = R_{\mathrm{g}}$ (pc)	N	N_{coll}	$M_{\max}$
10^{-4}	None	10-100	1.10×10^5	1.0	5000	563	3.16×10^4
10^{-5}	None	10-100	1.10×10^5	1.0	5000	490	2.90×10^4
10^{-6}	None	10-100	1.10×10^5	1.0	5000	20	1.29×10^4
10^{-5}	None	10-120	1.14×10^5	1.0	5000	440	2.88×10^4
10^{-5}	None	10-150	1.22×10^5	1.0	5000	404	2.84×10^4
$\dot{m}_{\mathrm{BH}}$	None	10-100	1.10×10^5	1.0	5000	153	1.12×10^5
$\dot{m}_{\mathrm{BH}}$	None	10-120	1.14×10^5	1.0	5000	152	1.19×10^5
$\dot{m}_{\mathrm{BH}}$	None	10-150	1.22×10^5	1.0	5000	178	1.26×10^5
$\dot{m}_{\mathrm{Edd}}$	None	10-100	1.10×10^5	1.0	5000	15	9.06×10^2
$\dot{m}_{\mathrm{Edd}}$	None	10-120	1.14×10^5	1.0	5000	31	2.23×10^3
$\dot{m}_{\mathrm{Edd}}$	None	10-150	1.22×10^5	1.0	5000	23	2.64×10^3
10^{-5}	None	10-100	1.10×10^5	0.3	5000	1018	5.33×10^4
10^{-5}	None	10-100	1.10×10^5	0.6	5000	691	3.91×10^4
10^{-5}	None	10-100	1.10×10^5	2.0	5000	246	1.55×10^4
10^{-5}	None	10-100	1.10×10^5	5.0	5000	28	2.08×10^4
$\dot{m}_{\mathrm{BH}}$	None	10-100	1.10×10^5	0.3	5000	454	1.10×10^5
$\dot{m}_{\mathrm{BH}}$	None	10-100	1.10×10^5	0.6	5000	426	1.28×10^5
$\dot{m}_{\mathrm{BH}}$	None	10-100	1.10×10^5	2.0	5000	28	9.68×10^4
$\dot{m}_{\mathrm{BH}}$	None	10-100	1.10×10^5	5.0	5000	24	9.44×10^4
$\dot{m}_{\mathrm{Edd}}$	None	10-100	1.10×10^5	0.3	5000	409	2.19×10^4
$\dot{m}_{\mathrm{Edd}}$	None	10-100	1.10×10^5	0.6	5000	107	6.83×10^3
$\dot{m}_{\mathrm{Edd}}$	None	10-100	1.10×10^5	2.0	5000	12	2.88×10^2
$\dot{m}_{\mathrm{Edd}}$	None	10-100	1.10×10^5	5.0	5000	0	1.11×10^2
10^{-5}	K15	10-100	1.10×10^5	0.3	5000	471	2.59×10^4
10^{-5}	0.3%	10-100	1.10×10^5	0.6	5000	272	2.69×10^4
10^{-5}	0.5%	10-100	1.10×10^5	2.0	5000	234	1.62×10^4
$\dot{m}_{\mathrm{BH}}$	K15	10-100	1.10×10^5	0.3	5000	86	1.10×10^5
$\dot{m}_{\mathrm{BH}}$	0.3%	10-100	1.10×10^5	0.6	5000	79	2.95×10^4
$\dot{m}_{\mathrm{BH}}$	0.5%	10-100	1.10×10^5	2.0	5000	76	1.76×10^4
$\dot{m}_{\mathrm{Edd}}$	K15	10-100	1.10×10^5	0.3	5000	33	1.68×10^3
$\dot{m}_{\mathrm{Edd}}$	0.3%	10-100	1.10×10^5	0.6	5000	16	6.34×10^2
$\dot{m}_{\mathrm{Edd}}$	0.5%	10-100	1.10×10^5	2.0	5000	11	2.56×10^2

Table 3.1: $\dot{m}_{\mathrm{acc}}$ ($M_\odot \mathrm{yr}^{-1}$): accretion model, ΔM ($M_\odot$): Mass loss due to collision, IMF($M_\odot$): Initial Mass Function used in the models, $M_{\mathrm{cl}} = M_{\mathrm{g}}$ ($M_\odot$):Initial mass of the cluster (= mass of the gas), $R_{\mathrm{cl}} = R_{\mathrm{g}}$ (pc): Initial radius of the cluster (=radius of the gas), N:Initial number of particles, N_{coll}: Total number of collisions, $M_{\max}$: Final mass of the MMO in the cluster

3.3.7   Caveats

One of the main caveats of this work is that the simulation setup we employed here is highly idealised and not based on cosmological initial conditions, and also not solving the hydrodynamic equations. Hence, the processes in real cosmological systems could be different if there are differences in the structure, or if the accretion recipes that we explored here do not represent the type of accretion that will occur in these halos. The main goal of this work was to build a simplified model that allows us to study a large part of the parameter space, and to study the evolution of the cluster in that parameter space over timescales of a few Myr, which would not be possible if we were to include the full hydrodynamics. If we were to do so, then in addition to the the cooling, the chemistry of the gas and feedback processes due to the stars would need to be modeled in more detail. Recent studies by Kroupa et al. (2020) and Natarajan (2021) discuss in more detail about gas accretion onto black holes inside NSCs.

The results of this work motivate us to run more simulations and will be able to guide future work to explore parts of the parameter space that can be regarded as particularly promising. It will be particularly important to understand which of the accretion recipes employed here, if any, provides an accurate prescription that will be consistent with results from real hydrodynamical simulations. We want to point out that sticking to only the first few Myr of evolution of the cluster minimizes concerns related to numerical issues i.e. if we were to re-run the simulations, we are confident that we would get the same results over the relevant timescales we consider. Over a longer timescale we would expect more divergence in the results of identical simulation setups. In addition, we note that other complicating factors such as mass loss due to stellar winds, stellar evolution, rotation etc. are currently not included in our simulations. Particularly, it is very uncertain how collisions affect stellar evolution, and the mass loss through winds for stars more massive than $1000 \, M_\odot$ is not well known. These provide very relevant uncertainties that need to be studied in more detail to provide reliable conclusions regarding collision-based formation mechanisms of SMBH seeds.

3.4   Summary and discussion

In this work, we explored possible formation scenarios of SMSs in low-metallicity NSCs where mass loss from winds should be minimized. We explored how the interaction of collisions and accretion affects the formation of a central massive object for different physically motivated accretion scenarios: considering accretion rates that are constant in space and time, the Eddington accretion rate and the Bondi accretion rate.

Our fiducial model consists of a cluster with $N = 5000$, $M_{cl} = M_g = 1.12 \times 10^5 \, M_\odot$, $R_{cl} = R_g = 1$ pc, assuming a stellar mass distribution with Salpeter IMF with mass range $10 - 100 \, M_\odot$. Then we studied different accretion scenarios and also the effect of varying different parameters e.g. the upper mass limit of the Salpeter IMF, the central densities of the cluster and the inclusion of mass loss due to collisions on the final mass of the MMO in the cluster.

In the case of a constant accretion rate, the number of collisions depends significantly on the magnitude of the accretion rate. Our simulations show that central massive objects of $\sim 10^{3-5} \, M_\odot$ may form for accretion rates of $10^{-6} - 10^{-4} \, M_\odot \, yr^{-1}$. If the SMSs formed in this

way can directly collapse into seed black holes with similar mass, they can grow into the billion solar-mass black holes observed at $z \gtrsim 6$. In general, we find that the problem is quite sensitive to the initial conditions and the assumed recipe for the accretion, due to the highly chaotic and non-linear nature of the problem. The dominant factors that determine the mass growth are the mass of the MMO and the gas reservoir. Eddington accretion produces a central massive object of a few times $10^3 \, M_\odot$ in our reference scenario, while Bondi accretion robustly produces final masses $\sim 10^5 \, M_\odot$. It is however important to note that the Bondi scenario assumes $\dot{M}_{BH} \propto M_*^2$ and, as a result, the accretion rate remains low until a critical accretor mass is achieved leading to runaway growth. Only after a sufficiently long time of a few million years, the mass of the central object grows very rapidly. It is thus important to stress that such a scenario could only work if the gas is not previously expelled due to feedback, and if stellar evolution does not restrict the evolution to shorter timescales. In addition, Bondi accretion in general may be an extreme assumption, and we caution that some of the assumptions in our model will break down during the rapid phase of Bondi accretion due to the very rapid gas depletion.

We compared the collision and accretion timescales computed both analytically and from our simulations. Our calculations suggest that the collision timescale is much greater when calculated for the MMO. However, we emphasize that the collision rates we employed for this estimate did not account for the potentially enhanced collision probability in the presence of accretion, and our simulations show that the number of collisions increases for larger accretion rates. It further must be noted that when evaluating the timescale to have collisions between any two objects within the cluster, the collision timescale can become comparable to or shorter than accretion timescale. When considering the effects of an IMF, the "Spitzer Instability" (Spitzer, 1969) will lead to a shorter relaxation time in the core and an increased collisional cross section, both of which will increase the collision rate. We therefore expect collisions to play an important relevant role for the growth of the most massive object, consistent with what we find in the simulations as well. As the gas is depleted, collisions start to take over as the dominant mass growth mechanism for the MMO. This is only accelerated by the effects of cluster contraction induced by the presence of the gas reservoir and the dissipational effects it introduces to the distribution of relative particle velocities and masses (Leigh et al., 2014).

We explored the dependence of our results on the details of the IMF, considering Salpeter-type IMFs with different upper-mass limits. For the parameter space we explored, when considering constant accretion rates, the results were insensitive to such a change, while in the case of Eddington accretion, a larger upper-mass limit favours larger final masses. In the case of Bondi-accretion, the time of occurrence of the first collision is more important than an initially larger mass, particularly when the mass change due to a collision is larger than the mass change due to a variation of the upper mass cutoff of the IMF.

We further explored the dependence on the central density of the cluster by varying its radius and keeping the total cluster mass constant. For models with constant accretion rates, a more compact cluster significantly favors the formation of a supermassive star, with the final mass varying by more than an order of magnitude, for variations of cluster radii from 0.3 pc to 5 pc, as found by Giersz et al. (2015) for clusters without gas. A very similar dependence is found for Eddington accretion. It is interesting to note that a central massive object of mass $\sim 10^4 \, M_\odot$ could be formed for the case of Eddington accretion if the cluster has central radius $\sim 0.3 pc$ or less. In the Bondi case, the final mass is independent of the size of the cluster, but the required timescale to form the central massive object can vary substantially depending on

when the first collision occurs.

A very relevant uncertainty in these models is the mass loss during collisions. We compared simulations employing different mass loss recipes, considering the prescription by Katz et al. (2015), where the effect of the mass loss is effectively negligible, as it becomes very small when the mass ratio between the collision partners is high. On the other hand, we noticed that a fixed mass loss of 3% or 5% during collisions has a more pronounced effect and can change the final mass by around an order of magnitude, as the mass loss may then become comparable to the mass gained via the collisions. It will thus be important to understand the expected mass loss from stellar models, as noted in the case of completely primordial clusters by Alister Seguel et al. (2020).

As mentioned already in the introduction, the future will provide relevant opportunities for hopefully observing and probing the formation of very massive objects in the early Universe. From the work pursued here (and considering the results of other studies), we expect that SMSs formed via moderate accretion rates of less than $10^{-3}\,M_\odot\,yr^{-1}$, the SMSs will appear with blue colours and high luminosities, while for larger accretion rates or in the regime when collisions occur extremely frequently, the SMSs may be bloated up and preferentially show red colours. It needs to be determined via future observations if such a bimodality actually occurs, or if there is a predominant way in which these types of objects may actually be found.

Understanding the evolution of very massive metal poor stars in general will be important for further progress on the topic, as the lifetime of these stars can be a relevant limiting factor for the models. For a 20 $M_\odot$ single star it is roughly 5.6 Myr. Above $\sim 40\,M_\odot$, the lifetime is almost constant ($\sim 3.5 - 5$ Myr) (Hurley et al., 2000), while SMSs evolve over a timescale (given by eq. 3.9) ranging from 6 to 0.06 Myrs for SMS masses of $10^{3-5}\,M_\odot$. These results may significantly change in the presence of rotation (e.g. Leigh et al., 2016), which can act as a stabilizing factor and an accelerator for the collision rate by reducing the relative velocities between objects due to more correlated motions in rotating cluster environments. It may also affect the accretion rate of gas onto stars, when the first collisions actually occur and even the underlying stellar evolution of the collision products. We conclude that it will be important to investigate the stellar evolution of such objects in dynamical environments, considering accretion and/or collisions.

Acknowledgements

Data availability

The data underlying this article will be shared on reasonable request to the corresponding author.

Connection to next chapter

In the next chapter we study the importance of the additional effect of mass loss due to stellar winds on the final mass of the SMBH seeds formed by gas accretion and stellar collisions in the NSCs.

Bibliography

Abel T., Bryan G. L., Norman M. L., 2002, Science, 295, 93

Agarwal B., Khochfar S., Johnson J. L., Neistein E., Dalla Vecchia C., Livio M., 2012, MNRAS, 425, 2854

Agarwal B., Cullen F., Khochfar S., Ceverino D., Klessen R. S., 2019, MNRAS, 488, 3268

Alexander T., Bar-Or B., 2017, Nature Astronomy, 1, 0147

Alexander T., Natarajan P., 2014, Science, 345, 1330

Alister Seguel P. J., Schleicher D. R. G., Boekholt T. C. N., Fellhauer M., Klessen R. S., 2020, MNRAS, 493, 2352

Aykutalp A., Wise J. H., Spaans M., Meijerink R., 2014, ApJ, 797, 139

Bañados E., et al., 2018, Nature, 553, 473

Baraffe I., Heger A., Woosley S. E., 2001, ApJ, 550, 890

Barkana R., Loeb A., 2001, Phys. Rep., 349, 125

Barnes J., Hut P., 1986, Nature, 324, 446

Barrera C., Leigh N. W. C., Reinoso B., Stutz A. M., Schleicher D., 2020, arXiv e-prints, p. arXiv:2011.00021

Basu S., Das A., 2019, ApJ, 879, L3

Becerra F., Marinacci F., Bromm V., Hernquist L. E., 2018, MNRAS, 480, 5029

Begelman M. C., Volonteri M., 2017, MNRAS, 464, 1102

Begelman M. C., Volonteri M., Rees M. J., 2006, MNRAS, 370, 289

Bender R., et al., 2005a, ApJ, 631, 280

Bender R., et al., 2005b, ApJ, 631, 280

Boekholt T. C. N., Schleicher D. R. G., Fellhauer M., Klessen R. S., Reinoso B., Stutz A. M., Haemmerlé L., 2018, MNRAS, 476, 366

Böker T., Laine S., van der Marel R. P., Sarzi M., Rix H.-W., Ho L. C., Shields J. C., 2002, AJ, 123, 1389

Bond J. R., Arnett W. D., Carr B. J., 1984, ApJ, 280, 825

Bondi H., 1952, MNRAS, 112, 195

Bonnell I. A., Bate M. R., Clarke C. J., Pringle J. E., 2001, MNRAS, 323, 785

Bromm V., Loeb A., 2003, ApJ, 596, 34

Capelo P. R., Volonteri M., Dotti M., Bellovary J. M., Mayer L., Governato F., 2015, Monthly Notices of the Royal Astronomical Society, 447, 2123

Carollo C. M., Stiavelli M., de Zeeuw P. T., Mack J., 1997, AJ, 114, 2366

Chon S., Omukai K., 2020, MNRAS, 494, 2851

Chon S., Hosokawa T., Yoshida N., 2018, MNRAS, 475, 4104

Corbett Moran C., Grudić M. Y., Hopkins P. F., 2018, arXiv e-prints, p. arXiv:1803.06430

Dale J. E., Davies M. B., 2006, MNRAS, 366, 1424

Davies M. B., Miller M. C., Bellovary J. M., 2011, ApJ, 740, L42

Davis O., Clarke C. J., Freitag M., 2010, MNRAS, 407, 381

Dayal P., Rossi E. M., Shiralilou B., Piana O., Choudhury T. R., Volonteri M., 2019, MNRAS, 486, 2336

Demircan O., Kahraman G., 1991, Ap&SS, 181, 313

Devecchi B., Volonteri M., 2009, ApJ, 694, 302

Devecchi B., Volonteri M., Colpi M., Haardt F., 2010, MNRAS, 409, 1057

Dijkstra M., Ferrara A., Mesinger A., 2014, MNRAS, 442, 2036

Dopcke G., Glover S. C. O., Clark P. C., Klessen R. S., 2011, ApJ, 729, L3

Fan X., et al., 2001, AJ, 122, 2833

Ferrara A., Salvadori S., Yue B., Schleicher D., 2014, MNRAS, 443, 2410

Ferrarese L., et al., 2006, ApJ, 644, L21

Freese K., Ilie C., Spolyar D., Valluri M., Bodenheimer P., 2010, ApJ, 716, 1397

Freese K., Rindler-Daller T., Spolyar D., Valluri M., 2016, Reports on Progress in Physics, 79, 066902

Freitag M., 2008, in Beuther H., Linz H., Henning T., eds, Astronomical Society of the Pacific Conference Series Vol. 387, Massive Star Formation: Observations Confront Theory. p. 247 (arXiv:0711.4057)

Freitag M., Guerkan M. A., Rasio F. A., 2007, in St. -Louis N., Moffat A. F. J., eds, Astronomical Society of the Pacific Conference Series Vol. 367, Massive Stars in Interactive Binaries. p. 707 (arXiv:astro-ph/0410327)

Fujii M., Iwasawa M., Funato Y., Makino J., 2007, PASJ, 59, 1095

Gallerani S., Fan X., Maiolino R., Pacucci F., 2017, Publ. Astron. Soc. Australia, 34, e022

Georgiev I. Y., Böker T., Leigh N., Lützgendorf N., Neumayer N., 2016, MNRAS, 457, 2122

Giersz M., Leigh N., Hypki A., Lützgendorf N., Askar A., 2015, MNRAS, 454, 3150

Glebbeek E., Gaburov E., de Mink S. E., Pols O. R., Portegies Zwart S. F., 2009, A&A, 497, 255

Glebbeek E., Gaburov E., Portegies Zwart S., Pols O. R., 2013, MNRAS, 434, 3497

Graham A. W., Spitler L. R., 2009, MNRAS, 397, 2148

Greene J. E., Strader J., Ho L. C., 2020, ARA&A, 58, 257

Haemmerlé L., Woods T. E., Klessen R. S., Heger A., Whalen D. J., 2018, MNRAS, 474, 2757

Haemmerlé L., Mayer L., Klessen R. S., Hosokawa T., Madau P., Bromm V., 2020, Space Sci. Rev., 216, 48

Haiman Z., 2004, ApJ, 613, 36

Harwit M., 1988, Astrophysical Concepts

Haster C.-J., Antonini F., Kalogera V., Mandel I., 2016, ApJ, 832, 192

Hirano S., Hosokawa T., Yoshida N., Umeda H., Omukai K., Chiaki G., Yorke H. W., 2014, ApJ, 781, 60

Hirano S., Hosokawa T., Yoshida N., Kuiper R., 2017, Science, 357, 1375

Hosokawa T., Omukai K., Yorke H. W., 2012, ApJ, 756, 93

Hosokawa T., Yorke H. W., Inayoshi K., Omukai K., Yoshida N., 2013, ApJ, 778, 178

Hoyle F., Lyttleton R. A., 1939, Proceedings of the Cambridge Philosophical Society, 35, 592

Hoyle F., Lyttleton R. A., 1940a, Proceedings of the Cambridge Philosophical Society, 36, 325

Hoyle F., Lyttleton R. A., 1940b, Proceedings of the Cambridge Philosophical Society, 36, 424

Hurley J. R., Pols O. R., Tout C. A., 2000, MNRAS, 315, 543

Inayoshi K., Ostriker J. P., Haiman Z., Kuiper R., 2018a, MNRAS, 476, 1412

Inayoshi K., Li M., Haiman Z., 2018b, MNRAS, 479, 4017

Inayoshi K., Visbal E., Haiman Z., 2019, arXiv e-prints, p. arXiv:1911.05791

Ishii M., Ueno M., Kato M., 1999, PASJ, 51, 417

Janka H.-T., 2002, in Gilfanov M., Sunyeav R., Churazov E., eds, Lighthouses of the Universe: The Most Luminous Celestial Objects and Their Use for Cosmology. p. 357 (arXiv:astro-ph/0202028), doi:10.1007/10856495_56

Kaaz N., Antoni A., Ramirez-Ruiz E., 2019, ApJ, 876, 142

Katz H., 2019, Black hole formation in the first stellar clusters. pp 125–143, doi:10.1142/9789813227958_0007

Katz H., Sijacki D., Haehnelt M. G., 2015, MNRAS, 451, 2352

Kormendy J., Ho L. C., 2013, ARA&A, 51, 511

Kroupa P., Subr L., Jerabkova T., Wang L., 2020, MNRAS, 498, 5652

Latif M. A., Ferrara A., 2016, Publ. Astron. Soc. Australia, 33, e051

Latif M., Schleicher D., 2019, Formation of the First Black Holes, doi:10.1142/10652.

Latif M. A., Schleicher D. R. G., Schmidt W., Niemeyer J., 2013, MNRAS, 433, 1607

Latif M. A., Bovino S., Grassi T., Schleicher D. R. G., Spaans M., 2015, MNRAS, 446, 3163

Latif M. A., Omukai K., Habouzit M., Schleicher D. R. G., Volonteri M., 2016, ApJ, 823, 40

Latif M. A., Khochfar S., Whalen D., 2020, ApJ, 892, L4

Leigh N., Geller A. M., 2012, MNRAS, 425, 2369

Leigh N., Böker T., Knigge C., 2012, MNRAS, 424, 2130

Leigh N. W. C., Böker T., Maccarone T. J., Perets H. B., 2013a, MNRAS, 429, 2997

Leigh N., Sills A., Böker T., 2013b, MNRAS, 433, 1958

Leigh N. W. C., Mastrobuono-Battisti A., Perets H. B., Böker T., 2014, MNRAS, 441, 919

Leigh N. W. C., Georgiev I. Y., Böker T., Knigge C., den Brok M., 2015, MNRAS, 451, 859

Leigh N. W. C., Antonini F., Stone N. C., Shara M. M., Merritt D., 2016, MNRAS, 463, 1605

Leigh N. W. C., Geller A. M., Shara M. M., Garland J., Clees-Baron H., Ahmed A., 2017a, MNRAS, 471, 1830

Leigh N. W. C., Geller A. M., Shara M. M., Garland J., Clees-Baron H., Ahmed A., 2017b, MNRAS, 471, 1830

Luo Y., Shlosman I., Nagamine K., Fang T., 2020, MNRAS, 492, 4917

Lupi A., Colpi M., Devecchi B., Galanti G., Volonteri M., 2014, MNRAS, 442, 3616

Maccarone T. J., Zurek D. R., 2012, MNRAS, 423, 2

Madau P., Rees M. J., 2001, ApJ, 551, L27

Madau P., Haardt F., Dotti M., 2014, ApJ, 784, L38

Maeder A., Meynet G., 2000, ARA&A, 38, 143

Makino J., Aarseth S. J., 1992, PASJ, 44, 141

Martins F., Schaerer D., Haemmerlé L., Charbonnel C., 2020, A&A, 633, A9

Matsuoka Y., et al., 2018, PASJ, 70, S35

Matsuoka Y., et al., 2019, ApJ, 883, 183

Mayer L., Fiacconi D., Bonoli S., Quinn T., Roškar R., Shen S., Wadsley J., 2015, ApJ, 810, 51

Milosavljević M., Couch S. M., Bromm V., 2009, ApJ, 696, L146

Moeckel N., Clarke C. J., 2011, MNRAS, 410, 2799

Mortlock D. J., et al., 2011, Nature, 474, 616

Naoz S., Yoshida N., Gnedin N. Y., 2013, ApJ, 763, 27

Natarajan P., 2021, MNRAS, 501, 1413

Neumayer N., Seth A., Böker T., 2020, A&ARv, 28, 4

Nguyen D. D., et al., 2019, ApJ, 872, 104

Oh S. P., Haiman Z., 2002, ApJ, 569, 558

Omukai K., Palla F., 2003, ApJ, 589, 677

Omukai K., Schneider R., Haiman Z., 2008, ApJ, 686, 801

Onoue M., et al., 2019, ApJ, 880, 77

Pacucci F., Loeb A., 2020, ApJ, 895, 95

Pacucci F., Volonteri M., Ferrara A., 2015, MNRAS, 452, 1922

Pacucci F., Natarajan P., Volonteri M., Cappelluti N., Urry C. M., 2017, ApJ, 850, L42

Pelupessy F. I., van Elteren A., de Vries N., McMillan S. L. W., Drost N., Portegies Zwart S. F., 2013, A&A, 557, A84

Piana O., Dayal P., Volonteri M., Choudhury T. R., 2021, MNRAS, 500, 2146

Plummer H. C., 1911, MNRAS, 71, 460

Portegies Zwart S. F., McMillan S. L. W., 2002, ApJ, 576, 899

Portegies Zwart S., McMillan S., 2018, Astrophysical Recipes; The art of AMUSE, doi:10.1088/978-0-7503-1320-9.

Portegies Zwart S. F., Baumgardt H., Hut P., Makino J., McMillan S. L. W., 2004, Nature, 428, 724

Portegies Zwart S., et al., 2009, New Astron., 14, 369

Portegies Zwart S., McMillan S. L. W., van Elteren E., Pelupessy I., de Vries N., 2013, Computer Physics Communications, 184, 456

Regan J. A., Downes T. P., 2018, MNRAS, 478, 5037

Regan J. A., Visbal E., Wise J. H., Haiman Z., Johansson P. H., Bryan G. L., 2017, Nature Astronomy, 1, 0075

Regan J. A., Downes T. P., Volonteri M., Beckmann R., Lupi A., Trebitsch M., Dubois Y., 2019, MNRAS, 486, 3892

Regan J. A., Wise J. H., Woods T. E., Downes T. P., O'Shea B. W., Norman M. L., 2020a, arXiv e-prints, p. arXiv:2008.08090

Regan J. A., Haiman Z., Wise J. H., O'Shea B. W., Norman M. L., 2020b, The Open Journal of Astrophysics, 3, E9

Regan J. A., Wise J. H., O'Shea B. W., Norman M. L., 2020c, MNRAS, 492, 3021

Reinoso B., Schleicher D. R. G., Fellhauer M., Klessen R. S., Boekholt T. C. N., 2018, A&A, 614, A14

Rizzuto F. P., et al., 2021, MNRAS, 501, 5257

Rossa J., van der Marel R. P., Böker T., Gerssen J., Ho L. C., Rix H.-W., Shields J. C., Walcher C.-J., 2006, AJ, 132, 1074

Sakurai Y., Hosokawa T., Yoshida N., Yorke H. W., 2015, MNRAS, 452, 755

Sakurai Y., Yoshida N., Fujii M. S., Hirano S., 2017, MNRAS, 472, 1677

Sakurai Y., Yoshida N., Fujii M. S., 2019, MNRAS, 484, 4665

Salpeter E. E., 1955, ApJ, 121, 161

Schaller G., Schaerer D., Meynet G., Maeder A., 1992, A&AS, 96, 269

Schleicher D. R. G., Palla F., Ferrara A., Galli D., Latif M., 2013, A&A, 558, A59

Schleicher D. R. G., et al., 2019, Boletin de la Asociacion Argentina de Astronomia La Plata Argentina, 61, 234

Schödel R., Feldmeier A., Neumayer N., Meyer L., Yelda S., 2014, Classical and Quantum Gravity, 31, 244007

Scott N., Graham A. W., 2013, ApJ, 763, 76

Seth A., Agüeros M., Lee D., Basu-Zych A., 2008, ApJ, 678, 116

Seth A. C., Neumayer N., Böker T., 2020, in Bragaglia A., Davies M., Sills A., Vesperini E., eds, IAU Symposium Vol. 351, IAU Symposium. pp 13–18 (arXiv:1908.00022), doi:10.1017/S1743921319007117

Shapiro S. L., 2005, ApJ, 620, 59

Shen Y., et al., 2019, ApJ, 873, 35

Shlosman I., Choi J.-H., Begelman M. C., Nagamine K., 2016, MNRAS, 456, 500

Sills A., Adams T., Davies M. B., Bate M. R., 2002, MNRAS, 332, 49

Smith A., Bromm V., 2019, Contemporary Physics, 60, 111

Spitzer Lyman J., 1969, ApJ, 158, L139

Stacy A., Bromm V., Lee A. T., 2016, MNRAS, 462, 1307

Stone N. C., Küpper A. H. W., Ostriker J. P., 2017, MNRAS, 467, 4180

Sugimura K., Hosokawa T., Yajima H., Inayoshi K., Omukai K., 2018, MNRAS, 478, 3961

Surace M., et al., 2018, ApJ, 869, L39

Surace M., Zackrisson E., Whalen D. J., Hartwig T., Glover S. C. O., Woods T. E., Heger A., Glover S. C. O., 2019, MNRAS, 488, 3995

Tagawa H., Haiman Z., Kocsis B., 2020, ApJ, 892, 36

Takeo E., Inayoshi K., Mineshige S., 2020, arXiv e-prints, p. arXiv:2002.07187

Tanaka T., Haiman Z., 2009, ApJ, 696, 1798

Toyouchi D., Hosokawa T., Sugimura K., Nakatani R., Kuiper R., 2019, MNRAS, 483, 2031

Trac H., Sills A., Pen U.-L., 2007, MNRAS, 377, 997

Umeda H., Hosokawa T., Omukai K., Yoshida N., 2016, ApJ, 830, L34

Vesperini E., McMillan S. L. W., D'Ercole A., D'Antona F., 2010, ApJ, 713, L41

Vink J. S., de Koter A., Lamers H. J. G. L. M., 2001, A&A, 369, 574

Visbal E., Haiman Z., Bryan G. L., 2014, MNRAS, 445, 1056

Vito F., et al., 2019, A&A, 630, A118

Volonteri M., 2010, A&ARv, 18, 279

Volonteri M., 2012, Science, 337, 544

Volonteri M., Rees M. J., 2005, ApJ, 633, 624

Volonteri M., Rees M. J., 2006, ApJ, 650, 669

Volonteri M., Silk J., Dubus G., 2015, ApJ, 804, 148

Volonteri M., Bogdanović T., Dotti M., Colpi M., 2016, IAU Focus Meeting, 29B, 285

Vorobyov E. I., Basu S., 2006, ApJ, 650, 956

Vorobyov E. I., Basu S., 2015, ApJ, 805, 115

Wang R., et al., 2019, ApJ, 887, 40

Willott C. J., et al., 2010, AJ, 139, 906

Wise J. H., Regan J. A., O'Shea B. W., Norman M. L., Downes T. P., Xu H., 2019, Nature, 566, 85

Wolcott-Green J., Haiman Z., Bryan G. L., 2017, MNRAS, 469, 3329

Woods T. E., Heger A., Whalen D. J., Haemmerlé L., Klessen R. S., 2017, ApJ, 842, L6

Woods T. E., Heger A., Haemmerlé L., 2020, MNRAS, 494, 2236

Wu X.-B., et al., 2015, Nature, 518, 512

Yoshida N., Omukai K., Hernquist L., 2008, Science, 321, 669

Chapter 4

Effect of mass loss due to stellar winds on the formation of supermassive black hole seeds in dense nuclear star clusters

4.1 Introduction

Discovery of more than two hundred supermassive black holes (SMBHs) with masses $\gtrsim 10^9 \, M_\odot$ within the first ~ Gyr after the Big Bang (Fan et al., 2001; Willott et al., 2010; Mortlock et al., 2011; Wu et al., 2015; Bañados et al., 2018; Matsuoka et al., 2018; Wang et al., 2019; Shen et al., 2019; Matsuoka et al., 2019) have challenged our general understanding of black hole growth and formation. How these massive objects formed and grew over cosmic time is one of the biggest puzzles to solve in astrophysics (Smith & Bromm, 2019; Inayoshi et al., 2019; Latif & Schleicher, 2019). These SMBHs are created from 'seed' black holes that grow via gas accretion and mergers. The 'seed' black holes are categorized into two categories: (i) low mass seeds ($\lesssim 10^2 \, M_\odot$) and (ii) high mass seeds ($\sim 10^{4-6} \, M_\odot$). These seeds were formed at $z \sim 20 - 30$ (Barkana & Loeb, 2001), and then they rapidly grew to their final masses by gas accretion and mergers (Dayal et al., 2019; Pacucci & Loeb, 2020; Piana et al., 2021). Low mass seeds are formed from Pop III stellar remnants. However, it is really challenging to grow a SMBH of mass $\sim 10^9 \, M_\odot$ from a $10^2 \, M_\odot$ seed (Haiman & Loeb, 2001; Haiman, 2004; Volonteri, 2012; Woods et al., 2019). A potential solution could be super-Eddington accretion (Volonteri & Rees, 2005; Alexander & Natarajan, 2014; Madau et al., 2014; Volonteri et al., 2015; Pacucci et al., 2015, 2017; Begelman & Volonteri, 2017; Toyouchi et al., 2019; Takeo et al., 2020). However, radiation feedback from the seed black hole itself (Milosavljević et al., 2009; Sugimura et al., 2018; Regan et al., 2019) and inefficient gas angular momentum transfer (Inayoshi et al., 2018; Sugimura et al., 2018) could reduce the accretion flow into the black hole.

Another solution is to start the growth from a high mass seed (Bromm & Loeb, 2003). A possible scenario for the formation of these high mass seeds is the formation of massive black holes via direct collapse (Oh & Haiman, 2002; Bromm & Loeb, 2003; Begelman et al., 2006; Agarwal et al., 2012; Latif et al., 2013; Dijkstra et al., 2014; Ferrara et al., 2014; Basu & Das, 2019). A key requirement for this scenario is large inflow rate of $\sim 0.1 \, M_\odot \text{yr}^{-1}$ which

can be obtained easily in metal free halos (Agarwal et al., 2012; Latif et al., 2013; Shlosman et al., 2016; Regan & Downes, 2018; Becerra et al., 2018; Chon et al., 2018; Agarwal et al., 2019; Latif et al., 2020). In this scenario supermassive stars (SMSs) of masses $\sim 10^{4-5}$ M$_\odot$ are formed, which are massive enough to grow to 10^9 M$_\odot$ by $z \sim 7$. These SMSs collapse into seed BHs with minimal mass loss at the end of their lifetime (Umeda et al., 2016). These seed BHs are massive enough to grow up to $\sim 10^{9-10}$ M$_\odot$ SMBHs observed at $z \sim 7$ via Eddington accretion. The SMSs are often assumed to be formed in primordial halos with virial temperatures $T_{\rm vir} \sim 10^4$ K where the formation of molecular hydrogen is fully suppressed by strong external radiation from nearby galaxies (Omukai, 2001; Shang et al., 2010; Regan et al., 2014; Sugimura et al., 2014). The accretion flow into the cloud remains very high $(0.1 - 1\,{\rm M}_\odot {\rm yr}^{-1})$ due to the high gas temperature (Latif et al., 2013; Inayoshi & Haiman, 2014; Becerra et al., 2015). The surface of the protostars is substantially inflated due to the high accretion inflow and the effective temperature drops down to a few times 10^3 K (Hosokawa et al., 2012, 2013; Schleicher et al., 2013; Woods et al., 2017; Haemmerlé et al., 2018). The accretion flow can then continue without being significantly affected by the radiative feedback, which allows the protostars to grow into SMSs of masses 10^{4-5} M$_\odot$ within about ~ 1 Myr. In order to prevent the molecular H$_2$ formation, a very high background UV radiation flux is required (Latif et al., 2015; Wolcott-Green et al., 2017), which is very rare and optimistic but not impossible (Visbal et al., 2014; Dijkstra et al., 2014; Regan et al., 2017, 2020b). The formation of H$_2$ may lead to fragmentation that would suppress this process, as would the presence of metals via metal line cooling (Omukai et al., 2008; Dopcke et al., 2011; Latif et al., 2016; Corbett Moran et al., 2018; Chon & Omukai, 2020).

However, there are some scenarios in which the high velocity of the baryon gas can yield high accretion rates even in the presence of H$_2$ and/or low metallicity. High velocities due to collisions of protogalaxies (Inayoshi et al., 2015) or due to supersonic streaming motions of baryons relative to dark matter (Hirano et al., 2017) can lead to the required high mass infall rates. Massive nuclear inflows in gas-rich galaxy mergers (Mayer et al., 2015) have also been invoked. Chon & Omukai (2020) have further shown that even in just slightly metal enriched halos ($Z < 10^{-3}$ Z$_\odot$), where fragmentation takes place, the central massive stars could be fed by the accreting gas and grow into SMSs. Regan et al. (2020a) also have shown that SMSs could still be formed in atomic cooling haloes with higher metal enrichment ($Z > 10^{-3}$ Z$_\odot$) in the early universe due to inhomogeneous metal distribution. The high infall rate could be obtained by dynamical heating during rapid mass growth of low-mass halos in over-dense regions at high redshifts (Wise et al., 2019). There would still be an angular momentum barrier in all scenarios, though Sakurai et al. (2016) have shown that gravitational instability in a circumstellar disk can solve the angular momentum problem, leads to an episodic accretion scenario (Vorobyov et al., 2013; Vorobyov & Basu, 2015) and is consistent with the maintenance of the required low surface temperature of the accreting SMS. Nevertheless, the DCBH scenario is optimistic in that it relies on low fragmentation (Latif et al., 2013) and lack of disruptive feedback, e.g. x-ray feedback that could reduce the final mass of the collapsed object (Aykutalp et al., 2014).

Other scenarios for the formation of SMSs are based on runaway collisions of stars in dense stellar clusters (Portegies Zwart & McMillan, 2002; Portegies Zwart et al., 2004; Freitag et al., 2007; Freitag, 2008; Glebbeek et al., 2009; Moeckel & Clarke, 2011; Lupi et al., 2014; Katz et al., 2015; Sakurai et al., 2017; Boekholt et al., 2018; Reinoso et al., 2018; Schleicher et al., 2019; Gieles & Charbonnel, 2019; Alister Seguel et al., 2020; Das et al., 2020; Vergara et al.,

2021; Rizzuto et al., 2021; Vergara et al., 2021). Both Pop III star clusters (e.g. Boekholt et al., 2018; Reinoso et al., 2018; Schleicher et al., 2019; Alister Seguel et al., 2020) and nuclear star clusters (e.g. Katz et al., 2015; Das et al., 2020; Natarajan, 2021) are possible birthplaces of such SMSs. Many galaxies host massive NSCs (Carollo et al., 1997; Böker et al., 2002; Leigh et al., 2012, 2015; Georgiev et al., 2016) in their centre with masses of $\sim 10^{4-8}\,\mathrm{M_\odot}$. In many galaxies (typically with masses $10^9\,\mathrm{M_\odot} < M < 10^{11}\,\mathrm{M_\odot}$), NSCs and SMBHs co-exist (Seth et al., 2008; Graham & Spitler, 2009; Kormendy & Ho, 2013; Georgiev et al., 2016; Nguyen et al., 2019) including galaxies like our own (Schödel et al., 2014), as well as M31 (Bender et al., 2005a) and M32 (Bender et al., 2005b). Studies have also found correlations between both the SMBH mass and the NSC mass with the galaxy mass (Ferrarese et al., 2006; Rossa et al., 2006; Leigh et al., 2012; Scott & Graham, 2013; Seth et al., 2020). In lower-mass galaxies ($M \lesssim 10^{11}\,\mathrm{M_\odot}$) the NSC masses are proportional to the stellar mass of the spheroidal component. The most massive galaxies do not contain NSCs and their galactic nuclei are inhabited by SMBHs. It is therefore motivating to explore the NSCs as possible birthplaces of SMSs. There are different proposed scenarios for the formation of black hole seeds of masses $\sim 10^{3-5}\,\mathrm{M_\odot}$ in NSCs. Stone et al. (2017) have proposed that above a critical threshold stellar mass, the NSCs can serve as possible sites for the formation of intermediate mass black holes (IMBH) and/or a SMBH from stellar collisions, which could end up eventually as central BHs via runaway tidal encounters. They have shown that both tidal capture and tidal disruption will favour the growth of the remnant stellar mass black holes in the NSCs. In their study, they have argued that the stellar mass black holes can grow into an intermediate mass black hole (IMBH) or SMBH via three stages of runaway growth processes. At an early stage, the mass growth is driven by the unbound stars leading to supra-exponential growth. Once the BH reaches a mass $\sim 100\,\mathrm{M_\odot}$, the growth is driven by the feeding of bound stars. In this second stage, the growth of the black hole could be extremely rapid as well. At later times, the growth slows down once the seed IMBH/SMBH consumes the core of its host NSC. This type of runaway growth happens in dense nuclear stellar clusters which have been observed at lower redshifts (e.g. Georgiev et al., 2016). The growth of the BH through tidal captures/disruption of stars has also been proposed (Alexander & Bar-Or, 2017; Boekholt et al., 2018; Arca Sedda & Mastrobuono-Battisti, 2019). Another possible pathway for the formation and growth of massive BH seeds in NSCs is via stellar collisions and gas accretion (Devecchi & Volonteri, 2009; Devecchi et al., 2010; Davies et al., 2011; Das et al., 2020; Natarajan, 2021). A seed BH of mass $\sim 10^{4-5}\,\mathrm{M_\odot}$ could be formed in this case and grow to a $10^9\,\mathrm{M_\odot}$ SMBH at $z \sim 6-7$. King & Pringle (2006) and King et al. (2008) have shown that rapid BH growth is favoured by low values of the spin. Several studies have also proposed that NSCs are likely formed by the mergers of smaller clusters and these merging clusters may already host an IMBH which could be brought to the NSC during the merging event (Ebisuzaki et al., 2001; Kim et al., 2004; Portegies Zwart et al., 2006; Devecchi et al., 2012; Davies et al., 2019). It is also likely that multiple IMBHs are being fed to the NSCs (Ebisuzaki et al., 2001; Mastrobuono-Battisti et al., 2014), which will form binary IMBHs that could merge and emit gravitational waves (GW) (Tamfal et al., 2018; Rasskazov et al., 2020; Arca Sedda & Mastrobuono-Battisti, 2019; Wirth & Bekki, 2020). However, the GW recoil kick from the merging of the two IMBHs has to be less than the escape speed of the NSC in order to retain the merged IMBH within the NSC (Amaro-Seoane & Freitag, 2006; Gürkan et al., 2006; Amaro-Seoane et al., 2007; Arca Sedda & Mastrobuono-Battisti, 2019). A recent study by Askar et al. (2020) has shown that the SMBH will be ejected from the NSC

by the GW recoil kick if the mass ratio $\gtrsim 0.15$. This might explain why some massive galaxies contain an NSC but not an SMBH, e.g. M33.

Das et al. (2020) have shown that SMSs of masses $10^{3-5}\,\mathrm{M}_\odot$ could be formed in dense NSCs in low metallicity environments via runaway stellar collisions and gas accretion adopting different accretion scenarios. However, in high metallicity environments the mass loss due to stellar winds will play an important role in the formation and growth of the SMSs in the NSCs. Glebbeek et al. (2013) and Kaaz et al. (2019) have shown that these could significantly change the final mass of the SMS formed via collisions. In this paper, we explore the effect of mass loss due to stellar winds on the final mass of the SMSs produced in nuclear clusters via gas accretion and runaway collisions. We use the same idealised N-body setups as in Das et al. (2020) and include the mass loss due to stellar winds. We adopt the theoretical mass loss recipe given by Vink et al. (2000, 2001). This work is an extension of the model presented in Das et al. (2020).

4.2 Methodology

4.2.1 Initial conditions

To model collisions and accretion in the nuclear clusters consisting of main sequence (MS) stars, we use the Astrophysical MUlti-purpose Software Environment (AMUSE) (Portegies Zwart et al., 2009, 2013; Pelupessy et al., 2013; Portegies Zwart & McMillan, 2018). This is an N-body code with component libraries that can be downloaded for free from `amusecode.org`. In the AMUSE framework different codes, e.g. stellar dynamics, stellar evolution, hydrodynamics and radiative transfer, can be easily coupled. We have modified the code and introduced the mass-radius relation for MS stars, gravitational N-body dynamics, gravitational coupling between the stars and the gas described via an analytic potential, accretion physics, stellar collisions, and mass growth due to accretion and collisions (Das et al., 2020).

The cluster is embedded in a stationary natal gas cloud. Initially both the cluster and gas follow a Plummer density distribution

$$\rho(r) = \frac{3M_{cl}}{4\pi b^3} \left(1 + \frac{r^2}{b^2}\right)^{-\frac{5}{2}} \tag{4.1}$$

(Plummer, 1911), where M_{cl} is the mass of the cluster and b is the Plummer length scale (or Plummer radius) that sets the size of the cluster core. We further assume that both the gas mass (M_{g}) and gas radius (R_{g}) are equal to the mass (M_{cl}) and radius (R_{cl}) of the stellar cluster. We introduce a cut-off radius, which is equal to five times the Plummer radius, after which the density is set to zero so that the cluster remains stable. We consider a Salpeter initial mass function (IMF) (Salpeter, 1955) for the stars:

$$\xi(m)\Delta m = \xi_0 \left(\frac{m}{\mathrm{M}_\odot}\right)^{-\alpha} \left(\frac{\Delta m}{\mathrm{M}_\odot}\right), \tag{4.2}$$

where $\alpha = 2.35$ is the power-law slope of the mass function. We considered a top heavy IMF with mass range $10\,\mathrm{M}_\odot - 100\,\mathrm{M}_\odot$. The main parameters for our simulations are the cluster mass M_{cl}, cluster radius R_{cl}, the gas mass M_{g}, gas radius R_{g}, and the number of stars N.

In principle, pure N-body codes solve Newton's equations of motion with no free physical parameters. However, they have capacities to flag special events e.g. close encounters or binary dynamics. The time-stepping criterion used to integrate the equations of motion is the only adjustable quantity. We used ph4 (e.g. McMillan & Hut, 1996, Sec. 3.2), which is based on a fourth-order Hermite algorithm (Makino & Aarseth, 1992), to model the gravitational interactions between the stars. We modeled the gravitational effect of the gas cloud via an analytical background potential which is coupled to the *N*-body code using the BRIDGE method (Fujii et al., 2007). This allows us to determine the motions of the stars from the total combined potential of the gas and stars.

4.2.2 Stellar properties

Another key ingredient in our simulations is the mass-radius relation of the MS stars as the size of the stars will play an important role in determining the number of collisions via the collisional cross section. The mass-radius ($M_* - R_*$) relation of the stars is given by

$$\frac{R_*}{\mathrm{R}_\odot} = 1.60 \times \left(\frac{M_*}{\mathrm{M}_\odot}\right)^{0.47} \quad \text{for } 10\,\mathrm{M}_\odot \lesssim M_* < 50\,\mathrm{M}_\odot, \tag{4.3}$$

$$\frac{R_*}{\mathrm{R}_\odot} = 0.85 \times \left(\frac{M_*}{\mathrm{M}_\odot}\right)^{0.67} \quad \text{for } 50\,\mathrm{M}_\odot \lesssim M_*, \tag{4.4}$$

where Eq. 4.3 is adopted from Bond et al. (1984) and Eq. 4.4 is adopted from Demircan & Kahraman (1991). However, it is important to note that the mass-radius relation of the SMSs is poorly understood. Moreover, stars produced via collisions could have a larger radii than similar mass stars (e.g. Lombardi et al., 2003). Using smoothed particle hydrodynamics (SPH), Suzuki et al. (2007) have shown that the collision product of massive stars ($\gtrsim 100\,\mathrm{M}_\odot$) could be $10 - 100$ times larger than the equilibrium radius and hence the collision rate could be sufficiently high to have the next collision before the star settles down to the equilibrium radius.

The luminosity of the stars is given by

$$L_* = 1.03 \times M_*^{3.42}\,\mathrm{L}_\odot \quad \text{for } 10\,\mathrm{M}_\odot \lesssim M_* < 120\,\mathrm{M}_\odot, \tag{4.5}$$

$$L_* = f_{\mathrm{Edd}} \times L_{\mathrm{Edd}} \quad \text{for } 120\,\mathrm{M}_\odot \lesssim M_*, \tag{4.6}$$

where

$$L_{\mathrm{Edd}} = 3.2 \times 10^4 \left(\frac{M_*}{\mathrm{M}_\odot}\right)\,\mathrm{L}_\odot. \tag{4.7}$$

Eq. 4.5 is adopted from Demircan & Kahraman (1991). As we are considering stars that are accreting, one might consider that the accretion luminosity

$$L_{\mathrm{acc}} = \frac{GM_*\dot{M}}{R_*} \tag{4.8}$$

also contributes to the total luminosity of the stars. In Fig. 4.1 we have plotted the different luminosity for different accretion scenarios (see below), showing that the accretion luminosity
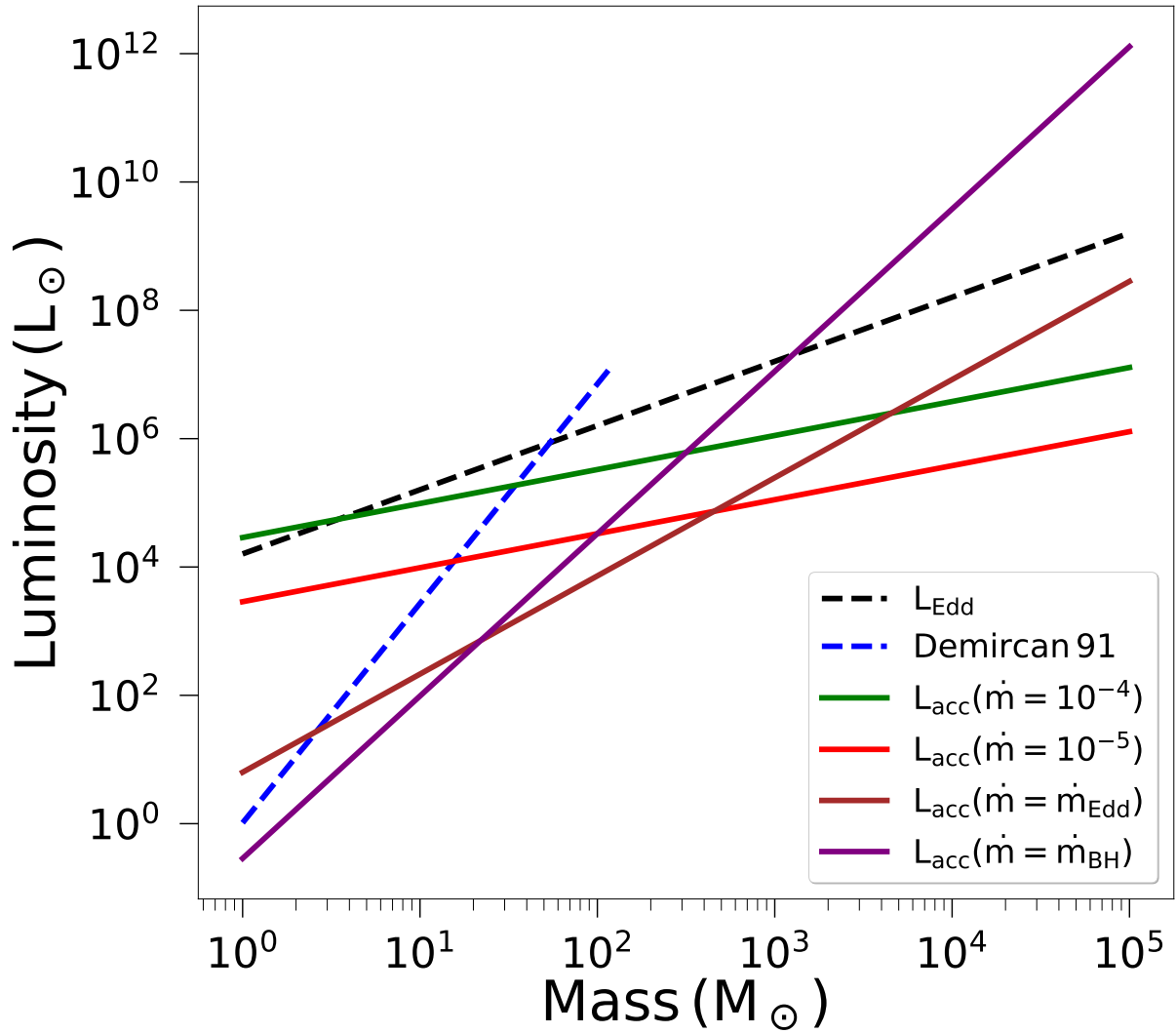
Figure 4.1: Luminosity of stars as a function of mass. The solid lines represent accretion luminosities whereas the dashed lines represent the Eddington luminosity and the luminosity assumed in Demircan & Kahraman (1991), respectively.

is almost always subdominant, except for cases where we are reaching the largest stellar masses. The atmospheric temperature of the star is given from the Stefan-Boltzman equation via

$$T_{\text{eff}}^4 = \frac{L_*}{4\pi R_*^2 \sigma_{\text{SB}}},\tag{4.9}$$

where σ_{SB} is the Stefan-Boltzmann constant.

4.2.3 Gas accretion

The next key ingredient in our simulation is the gas accretion. The protostars formed in the cluster will grow in mass by gas accretion (Bonnell et al., 1998; Krumholz et al., 2009; Hartmann et al., 2016). Das et al. (2020) have found that gas accretion will play a crucial role in determining the number of collisions and hence the final mass of the most massive object (MMO). In our current accretion prescription, the gas is assumed to be initially at rest, and hence due to momentum conservation the stellar velocity decreases as they accrete gas and gain mass, and fall deeper into the potential well of the cluster. We assume that no new stars are formed and hence the gas is fueled into the cluster with 100% accretion efficiency. The efficiency might be reduced due to protostellar outflows (Federrath, 2015; Offner & Chaban, 2017), which are not considered here. At each time step the accreted gas mass is subtracted from the total gas mass, and the density keeps being distributed according to the Plummer profile. Hence, the gas depletion in our simulation is uniform. We consider different accretion scenarios in our work, including constant accretion rates of 10^{-4}, 10^{-5} and $10^{-6}\,\text{M}_\odot\text{yr}^{-1}$, and Eddington accretion given by:

$$\dot{M}_{\text{Edd}} = 2.2 \times 10^{-8} \left(\frac{M_*}{\text{M}_\odot}\right)\ \text{M}_\odot\,\text{yr}^{-1},\tag{4.10}$$

as well as Bondi-Hoyle-Lyttleton (hereafter BHL or Bondi-Hoyle) accretion given by Eq. 2 of Maccarone & Zurek (2012):

$$\dot{M}_{\text{BHL}} = 7 \times 10^{-9} \left(\frac{M_*}{\text{M}_\odot}\right)^2 \left(\frac{n}{10^6\,\text{cm}^{-3}}\right)^2 \left(\frac{\sqrt{c_s^2 + v_\infty^2}}{10^6\,\text{cm s}^{-1}}\right)^{-3}\ \text{M}_\odot\,\text{yr}^{-1}.\tag{4.11}$$

A recent study by Kaaz et al. (2019) has shown that the average BH accretion rate of an individual star is given by

$$\langle\dot{M}_{\text{BHL}}\rangle = \begin{cases} \dot{M}_{\text{BHL}}, & \text{when } R_\perp \gg R_{\text{acc}}, \\ N \times \dot{M}_{\text{BHL}}, & \text{when } R_\perp \leq R_{\text{acc}}, \end{cases}\tag{4.12}$$

where $R_\perp = R_{\text{cl}}N^{-1/3}$ is the mean separation between stars and $R_{\text{acc}} = \frac{2GM_*}{v_\infty^2}$ is the characteristic accretion radius of a star, i.e. the impact parameter in the BHL theory for which gas can be gravitationally-focused and overcome its angular momentum barrier to reach the star. Here, v_∞ is the relative velocity of the star with respect to the gas. Our adopted BHL accretion rate is given by Eq. 4.11. We multiply the BHL rate of a single star by N if $R_\perp \leq R_{\text{acc}}$ according to Eq. 4.12. We compute the density of the gas and hence the $\dot{M}_{\text{BHL}}$ locally.
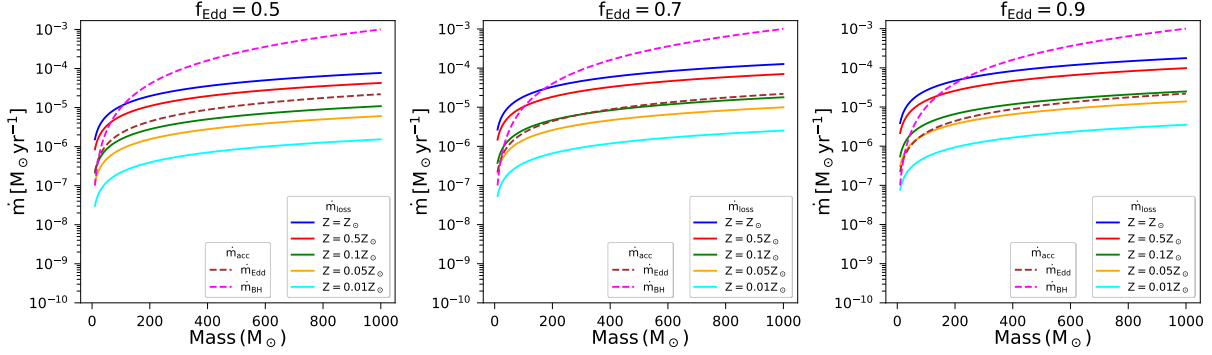
Figure 4.2: Mass loss rate $\dot{m}_{\rm loss}$ as a function of mass for different metallicities (solid lines) and accretion rates (dashed line) as a function of the stellar mass.

4.2.4   Stellar Collisions

We adopt the sticky-sphere approximation to model collisions between the main sequence stars (Leigh & Geller, 2012; Leigh et al., 2017), where the two stars are assumed to merge if the distance between their centres is less than the sum of their radii. The two stars are replaced by a single star whose mass is equal to the sum of the masses of the colliding stars and the radius of the object to be determined by the $(M_* - R_*)$ relation described in Eqs. 4.3 and 4.4. The conservation of linear momentum is implemented during the collision. However, the mass is not necessarily conserved due to the possible ejection of mass (Sills et al., 2002; Dale & Davies, 2006; Trac et al., 2007). The final mass of the colliding objects could change a lot depending on fraction of the mass that is lost during the merger (Alister Seguel et al., 2020; Das et al., 2020). This fraction depends on the type of stars that are colliding (Glebbeek et al., 2013).

4.2.5   Mass loss due to stellar winds

Since the massive stars and the collision products in our simulations become very massive and luminous, mass loss driven by stellar wind plays a key role in their evolution. However, the mass loss of very massive stars is very poorly understood both observationally and theoretically. In this work we adopt the theoretical mass loss recipe given by Vink et al. (2000, 2001). The mass loss rate is a function of the luminosity of the stars L_*, mass of the stars M_*, the Galactic ratio of terminal velocity and escape velocity $v_\infty/v_{\rm esc}$, the effective temperature of the stars $T_{\rm eff}$, and the metallicity of the stars Z_*.

In Fig. 4.2 we have plotted the mass loss rates for different metallicities. We have also plotted the Eddington and Bondi-Hoyle accretion rates to compare with the mass loss rates (the constant accretion rates can be identified without a plotted line). It is interesting to note that for Bondi-Hoyle accretion, the mass loss could be comparable or higher for masses $\lesssim 200\,{\rm M}_\odot$ and metallicities $Z = (0.5 - 1)\,{\rm Z}_\odot$, whereas the Eddington accretion rate is always lower than the mass loss rate in the same metallicity range for any mass. The Eddington accretion rate could be comparable to or higher than the mass loss rate for $Z \lesssim 0.1\,{\rm Z}_\odot$. Another key parameter in the mass loss rate is the Eddington factor $f_{\rm Edd}$, which is given by Eq. 4.7. Nadyozhin & Razinkova (2005) have shown that $0.54 \lesssim f_{\rm Edd} \lesssim 0.94$ for stellar masses in the range $3 \times 10^2\,{\rm M}_\odot \lesssim M_* \lesssim 10^4\,{\rm M}_\odot$. We adopt a typical value of $f_{\rm Edd} = 0.7$ for the rest of our models.

In Fig. 4.2 we show the mass loss rates for different values of f_{Edd}. An important point to note here is that the mass loss recipe in Vink et al. (2001) was computed for $f_{Edd} < 0.5$. Vink et al. (2011) have shown that mass loss rates could be significantly higher for stars close to the Eddington limit. In other words, when extrapolating the results to higher Eddington fractions, it is important to note that we might be underestimating the mass loss that actually occurs.

4.3 Results

The main results of our simulations are presented in this section. We adopted the initial conditions with $N = 5000$, $M_{cl} = M_g = 1.12 \times 10^5 \, M_\odot$, $R_{cl} = R_g = 1$ pc, assuming a Salpeter IMF within a stellar mass interval of $10 - 100 \, M_\odot$. We have assumed three different values of $f_{Edd} = 0.5, 0.7, 0.9$ and for each f_{Edd}, we have studied six different metallicities $Z_* = Z_\odot, 0.5 \, Z_\odot, 0.1 \, Z_\odot, 0.05 \, Z_\odot, 0.01 \, Z_\odot, 0.001 \, Z_\odot$.

The evolution of the cluster is similar to the results in Das et al. (2020). In the initial phase the stars accrete gas and due to momentum conservation the stellar velocity decreases and the stars fall deeper into the potential well of the cluster. During the accretion phase the accretion dominates the mass growth. Once the gas is fully depleted, the stellar collisions take place and drive the mass growth of the SMS. However, some initial collisions might occur which will boost the accretion process, especially for the Eddington and Bondi-Hoyle accretion scenarios. The evolution of the Lagrangian radii will be similar to our previous results in Das et al. (2020). The 10% Lagrange radii will always decrease, eventually leading to a core collapse. The evolution of the 50% and 90% Lagrange radii will be an initial decrease and a later increase after the core collapse. The timing of the transition will depend on the accretion recipe. A similar trend has been seen in previous simulations in the absence of accretion (e.g. Leigh et al., 2014).

The evolution of the mass of the MMO is shown in Fig. 4.3 for constant accretion rates of $10^{-5} \, M_\odot \mathrm{yr}^{-1}$ and $10^{-4} \, M_\odot \mathrm{yr}^{-1}$, as well as for physically-motivated accretion rates of Eddington and Bondi-Hoyle accretion rates. For a constant accretion rate of $10^{-4} \, M_\odot \mathrm{yr}^{-1}$, the growth of the MMO is quite rapid due to mergers of collision products. The mass of the MMO reaches $\sim 10^4 \, M_\odot$ already after 0.8 Myr except for $Z_* = Z_\odot$ for $f_{Edd} = 0.7$ and 0.9. The final mass of the MMO depends on Z_* and f_{Edd}. SMSs of mass $\sim 10^4 \, M_\odot$ are formed for all the cases except for $Z_* = Z_\odot$ for $f_{Edd} = 0.7$ and 0.9 where the final mass of the MMO is $\sim 5 \times 10^3 \, M_\odot$. For the case of a constant accretion rate of $10^{-5} \, M_\odot \mathrm{yr}^{-1}$, the growth of the MMO is more gradual. The MMO reaches a mass of $\sim 10^4 \, M_\odot$ for $Z_* < 0.5 \, Z_\odot$ after ~ 2.5 Myr, and a final mass of $\sim 2 \times 10^4 \, M_\odot$ after 5 Myr. For the case of $Z = 0.5 \, Z_\odot$, the evolution of the MMO depends on the adopted f_{Edd}. For $Z_* = 0.5 \, Z_\odot$, the MMO reaches a mass of $\sim 8 \times 10^3 \, M_\odot, 6 \times 10^3 \, M_\odot$ and $2 \times 10^3 \, M_\odot$, after ~ 2.5 Myr for $f_{Edd} = 0.5, 0.7$ and 0.9, respectively. The final mass after 5 Myr varies between $3 \times 10^3 - 10^4 \, M_\odot$. For the case of $Z = Z_\odot$, no SMS could be formed for $f_{Edd} = 0.9$. However, for $f_{Edd} = 0.5$ and 0.7, a significant growth occurs after 3 Myr, and the MMO reaches a mass of $\sim 5 \times 10^2 \, M_\odot$ and $4 \times 10^3 \, M_\odot$ for $f_{Edd} = 0.7$ and 0.5, respectively, at 5 Myr. The mass loss by winds is stronger for higher metallicity, and so its effect on the final mass of the MMO is more prominent in the case of the lower accretion rate $10^{-5} \, M_\odot \mathrm{yr}^{-1}$ compared to $10^{-4} \, M_\odot \mathrm{yr}^{-1}$.

Next, we explore the Eddington accretion scenario given by Eq. 4.10. For the case of
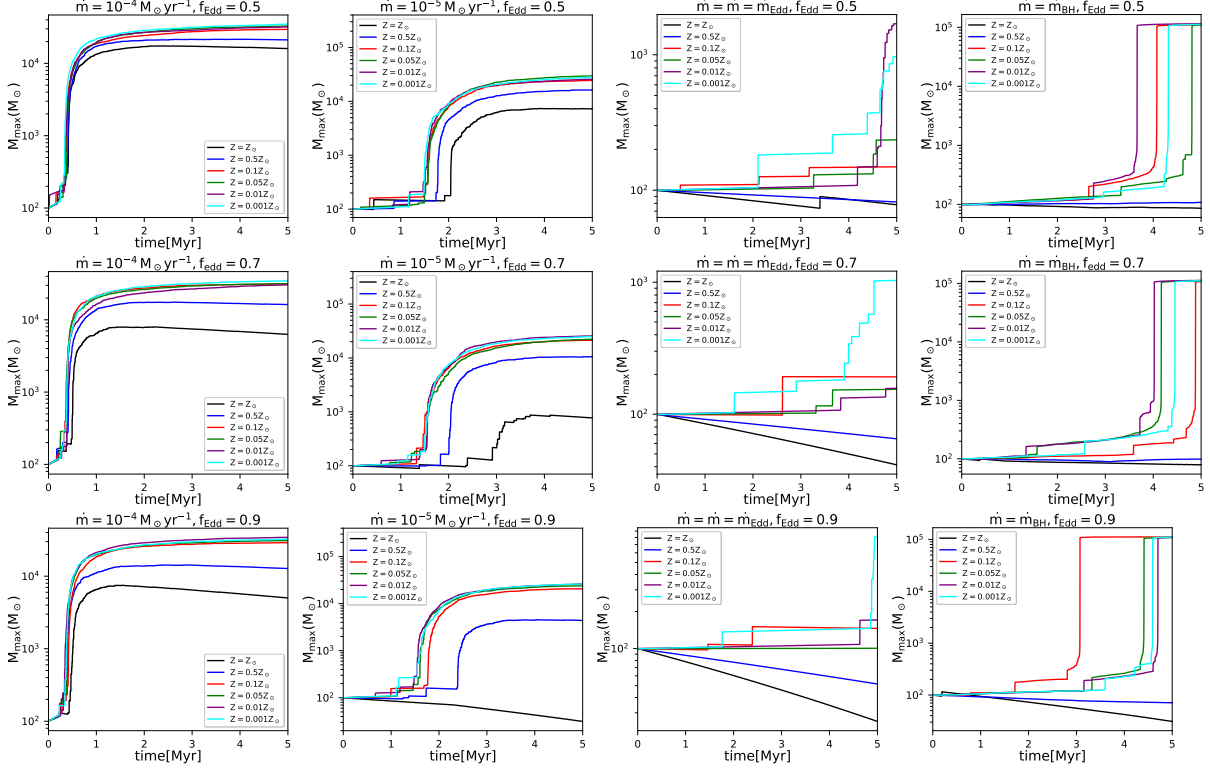
Figure 4.3: Mass evolution of the MMO for different accretion rates and mass loss rates. Different colors represent different values of Z_* as labeled.

Eddington accretion, the growth of the MMO occurs after about 3.5 Myr. However, it is important to note that using this recipe, the MMO does not grow for the cases of $Z_* = Z_\odot$ and $0.5\,Z_\odot$. The final mass of the MMO depends highly on the values of Z_* and f_{Edd}. For $f_{Edd} = 0.5$, an MMO of mass $\sim 10^3\,M_\odot$ is formed for $Z_* \lesssim 0.01\,Z_\odot$. For $f_{Edd} = 0.7$ and 0.9, an MMO of mass $\sim 10^3\,M_\odot$ is formed for $Z_* \lesssim 0.001\,Z_\odot$. Finally, we explore the more extreme case of Bondi-Hoyle accretion given by Eq. 4.11. The growth of the MMO is very slow during the initial period of time (depending on Z_* and f_{Edd}), after which the growth happens in a runaway fashion due to the fact that $\dot{M}_{BH} \propto M_*^2$. The timing of the runaway growth depends on when the first collision happens. Similar to the Eddington accretion scenario, there is no growth of the MMO for the case of $Z = Z_\odot$ and $0.5\,Z_\odot$. The MMO reaches a final mass of $\sim 10^5\,M_\odot$ for $Z_* = 0.1\,Z_\odot$ or lower. The results could also be understood from the comparison of accretion and mass loss rates in Fig. 4.2. For a constant accretion rate of $10^{-4}\,M_\odot\mathrm{yr}^{-1}$, the accretion rate is greater than the mass loss rate for $M_* \lesssim 10^3\,M_\odot$. So the stars have a net gain of mass no matter what metallicity we choose and as a result, they slow down and move towards the core due to momentum conservation. This results in a significant number of collisions and the formation of a SMS in the core. However, for the accretion scenario of $10^{-5}\,M_\odot\mathrm{yr}^{-1}$, Eddington, or Bondi-Hoyle, the accretion rate could be greater or lesser than the mass loss rate depending on the adopted values of Z_* and f_{Edd}.
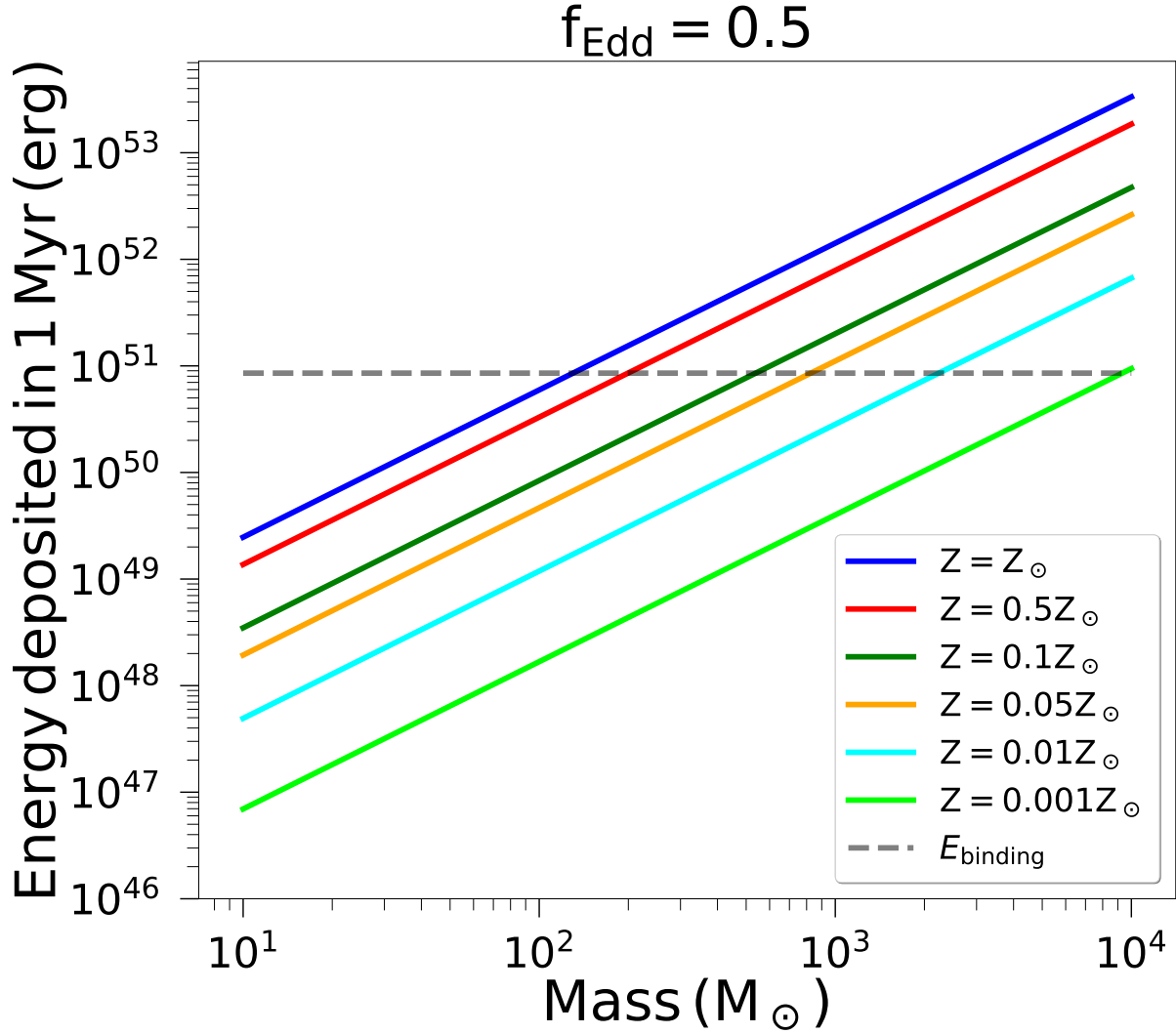
Figure 4.4: Energy deposited by a single star as a function of mass. Different color represents different Z_*. The binding energy of the cluster is shown as the black dashed line for comparison

4.4 Neglected processes

In this paper, we considered the interplay of collisions, physically motivated accretion recipes, and mass loss due to stellar winds. However, there are important processes that were still neglected, and which could have a relevant influence on some of the results.

In the context of stellar winds, we considered only the mass loss, but the winds also deposit kinetic energy into the system. It is therefore important to at least approximately assess its effect. In Fig. 4.4, we show the energy deposited by a single star for different metallicities as a function of mass. The energy deposited by a single star can be calculated as $\dot{E}_{*,\mathrm{kin}} \sim \dot{M}_{\mathrm{loss}} v^2$, where $\dot{M}_{\mathrm{loss}}$ is the mass loss rate of the star (computed for $f_{\mathrm{Edd}} = 0.5$). To estimate the velocity of the winds we calculate the escape velocity from the stellar surface, $v_{\mathrm{esc}} = \sqrt{2GM_*/R_*}$. The wind velocity should correspond to that velocity within a factor of a few (Vink et al., 2000, 2001). We also show the gravitational binding energy of the cluster $E_{\mathrm{bin}} \simeq GM^2/R \sim 9 \times 10^{50}$ erg with

the black dashed line in the same figure for comparison. It is important to note that a single star with mass ~ few times 100 $M_\odot$ will deposit enough energy in 1 Myr to unbind the cluster for metallicities $Z_* \gtrsim 0.5\,M_\odot$. As we go toward lower metallicities, the energy deposition rate is considerably lower. In order to avoid the unbinding of the cluster, one can naively expect the stars to be of lower metallicities. For a constant accretion rate of $10^{-4}\,M_\odot\mathrm{yr}^{-1}$ the SMS is forming within the first 1 Myr, so in principle the deposition of energy by the stellar wind will not prohibit the formation of a SMS. However, for an accretion rate of $10^{-5}\,M_\odot\mathrm{yr}^{-1}$ the SMS is forming at a much later stage, $\gtrsim 2$ Myr. The energy deposited by the wind from the MMO is enough to unbind the cluster within 2 Myr for $Z_* \gtrsim 0.1\,Z_\odot$. For the Eddington accretion scenario, the SMS ~ $10^3\,M_\odot$ is forming at a much later stage ~ $4-5$ Myr for $Z \lesssim 0.01$ Myr for which the binding energy of the cluster is greater than the kinetic energy deposited by the star. So, the deposition of kinetic energy from the star would not be expected to be a problem at least for the run-time of the simulations. For the Bondi-Hoyle scenario, no SMS is forming for $Z_* \gtrsim 0.5\,Z_\odot$, where we expect the unbinding of the cluster to be much faster. For all other cases, the SMS could be formed if kinetic energy feedback was not relevant; however in reality it will unbind the cluster very quickly ($\lesssim 1$ Myr), since for Bondi-Hoyle the mass of the SMS is ~ $10^5\,M_\odot$.

To compute the energy deposited by the whole cluster we can assume a simplified cluster with $N = 5000$ stars with each star of mass $22\,M_\odot$ (which is the average mass of a star in the cluster with the initial conditions we assumed in our simulations). The velocity of the wind can be estimated as for a single star, which yields a characteristic velocity $v \sim 1100$ km/s. The total kinetic energy deposition rate can then be evaluated as $\dot{E}_{\mathrm{kin}} \sim \dot{M}Nv^2 \sim 1.2 \times 10^{53}$ erg Myr^{-1}.

To avoid unbinding the gas within a timescale of 1 Myr, the energy deposition should decrease by at least two orders of magnitude. Equation (21) of Vink et al. (2001) suggests that the mass loss rate scales with the metallicity as $Z^{0.85}$, implying that a decrease of the metallicity by a factor of 225 should bring the energy deposition rate into the regime where the gas no longer becomes unbound. Since this estimate is very approximate, we expect the transition where kinetic energy deposition is no longer relevant to occur somewhere in the range $(10^{-2} - 10^{-3})\,Z_\odot$. For the range in between, gas expulsion due to the winds is expected to limit the potential growth of the central massive object, with this effect becoming weaker at lower metallicities. We also want to note that the gravitational potential energy of the cluster will change with the cluster properties. For a massive cluster or for a compact cluster the binding energy will be higher and hence the formation of the SMS would be more favorable.

On the 5 Myr timescale explored in our simulations, supernova feedback is also expected to become relevant. With the typical energy of 10^{51} erg for a core collapse supernova, it is clear that one such event will expel the gas and terminate the accretion, if it has not stopped already (either due to gas expulsion by stellar winds or as the accretion process may have depleted the gas).

In future work, it will be important to study detailed gas dynamics where the kinetic energy deposition of winds as well as the supernova feedback is taken into account.

4.5   Summary and Discussion

In this work, we explored the effect of mass loss due to stellar winds on the final mass of the SMSs, which could be formed via runaway stellar collisions and gas accretion inside NSCs. We find that a SMS of mass $\gtrsim 10^3 \, M_\odot$ could be formed even in a high metallicity environment for high accretion rates of $10^{-4} \, M_\odot \mathrm{yr}^{-1}$. For an accretion rate of $10^{-5} \, M_\odot \mathrm{yr}^{-1}$, the final mass of the SMS $\sim 10^4 \, M_\odot$ for $Z_* \lesssim 0.5 \, Z_\odot$. Whereas for solar metallicity, no SMS can be formed for $f_{\mathrm{Edd}} = 0.9$ and SMSs of masses $\sim 10^{2-3} \, M_\odot$ can be formed for $f_{\mathrm{Edd}} = 0.7$ and 0.5, respectively. For the case of Eddington accretion it will not be possible to form a SMS in the metallicity regime $\gtrsim 0.1 \, Z_\odot$. Finally, for the Bondi-Hoyle accretion scenario, we find that the formation of a SMS will not be possible in the high metallicity regime of $Z_* \gtrsim 0.5 \, Z_\odot$.

The interaction of the stellar wind and the gas inside the cluster might play an important role in the evolution of the SMS. The winds from the SMSs have high velocities $\sim 10^3$ km s^{-1} (Muijres et al., 2012), which might exceed the escape velocity from the centre of our modelled star cluster. The SMS in the cluster is close to the centre which results in a high collision rate near the centre due to a shorter relaxation time in the core and an increased collisional cross section. If the SMS is displaced by collisions, it rapidly sinks back close to the centre via dynamical friction where it may eventually decouple from the remainder of the cluster. This is also known as the Spitzer instability (Spitzer, 1969). Interestingly, Krause et al. (2016) have found that for a Salpeter type mass function the stellar wind cannot remove the gas inside the cluster. Hence, we do not expect the stellar wind to remove gas from the cluster.

One of the main caveats of this work is the neglect of the kinetic energy deposition through stellar winds, which could contribute significantly to expel the gas. The latter is likely to create a regime where the growth of a massive object is still inhibited, even though the mass loss itself from the winds is no longer significant. Below a critical metallicity in the range $(10^{-2} - 10^{-3}) \, Z_\odot$, this effect is no longer expected to be relevant; however, supernova feedback may lead to the expulsion of the gas. Another relevant caveat is the extrapolation of the mass loss recipe by Vink et al. (2000, 2001) beyond $1000 \, M_\odot$, for which the mass loss is not really well known. Another uncertainty is the mass loss rates for stars close to their Eddington limit. Vink et al. (2011) have shown that the mass-loss rate increases strongly for stars close to the Eddington limit. So we might be underestimating the mass loss rate assuming the Vink et al. (2001) recipe, especially in the high mass regime. We point out that similar to Das et al. (2020), this work contains an idealized simulation setup. In real cosmological systems, the gas dynamics could be different and one needs to solve the hydrodynamics equations. In order to study the gas dynamics in detail, we need to incorporate the full hydrodynamics and hence the cooling, which also depends on the chemistry of the gas. Feedback processes due to the stars would also need to be modeled in more detail. Using cosmological zoom-in simulations, Li et al. (2017) have found that accretion might be regulated by stellar feedback processes. The main goal of this work was to build a simplified model that allows us to study the evolution over a large part of the parameter space for a long timescale of a few Myr. For future work, it will be important to explore more realistic accretion scenarios and their interaction with the mass loss process, as well as mass loss in the range of high stellar masses.

Acknowledgements

Data availability

The data underlying this article will be shared on reasonable request to the corresponding author.

Bibliography

Agarwal B., Khochfar S., Johnson J. L., Neistein E., Dalla Vecchia C., Livio M., 2012, MNRAS, 425, 2854

Agarwal B., Cullen F., Khochfar S., Ceverino D., Klessen R. S., 2019, MNRAS, 488, 3268

Alexander T., Bar-Or B., 2017, Nature Astronomy, 1, 0147

Alexander T., Natarajan P., 2014, Science, 345, 1330

Alister Seguel P. J., Schleicher D. R. G., Boekholt T. C. N., Fellhauer M., Klessen R. S., 2020, MNRAS, 493, 2352

Amaro-Seoane P., Freitag M., 2006, ApJ, 653, L53

Amaro-Seoane P., Gair J. R., Freitag M., Miller M. C., Mandel I., Cutler C. J., Babak S., 2007, Classical and Quantum Gravity, 24, R113

Arca Sedda M., Mastrobuono-Battisti A., 2019, arXiv e-prints, p. arXiv:1906.05864

Askar A., Davies M. B., Church R. P., 2020, arXiv e-prints, p. arXiv:2006.04922

Aykutalp A., Wise J. H., Spaans M., Meijerink R., 2014, ApJ, 797, 139

Bañados E., et al., 2018, Nature, 553, 473

Barkana R., Loeb A., 2001, Phys. Rep., 349, 125

Basu S., Das A., 2019, ApJ, 879, L3

Becerra F., Greif T. H., Springel V., Hernquist L. E., 2015, MNRAS, 446, 2380

Becerra F., Marinacci F., Bromm V., Hernquist L. E., 2018, MNRAS, 480, 5029

Begelman M. C., Volonteri M., 2017, MNRAS, 464, 1102

Begelman M. C., Volonteri M., Rees M. J., 2006, MNRAS, 370, 289

Bender R., et al., 2005a, ApJ, 631, 280

Bender R., et al., 2005b, ApJ, 631, 280

Boekholt T. C. N., Schleicher D. R. G., Fellhauer M., Klessen R. S., Reinoso B., Stutz A. M., Haemmerlé L., 2018, MNRAS, 476, 366

Böker T., Laine S., van der Marel R. P., Sarzi M., Rix H.-W., Ho L. C., Shields J. C., 2002, AJ, 123, 1389

Bond J. R., Arnett W. D., Carr B. J., 1984, ApJ, 280, 825

Bonnell I. A., Bate M. R., Zinnecker H., 1998, MNRAS, 298, 93

Bromm V., Loeb A., 2003, ApJ, 596, 34

Carollo C. M., Stiavelli M., de Zeeuw P. T., Mack J., 1997, AJ, 114, 2366

Chon S., Omukai K., 2020, MNRAS, 494, 2851

Chon S., Hosokawa T., Yoshida N., 2018, MNRAS, 475, 4104

Corbett Moran C., Grudić M. Y., Hopkins P. F., 2018, arXiv e-prints, p. arXiv:1803.06430

Dale J. E., Davies M. B., 2006, MNRAS, 366, 1424

Das A., Schleicher D. R. G., Leigh N. W. C., Boekholt T. C. N., 2020, arXiv e-prints, p. arXiv:2012.01456

Davies M. B., Miller M. C., Bellovary J. M., 2011, ApJ, 740, L42

Davies M. B., Askar A., Church R. P., 2019, Proceedings of the International Astronomical Union, 14, 80–83

Dayal P., Rossi E. M., Shiralilou B., Piana O., Choudhury T. R., Volonteri M., 2019, MNRAS, 486, 2336

Demircan O., Kahraman G., 1991, Ap&SS, 181, 313

Devecchi B., Volonteri M., 2009, ApJ, 694, 302

Devecchi B., Volonteri M., Colpi M., Haardt F., 2010, MNRAS, 409, 1057

Devecchi B., Volonteri M., Rossi E. M., Colpi M., Portegies Zwart S., 2012, MNRAS, 421, 1465

Dijkstra M., Ferrara A., Mesinger A., 2014, MNRAS, 442, 2036

Dopcke G., Glover S. C. O., Clark P. C., Klessen R. S., 2011, ApJ, 729, L3

Ebisuzaki T., et al., 2001, ApJ, 562, L19

Fan X., et al., 2001, AJ, 122, 2833

Federrath C., 2015, MNRAS, 450, 4035

Ferrara A., Salvadori S., Yue B., Schleicher D., 2014, MNRAS, 443, 2410

Ferrarese L., et al., 2006, ApJ, 644, L21

Freitag M., 2008, in Beuther H., Linz H., Henning T., eds, Astronomical Society of the Pacific Conference Series Vol. 387, Massive Star Formation: Observations Confront Theory. p. 247 (arXiv:0711.4057)

Freitag M., Guerkan M. A., Rasio F. A., 2007, in St.-Louis N., Moffat A. F. J., eds, Astronomical Society of the Pacific Conference Series Vol. 367, Massive Stars in Interactive Binaries. p. 707 (arXiv:astro-ph/0410327)

Fujii M., Iwasawa M., Funato Y., Makino J., 2007, PASJ, 59, 1095

Georgiev I. Y., Böker T., Leigh N., Lützgendorf N., Neumayer N., 2016, MNRAS, 457, 2122

Gieles M., Charbonnel C., 2019, Proceedings of the International Astronomical Union, 14, 297–301

Glebbeek E., Gaburov E., de Mink S. E., Pols O. R., Portegies Zwart S. F., 2009, A&A, 497, 255

Glebbeek E., Gaburov E., Portegies Zwart S., Pols O. R., 2013, MNRAS, 434, 3497

Graham A. W., Spitler L. R., 2009, MNRAS, 397, 2148

Gürkan M. A., Fregeau J. M., Rasio F. A., 2006, ApJ, 640, L39

Haemmerlé L., Woods T. E., Klessen R. S., Heger A., Whalen D. J., 2018, MNRAS, 474, 2757

Haiman Z., 2004, ApJ, 613, 36

Haiman Z., Loeb A., 2001, ApJ, 552, 459

Hartmann L., Herczeg G., Calvet N., 2016, ARA&A, 54, 135

Hirano S., Hosokawa T., Yoshida N., Kuiper R., 2017, Science, 357, 1375

Hosokawa T., Omukai K., Yorke H. W., 2012, ApJ, 756, 93

Hosokawa T., Yorke H. W., Inayoshi K., Omukai K., Yoshida N., 2013, ApJ, 778, 178

Inayoshi K., Haiman Z., 2014, MNRAS, 445, 1549

Inayoshi K., Visbal E., Kashiyama K., 2015, MNRAS, 453, 1692

Inayoshi K., Ostriker J. P., Haiman Z., Kuiper R., 2018, MNRAS, 476, 1412

Inayoshi K., Visbal E., Haiman Z., 2019, arXiv e-prints, p. arXiv:1911.05791

Kaaz N., Antoni A., Ramirez-Ruiz E., 2019, ApJ, 876, 142

Katz H., Sijacki D., Haehnelt M. G., 2015, MNRAS, 451, 2352

Kim S. S., Figer D. F., Morris M., 2004, ApJ, 607, L123

King A. R., Pringle J. E., 2006, MNRAS, 373, L90

King A. R., Pringle J. E., Hofmann J. A., 2008, MNRAS, 385, 1621

Kormendy J., Ho L. C., 2013, ARA&A, 51, 511

Krause M. G. H., Charbonnel C., Bastian N., Diehl R., 2016, A&A, 587, A53

Krumholz M. R., Klein R. I., McKee C. F., Offner S. S. R., Cunningham A. J., 2009, Science, 323, 754

Latif M., Schleicher D., 2019, Formation of the First Black Holes, doi:10.1142/10652.

Latif M. A., Schleicher D. R. G., Schmidt W., Niemeyer J., 2013, MNRAS, 433, 1607

Latif M. A., Bovino S., Grassi T., Schleicher D. R. G., Spaans M., 2015, MNRAS, 446, 3163

Latif M. A., Omukai K., Habouzit M., Schleicher D. R. G., Volonteri M., 2016, ApJ, 823, 40

Latif M. A., Khochfar S., Whalen D., 2020, ApJ, 892, L4

Leigh N., Geller A. M., 2012, MNRAS, 425, 2369

Leigh N., Böker T., Knigge C., 2012, MNRAS, 424, 2130

Leigh N. W. C., Mastrobuono-Battisti A., Perets H. B., Böker T., 2014, MNRAS, 441, 919

Leigh N. W. C., Georgiev I. Y., Böker T., Knigge C., den Brok M., 2015, MNRAS, 451, 859

Leigh N. W. C., Geller A. M., Shara M. M., Garland J., Clees-Baron H., Ahmed A., 2017, MNRAS, 471, 1830

Li H., Gnedin O. Y., Gnedin N. Y., Meng X., Semenov V. A., Kravtsov A. V., 2017, ApJ, 834, 69

Lombardi J. C., Thrall A. P., Deneva J. S., Fleming S. W., Grabowski P. E., 2003, MNRAS, 345, 762

Lupi A., Colpi M., Devecchi B., Galanti G., Volonteri M., 2014, MNRAS, 442, 3616

Maccarone T. J., Zurek D. R., 2012, MNRAS, 423, 2

Madau P., Haardt F., Dotti M., 2014, ApJ, 784, L38

Makino J., Aarseth S. J., 1992, PASJ, 44, 141

Mastrobuono-Battisti A., Perets H. B., Loeb A., 2014, ApJ, 796, 40

Matsuoka Y., et al., 2018, PASJ, 70, S35

Matsuoka Y., et al., 2019, ApJ, 883, 183

Mayer L., Fiacconi D., Bonoli S., Quinn T., Roškar R., Shen S., Wadsley J., 2015, ApJ, 810, 51

McMillan S. L. W., Hut P., 1996, ApJ, 467, 348

Milosavljević M., Couch S. M., Bromm V., 2009, ApJ, 696, L146

Moeckel N., Clarke C. J., 2011, MNRAS, 410, 2799

Mortlock D. J., et al., 2011, Nature, 474, 616

Muijres L. E., Vink J. S., de Koter A., Müller P. E., Langer N., 2012, A&A, 537, A37

Nadyozhin D. K., Razinkova T. L., 2005, Astronomy Letters, 31, 695

Natarajan P., 2021, MNRAS, 501, 1413

Nguyen D. D., et al., 2019, ApJ, 872, 104

Offner S. S. R., Chaban J., 2017, ApJ, 847, 104

Oh S. P., Haiman Z., 2002, ApJ, 569, 558

Omukai K., 2001, ApJ, 546, 635

Omukai K., Schneider R., Haiman Z., 2008, ApJ, 686, 801

Pacucci F., Loeb A., 2020, ApJ, 895, 95

Pacucci F., Volonteri M., Ferrara A., 2015, MNRAS, 452, 1922

Pacucci F., Natarajan P., Volonteri M., Cappelluti N., Urry C. M., 2017, ApJ, 850, L42

Pelupessy F. I., van Elteren A., de Vries N., McMillan S. L. W., Drost N., Portegies Zwart S. F., 2013, A&A, 557, A84

Piana O., Dayal P., Volonteri M., Choudhury T. R., 2021, MNRAS, 500, 2146

Plummer H. C., 1911, MNRAS, 71, 460

Portegies Zwart S. F., McMillan S. L. W., 2002, ApJ, 576, 899

Portegies Zwart S., McMillan S., 2018, Astrophysical Recipes; The art of AMUSE, doi:10.1088/978-0-7503-1320-9.

Portegies Zwart S. F., Baumgardt H., Hut P., Makino J., McMillan S. L. W., 2004, Nature, 428, 724

Portegies Zwart S. F., Baumgardt H., McMillan S. L. W., Makino J., Hut P., Ebisuzaki T., 2006, ApJ, 641, 319

Portegies Zwart S., et al., 2009, New Astron., 14, 369

Portegies Zwart S., McMillan S. L. W., van Elteren E., Pelupessy I., de Vries N., 2013, Computer Physics Communications, 184, 456

Rasskazov A., Fragione G., Kocsis B., 2020, ApJ, 899, 149

Regan J. A., Downes T. P., 2018, MNRAS, 478, 5037

Regan J. A., Johansson P. H., Wise J. H., 2014, ApJ, 795, 137

Regan J. A., Visbal E., Wise J. H., Haiman Z., Johansson P. H., Bryan G. L., 2017, Nature Astronomy, 1, 0075

Regan J. A., Downes T. P., Volonteri M., Beckmann R., Lupi A., Trebitsch M., Dubois Y., 2019, MNRAS, 486, 3892

Regan J. A., Haiman Z., Wise J. H., O'Shea B. W., Norman M. L., 2020a, The Open Journal of Astrophysics, 3, E9

Regan J. A., Wise J. H., O'Shea B. W., Norman M. L., 2020b, MNRAS, 492, 3021

Reinoso B., Schleicher D. R. G., Fellhauer M., Klessen R. S., Boekholt T. C. N., 2018, A&A, 614, A14

Rizzuto F. P., et al., 2021, MNRAS, 501, 5257

Rossa J., van der Marel R. P., Böker T., Gerssen J., Ho L. C., Rix H.-W., Shields J. C., Walcher C.-J., 2006, AJ, 132, 1074

Sakurai Y., Vorobyov E. I., Hosokawa T., Yoshida N., Omukai K., Yorke H. W., 2016, MNRAS, 459, 1137

Sakurai Y., Yoshida N., Fujii M. S., Hirano S., 2017, MNRAS, 472, 1677

Salpeter E. E., 1955, ApJ, 121, 161

Schleicher D. R. G., Palla F., Ferrara A., Galli D., Latif M., 2013, A&A, 558, A59

Schleicher D. R. G., et al., 2019, Boletin de la Asociacion Argentina de Astronomia La Plata Argentina, 61, 234

Schödel R., Feldmeier A., Neumayer N., Meyer L., Yelda S., 2014, Classical and Quantum Gravity, 31, 244007

Scott N., Graham A. W., 2013, ApJ, 763, 76

Seth A., Agüeros M., Lee D., Basu-Zych A., 2008, ApJ, 678, 116

Seth A. C., Neumayer N., Böker T., 2020, in Bragaglia A., Davies M., Sills A., Vesperini E., eds, IAU Symposium Vol. 351, IAU Symposium. pp 13–18 (arXiv:1908.00022), doi:10.1017/S1743921319007117

Shang C., Bryan G. L., Haiman Z., 2010, MNRAS, 402, 1249

Shen Y., et al., 2019, ApJ, 873, 35

Shlosman I., Choi J.-H., Begelman M. C., Nagamine K., 2016, MNRAS, 456, 500

Sills A., Adams T., Davies M. B., Bate M. R., 2002, MNRAS, 332, 49

Smith A., Bromm V., 2019, Contemporary Physics, 60, 111

Spitzer Lyman J., 1969, ApJ, 158, L139

Stone N. C., Küpper A. H. W., Ostriker J. P., 2017, MNRAS, 467, 4180

Sugimura K., Omukai K., Inoue A. K., 2014, MNRAS, 445, 544

Sugimura K., Hosokawa T., Yajima H., Inayoshi K., Omukai K., 2018, MNRAS, 478, 3961

Suzuki T. K., Nakasato N., Baumgardt H., Ibukiyama A., Makino J., Ebisuzaki T., 2007, ApJ, 668, 435

Takeo E., Inayoshi K., Mineshige S., 2020, arXiv e-prints, p. arXiv:2002.07187

Tamfal T., Capelo P. R., Kazantzidis S., Mayer L., Potter D., Stadel J., Widrow L. M., 2018, ApJ, 864, L19

Toyouchi D., Hosokawa T., Sugimura K., Nakatani R., Kuiper R., 2019, MNRAS, 483, 2031

Trac H., Sills A., Pen U.-L., 2007, MNRAS, 377, 997

Umeda H., Hosokawa T., Omukai K., Yoshida N., 2016, ApJ, 830, L34

Vergara M. Z. C., Schleicher D. R. G., Boekholt T. C. N., Reinoso B., Fellhauer M., Klessen R. S., Leigh N. W. C., 2021, arXiv e-prints, p. arXiv:2104.01451

Vink J. S., de Koter A., Lamers H. J. G. L. M., 2000, A&A, 362, 295

Vink J. S., de Koter A., Lamers H. J. G. L. M., 2001, A&A, 369, 574

Vink J. S., Muijres L. E., Anthonisse B., de Koter A., Gräfener G., Langer N., 2011, A&A, 531, A132

Visbal E., Haiman Z., Bryan G. L., 2014, MNRAS, 445, 1056

Volonteri M., 2012, Science, 337, 544

Volonteri M., Rees M. J., 2005, ApJ, 633, 624

Volonteri M., Silk J., Dubus G., 2015, ApJ, 804, 148

Vorobyov E. I., Basu S., 2015, ApJ, 805, 115

Vorobyov E. I., DeSouza A. L., Basu S., 2013, ApJ, 768, 131

Wang R., et al., 2019, ApJ, 887, 40

Willott C. J., et al., 2010, AJ, 139, 906

Wirth H., Bekki K., 2020, MNRAS, 496, 921

Wise J. H., Regan J. A., O'Shea B. W., Norman M. L., Downes T. P., Xu H., 2019, Nature, 566, 85

Wolcott-Green J., Haiman Z., Bryan G. L., 2017, MNRAS, 469, 3329

Woods T. E., Heger A., Whalen D. J., Haemmerlé L., Klessen R. S., 2017, ApJ, 842, L6

Woods T. E., et al., 2019, Publ. Astron. Soc. Australia, 36, e027

Wu X.-B., et al., 2015, Nature, 518, 512

Chapter 5

Summary

In this Thesis, we have studied the formation and growth history of supermassive black holes (SMBH) in the early universe. Many models have been proposed to describe the formation of SMBHs in early universe. In chapter 2, we have studied the direct collapsed black holes (DCBH) model whereas in chapter 3 and chapter 4 we have studied the formation of supermassive black hole seeds via gas accretion and collisions in a nuclear star cluster. Some of the important results from the different chapters are summarized below.

Chapter 2

- The quasar luminosity function (QLF) can be fitted with a tapered power law rather than a double power law which has been commonly used in the literature

- The break point of the power law identifies the end of the era of DCBH creation

- The observed QLF can be fitted with a power-law index $\alpha = 0.5$ and the break-point related parameter $\beta = 8.4$. These are consistent with a period of rapid mass growth of DCBH with super-Eddington factor $\chi = 2.8$, for a time period $T = 150$ Myr during which the growth rate of the number density n_{DCBH} was $\lambda = 28.0\,\mathrm{Gyr}^{-1}$

Chapter 3

- SMS of masses $\sim 10^{3-5}\,\mathrm{M}_{\odot}$ can be formed for accretion rates of $10^{-6} - 10^{-4}\,\mathrm{M}_{\odot}\,\mathrm{yr}^{-1}$. These SMSs can directly collapse into seed black holes with similar mass, they can grow into the billion solar-mass black holes observed at $z \gtrsim 6$. Eddington accretion produces a central massive object of a few times $10^3\,\mathrm{M}_{\odot}$ in our reference scenario, while Bondi accretion robustly produces final masses $\sim 10^5\,\mathrm{M}_{\odot}$

- When evaluating the timescale to have collisions between any two objects within the cluster, the collision timescale can become comparable to or shorter than accretion timescale. We therefore expect collisions to play an important relevant role for the growth of the most massive object

- For constant accretion rates, the results were insensitive to the choice of IMF, while in the case of Eddington accretion, a larger upper-mass limit favours larger final masses. In the case of Bondi accretion, the time of occurrence of the first collision is more important than an initially larger mass

- For constant accretion rates, a more compact cluster significantly favors the formation of a supermassive star. A very similar dependence is found for Eddington accretion. Even SMSs of masses $10^4\,M_\odot$ can be formed for Eddington accretion rate if the cluster is compact with radius $\sim 0.3\,\mathrm{pc}$ or smaller. For the Bondi case, the final mass is independent of the size of the cluster

- A fixed mass loss of 3% or 5% during collisions has a more pronounced effect and can change the final mass by around an order of magnitude, as the mass loss may then become comparable to the mass gained via the collisions. It will thus be important to understand the expected mass loss from stellar models

Chapter 4

- The mass loss rate will depend both on Z_* and $f_{\mathrm{Edd}} = L_*/L_{\mathrm{Edd}}$. SMSs of masses $\gtrsim 10^3\,M_\odot$ could be formed even in a high metallicity environment for high accretion rates of $10^{-4}\,M_\odot\mathrm{yr}^{-1}$. For an accretion rate of $10^{-5}\,M_\odot\mathrm{yr}^{-1}$, the final mass of the SMS $\sim 10^4\,M_\odot$ for $Z_* \lesssim 0.5\,Z_\odot$. Whereas for solar metallicity, no SMS can be formed for $f_{\mathrm{Edd}} = 0.9$ and SMSs of masses $\sim 10^{2-3}\,M_\odot$ can be formed for $f_{\mathrm{Edd}} = 0.7$ and 0.5. For the case of Eddington accretion it will not be possible to form a SMS in the metallicity regime $\gtrsim 0.1\,Z_\odot$. Finally, for the Bondi-Hoyle accretion scenario, we find that the formation of a SMS will not be possible in the high metallicity regime of $Z_* \gtrsim 0.5\,Z_\odot$

We have explored two different mechanisms of SMBH formation. Whether the SMBHs are formed via the DCBH mechanism or via collisions and accretion in a stellar cluster or by any other proposed mechanism will be verified by future observations. Our results show how the observed quasar luminosity function can be fitted with a tapered power law and that the parameters which define the power law can capture the formation and growth history of these SMBHs. Future observations will help us to put better constraints on these parameters and reveal the cosmic history of SMBH formation. Detection of large numbers of high redshift quasars will lead to a better determination of the quasar luminosity function and its evolution with redshift.

We have also shown that a Nuclear Star Cluster can be a potential birthplace for the SMBH seeds. The high density of stars in the NSCs result in stellar collisions. Gas accretion by the stars can enhance the number of collisions, which lead to the formation of a supermassive star that can collapse into a similar mass black hole. Many current observations already found SMBHs inside the NSCs in the local universe. However, whether these SMBHs are actually formed inside the NSCs via collisions and accretion will be confirmed by future observations of the high redshift universe.

The upcoming James Webb Space Telescope (JWST, set to launch in 2021) with it's impressive angular resolution and a light-collecting area much larger than the Hubble Space Telescope (HST), will be able to observe the universe to farther distances than ever before. It is expected that JWST will be able to detect massive objects $\sim 10^{5-6}\,\mathrm{M}_\odot$ at $z \sim 10$ (about 480 Myr after the Big Bang), which will open a window to the dawn of high redshift SMBHs. This will undoubtedly lead to more robust luminosity function determinations and a better account of the formation and growth history of SMBHs.

Arpan Das

Research Interests	*Supermassive Black Holes - First Stars - Reionization - 21cm Cosmology - Modelling Technique and data analysis - Data Science - Machine Learning - Aritifical Intelligence*

EDUCATION

University of Western Ontario, Canada
PhD in Astronomy   2017-2021

Thesis: Formation of Supermassive Black Holes in the Early Universe

Scuola Normale Superiore, Pisa, Italy
Thesis: 21-cm cosmology in the early universe

Department of Physics and Astrophysics, University of Delhi, Delhi, India
M.Sc in Physics (Specialization: Astrophysics),   2011-2013

Thesis: Re-ionization History of the Universe, its possible sources and its cosmological consequences

University of Calcutta, Kolkata, India
B.Sc in Physics,   2008-2011

Publications

1) Formation of supermassive black hole seeds in nuclear star clusters via gas accretion and runaway collisions, The Monthly Notices of the Royal Astronomical Society,   2021
https://doi.org/10.1093/mnras/stab402

2) Effect of mass loss due to stellar wind in the final mass of the supermassive black hole seed in Nuclear Star Cluster, Monthly Notices of Royal Astronomical Society (Submitted),   2021

3) The Mass Function of Supermassive Black Holes in the Direct-collapse Scenario, The Astrophysical Journal Letter,   2019
https://doi.org/10.3847/2041-8213/ab2646

4) High Mass X-ray Binaries and the Cosmic 21-cm Signal: Impact of Host Galaxy Absorption, Monthly Notices of the Royal Astronomical Society,   2017
https://doi.org/10.1093/mnras/stx943

Experience

Doctoral Research, University of Western Ontario, Canada

- Build an analytical model to describe the mass distribution of supermassive black holes in the early universe
- Won two prestigious scholarships to build a collaboration between Canada and Chile and study the formation of Black Holes in Early Universe using numerical simulations
- Developed an N-body code in Python which can simulate a stellar cluster
- Modified the code to run in GPU and improved the performance of the code using a single Nvidia GPU
- Modified the code further to run it in the GPU cluster of Compute Canada
- Developed analysis pipeline of the huge dataset using Python
- Developed a code to visualize the huge dataset using Python

- Modified the code to include complicated physics e.g. the mass loss due to stellar winds
- Published 2 papers and submitted 1 more in peer reviewed journals e.g. Astrophysical Journal and Monthly Notices of Royal Astronomical Society
- Teaching assistant for the course Computer Simulations in Physics to teach Python and GitHub to undergraduate students and several other Astronomy related courses
- Helped undergraduate students in numerical projects using Python

Junior Research Fellow, Scuola Normale Superiore di Pisa, Italy

- Worked for the European Research Council funded project An Illumination of the Dark Ages (AIDA) to investigates the birth of the very first stars and galaxies in our Universe
- Helped to modify the semi-numerical code 21cmFast using C++ which is able to produce 3D cosmological realizations of many physical fields in the early Universe
- eveloped a pipeline in Python which could read the big data output from the simulation and produce the relevant results
- Estimated parameters using Bayesian estimation
- Developed a radiative transfer code for early galaxies using Python
- Helped to develop a ray transfer code for early galaxies using C++
- Helped to develop a Monte Carlo Markov Chain sampler of 21CMFAST which directly forward models the 3D cosmic 21-cm signal in a fully Bayesian framework
- Published the research work in Monthly Notice of Royal Astronomical Society which has been cited 38 times till now

Computer and Software Skills

- **Programming Languages-** Python (6 years, expert), R (1 year), C++(3 years, skilled), Fortran(1 year)
- **Tools and Libraries** Astropy, numpy, scipy, matplotlib, scikit-learn, Matplotlib, Statmodels, Pandas, Theano, Tensorflow, Seaborn, HDF5, Docker, MySQL, Pytorch, PySpark, Keras
- **Data Analysis** Regression, Clustering, SVM, Time Series Analysis, Image Analysis, Spectral Analysis, Neural Networks (basics)
- **Statistics** Frequentist methods, Multivariate Analysis, Bayesian Inference, Hypothesis Testing, MCMC.
- **Astrophysical Simulations and Codes-** AMUSE, MUSIC, CAMB, CosmoMC, CLASS, 21cmFast, Xspec, Chianti
- **Productive Softwares-**LaTex, Microsoft Office, Powerpoint, Excel
- **Operating Systems-** Mac OSX, Linux, Windows
- **Other Softwares-** Photoshop, Adobe Premiere Pro

Awards & Scholarships

- *Science International Engagement Fund Award*, Canada, 2020
- *Mitacs Globalink Research Award*, Canada, 2019
- *European Research Council scholarship*, Italy, 2014
- *Award for excellent performance during the first year of M.Sc Study*, University of Delhi, India, 2011

Workshops, Conferences and Internships

- *Colloquium Talk*, IUCAA Centre for Astronomy Research and Development, University of Delhi,   2020

- *Colloquium Talk*, Departamento De Astronoma, Universidad De Concepcion,   2020

- *Conference Speaker and Poster*, **First Stars VI**, Departamento De Astronoma, Universidad De Concepcion,   2020

- *Visiting Research Student*, Harvard-Smithsonian Center for Astrophysics, University of Harvard,   2019

- *Introduction to R and Intermediate R workshop*,University of Western Ontario,   2019

- *Public talk at Cronyn Observatory*, University of Western Ontario,   2019

- *Cosmological Signals from Cosmic Dawn to the Present, 2018 Aspen Winter Conference on Astrophysics*
  Conference talk,High Mass X-ray Binaries and the Cosmic 21-cm Signal: Impact of Host Galaxy Absorption   2018

- *Invited talk,Studying High Mass X-ray Binraies with cosmological 21-cm signal*, Department of Physics and Astrophysics, University of Delhi,India   2016

- *Light from the Cosmic Dark Ages DAVID VIII International Workshop, Scuola Normale Superiore di Pisa, Italy*
  Conference talk, X-ray heating of the intergalactic medium and the cosmological 21-cm signal   2015

- *Advanced Workshop on Cosmological Structures from Reionization to Galaxies: combining efforts from analytical and numerical methods*
  International Centre for Theoretical Physics, Trieste, Italy   2015

- *First ICTP advanced School on Cosmology*
  International Centre for Theoretical Physics, Trieste, Italy   2015

- *Summer School on Cosmology*
  International Centre for Theoretical Physics, Trieste, Italy   2014

- *Workshop on Cosmology from Baryons at High redshift*
  International Centre for Theoretical Physics, Trieste, Italy   2014

- *IUCAA Sponsored Workshop on Cosmology, Present Observational Constraints on Cosmological Parameters*
  IUCAA resource centre, University of Delhi, India   2013

- *Summer research student, Cosmological Redshift and Wolf effect*
  Indian Statistical Institute, Kolkata   2012